2012

Computational fluid dynamic modeling of fluidized bed polymerization reactors

Ram Ganesh Rokkam
Iowa State University

Computational fluid dynamic modeling of fluidized-bed polymerization reactors

by

Ram Ganesh Rokkam

A dissertation submitted to the graduate faculty

in partial fulfillment of the requirements for the degree of

DOCTOR OF PHILOSOPHY

Major: Chemical Engineering

Program of Study Committee:

Rodney O. Fox, Major Professor

James C. Hill

Dennis R. Vigil

Zhi J. Wang

S. Subramaniam

Iowa State University

Ames, Iowa

2012

TABLE OF CONTENTS

LIST OF TABLES

LIST OF FIGURES

ACKNOWLEDGEMENT

I would like to take this opportunity to express my thanks to those who helped with my PhD thesis research. First anf foremost, I would thank my major professor Dr. Fox for his guidance and support throughout the project. His discussions and comments were helpful in analyzing, conducting and improving my research. I would also like to thank my program of study committee members: Dr. Subramaniam, Dr. Wang, Dr. Vigil and Dr. Hill for their contributions. Special thanks to Dr. Passalacqua for answering my countless number of questions and help on using MFIX and OpenFOAM. I acknowledge Dr. Muhle's help on Univation Technologies project. His insightful comments and suggestions on the annual reports and journal publications helped in exploring different aspects of research. A warm thanks to all my colleagues at Fox group: Sean, Maulik, Jason, Janine, Yanxiang, Qingluan, Wei. Also, I would like to thank Dr. Mehrani and Andrew from University of Ottawa, Canada for the many discussions on electrostatics and experimental data in laboratory scale fluidized-bed. I would like to thank my friends (Siva, Prasad, Prem, Vichu, Shibi, Sriram, Rakesh, Sambit, Siva Kin, ...) in Ames for all their help and memorable experiences. I am deeply indebted to my close friends (Hari, Ravi, RamaKrishna, Lakshmi Tata, GowriSankar, Thirumalesha, Bhoom) who motivated, supported and guided me at various stages of my life.

Finally, I would like to thank my wonderful family. I thank my father Ramachandra Rao for instilling the importance of hard work and higher education. I am grateful to my loving mother Lakshmi for her patience and encouragement. I am thankful to my sister Sri and brother Hari for their love, support and motivation. I gratefully acknowledge the financial support from Univation Technologies LLC (Baytown, TX) and US DOE NETL (FWP to Ames Laboratory, Ames, IA) for the projects done during my PhD.

.

ABSTRACT

Polyethylene is one of the most widely used plastics, and over 60 million tons are produced worldwide every year. Polyethylene is obtained by the catalytic polymerization of ethylene in gas and liquid phase reactors. The gas phase processes are more advantageous, and use fluidized-bed reactors for production of polyethylene. Since they operate so close to the melting point of the polymer, agglomeration is an operational concern in all slurry and gas polymerization processes. Electrostatics and hot spot formation are the main factors that contribute to agglomeration in gas-phase processes. Electrostatic charges in gas phase polymerization fluidized bed reactors are known to influence the bed hydrodynamics, particle elutriation, bubble size, bubble shape etc. Accumulation of electrostatic charges in the fluidized-bed can lead to operational issues. In this work a first-principles electrostatic model is developed and coupled with a multi-fluid computational fluid dynamic (CFD) model to understand the effect of electrostatics on the dynamics of a fluidized-bed. The multi-fluid CFD model for gas-particle flow is based on the kinetic theory of granular flows closures. The electrostatic model is developed based on a fixed, size-dependent charge for each type of particle (catalyst, polymer, polymer fines) phase. The combined CFD model is first verified using simple test cases, validated with experiments and applied to a pilot-scale polymerization fluidized-bed reactor. The CFD model reproduced qualitative trends in particle segregation and entrainment due to electrostatic charges observed in experiments. For the scale up of fluidized bed reactor, filtered models are developed and implemented on pilot scale reactor.

1 INTRODUCTION

Polymers have various applications in automotive, packaging, chemical, construction, electrical, packaging, and agriculture industries. Widely used polymers fall in the category of thermoplastics and thermosets. The major thermoplastics include low density polyethylene (LDPE), high density polyethylene (HDPE), polypropylene (PP), poly vinyl chloride (PVC), polyethylene terephthalate (PET), polystyrene (PS) and polyamide (PA). Important thermoplastics include polyurethanes (PU), phenolics and epoxy resins. Various commercial reactors are used for the production of thermosets and thermoplastics. These include stirred tank reactors, fluidized beds, plug flow reactors, loop reactors, bubble columns and multizone circulating reactors. These fall in the category of gas-solid systems (fluidized beds, stirred tanks), gas-liquid (bubble columns), and gas-solid-liquid (slurry reactors).

When one surveys the total polymerization marketplace today, thermoplastics represent the major portion of the total production volume. Polyolefins, represent roughly 60 percent of all the thermoplastics produced and sold in the world today. The major types of polyolefins include polypropylene, high-density polyethylene, linear low-density polyethylene, low-density polyethylene, metallocene polyethylene and polypropylene, and various co-polymers and elastomers. The polyolefin family of products serves a wide variety of end-use markets in the major sectors of packaging, automotive, construction, medical, wire and cable and others. Unlike the incremental technological developments more common in other polymers, polyolefin technology developments are significant and routinely leapfrog the existing ones. These tremendous developments in technology impact the whole industry as a unit as well as the high profit sectors. Multiphase reactors and the associated catalyst technology play a key role in polyolefin businesses.

Polyethylene is the most widely used polyolefin in a wide range of applications. For example, it is used to manufacture plastic bags, electrical insulation, plastic tubing, bottles and

packaging materials, and has the advantages of low price, flexibility of molding, and ease of disposal and recycling [3]. Over 60 million tons of polyethylene is produced annually worldwide. It can be produced using gas-phase and liquid-phase processes. In general the gas-phase processes are more advantageous than liquid-phase processes. The activity of most catalysts is approximately 1000 Kg polymer per gram of catalyst and the final polymer need not be separated from the catalyst. In liquid-phase processes the olefin needs to be dried and separated from the solvent [4]. Earlier technologies produced polyethylene at high pressures ($\sim$ 3000 atm). With the advent of catalysts like Ziegler-Natta and metallocene, polyethylene can be produced at low pressures ($\sim$ 20 atm). The available commercial gas-phase reactors are fluidized beds (UNIPOL and Innovene process), vertical stirred-beds (NOVOLEN process), horizontal stirred-beds (AMOCO process) and multizone circulating reactors (Basell process). Of all reactor types, fluidized-beds have become popular due to its excellent mass and heat transfer characteristics.

Although there are several advantages with gas-solid fluidized-bed polymerization reactors, there are also some disadvantages, which researchers are trying to understand and solve. In fluidization, we generally encounter particles of different sizes and/or densities. When gas flows through a bed of such particles different phenomena are observed. Consider a gas-solid system where the density of the particles is the same (as is the case for gas-phase polymerization system), but have a particle size distribution. The dynamic response of one particle size is different from the other primarily due to the size dependence of the drag force exerted by the gas phase. As a general rule, the drag force for a given gas velocity on small catalyst particles will be much larger than on large polymer particles. When the gas flow rate is operated at velocities between the minimum fluidization velocity of the smaller and larger particles a phenomenon known as segregation ([5], [6], [7], [8], [9]) is observed. Fluidized beds operated at velocities higher than the minimum fluidization of all particles results in a well-mixed system. However, at high gas velocities small particles can escape out of the top of the reactor. This phenomenon is called entrainment or elutriation ([10], [11], [12]). The other important phenomena occurring in fluidized-bed polymerization is electrostatics ([13], [14], [15], [16], [17], [18]). Charge generation in a fluidized bed takes place due to particle-

particle and particle-wall collisions. This phenomenon is called tribo-electrification ([19], [20], [21], [22], [23], [24]). Particle agglomerates and sheets forming on the walls of the reactor are specific problems associated with electrostatics in fluidized-bed reactors [1]. Typical locations for fluidized-bed sheeting is shown in Figure 1.1. These sheets grow over a period of time, gain weight and fall over the distributor plate. This plugs the holes of the distributor plate and can cause defluidization and reactor fouling. This has been a serious problem in gas-phase polymerization fluidized-bed reactors. Polymerization reactions are highly exothermic reactions. If the polymer temperature rises above the melting point, the polymer can melt and be a source of thermal agglomeration ([25], [26]) and hot spots ([27], [26], [28], [29]). On the other hand, if the temperature is too low then particles can become brittle producing unwanted fines that must be separated from the outlet gas.

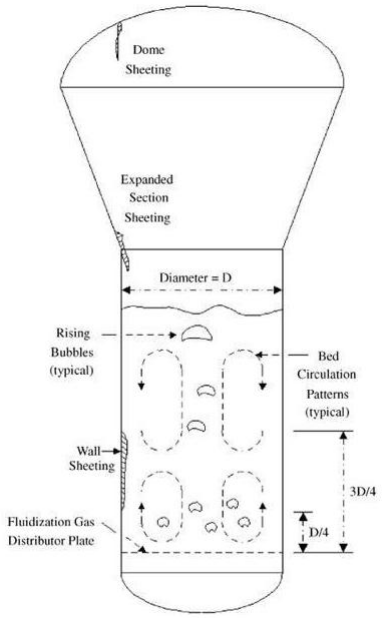

Figure 1.1 Wall and dome sheeting phenomena in gas phase polymerization fluidized-bed reactor. The figure is taken from Hendrickson [1]

In this review only CFD models for olefin polymerization reactors will be discussed. Heat transfer plays an important role in polymer particle overheating. Behjat et al. [25], Dehnavi et al. [30], Mckenna et al. [27] used CFD simulations to compute convective heat-transfer coefficients between polymer particles and the gas phase. They compared the single particle

heat-transfer coefficient results with the Ranz-Marshall correlation and obtained good comparisons. They also analyzed the effects of gas velocity, particle size and shape, and different configurations on the heat-transfer coefficient. Erikkson et al [31] employed CFD to study the influence of initial catalyst particle size on particle growth and the effects of other parameters such as particle interactions on heat transfer. Kaneko et al. [3] used a discrete element model to simulate a small gas-phase olefin polymerization reactor. They did two-dimensional, constant particle size simulations and studied the effects of gas distributor design and particle behavior on hot-spot formation. The works on CFD simulation of pilot and industrial-scale fluidized-bed polymerization reactors are very few. Gobin et al. [32] used a two-fluid modeling approach to simulate a pilot scale and industrial reactors. They utilized two and three-dimensional time-dependent simulations and compared the simulation results of bed height, pressure drop and mean flow properties with experimental results. The work described above assumes a unimodal, single particle size for the polymer. In reality, fluidized-bed polyolefin processes have a wide range of particle sizes. In order to describe phenomena such as segregation and entrainment, a particle size distribution needs to be considered. To describe this case, the multifluid model and chemical reaction engineering model are combined to simulate a pilot-scale fluidized-bed polymerization reactor.

At present, the art of scale-up and design of industrial fluidized-bed reactors is largely empirical [33]. The correlations derived from laboratory-scale reactors are used to build the pilot scale reactors. If these correlations work well at the pilot- plant scale, they are extended to the commercial scale. This process is trial and error since the hydrodynamics in larger units can be vastly different from that in smaller units. For example bubble sizes and wall effects will be different in larger units compared to smaller units, and conversion of the reactants will thus be different. This empirical approach has been adopted because of the difficulty in understanding the gas-solid and solid-solid interactions. In recent years, computational fluid dynamics has emerged as a useful tool for understanding such behavior. With the advent of high-performance computers and improved computational resources, the complex behavior of the underlying gas-solid flows can be understood and used to help in the design process of fluidized-bed polymerization reactors.

There are two primary objectives in this research. The first objective is to develop an electrostatic model from first principles. The next step is to verify and validate the developed electrostatic model. The model is then applied on a pilot plant scale reactor and the observations from simulations and experiments are compared. The second objective is to do develop filtered models for industrial scale reactors. As the simulations on large scale reactors are computationally expensive, subgrid models will be developed for gas-particle flows. The details of the electrostatic and filtered model will be explained in this thesis.

The work is organized as follows. There are five chapters after introduction excluding summary. First, the description of the governing equations of the continuum model is presented. Then, the numerical implementation, verification and validation of the electrostatic model with simple test case and experiments from published literature will be presented. The fourth chapter deals with the application of the electrostatic model to a pilot-plant polymerization fluidized-bed reactor. In this application three cases are considered. The first is the effect of the magnitude of charge on the distribution of solid phases, the second is the continuous injection of catalyst in the fluidized-bed, and the third is the effect of electrostatics on entrainment. The effect of grids used on the computation of electrostatics will also be discussed. Filtered model governing equations and the application of the model on pilot and industrial scale reactors are described in the fifth chapter The sixth chapter deals with the implementation of new aggregation and breakage kernels in poly disperse gas-particle fluidized beds. Finally the summary of the work will be presented.

2 TWO-FLUID MODEL FOR GAS-PARTICLE FLOWS

2.1 Introduction

In principal the hydrodynamics of gas-solid flows can be described by two classes of models, namely the Euler-Lagrange and Euler-Euler models. The Euler-Lagrange models ([3], [34], [35]) solves the newtonian equations of motion for the particle phase and the trajectory of each particle is tracked. The interactions between particles is treated in a hard or soft sphere model. The hard sphere assumes the interactions between particles is instantaneous and binary collisons, whereas in the soft sphere approach the contact forces are calculated from the overlap between particles. The generalized Navier-Stokes equations are used to solve for the gas phase. The Euler-Lagrange models are computationally inefficient for the simulation of large scale reactors and Euler-Euler models are more suitable.

Euler-Euler models ([7], [36], [37]) assume the gas and solid phase as continuous and interpenetrating phases. The equations are the generalization of the Navier Stokes equations for interacting continua. As the solid phase is treated as a continuous phase, closure models are required for the solid stress tensor and the gas-solid drag. The Euler-Euler model are feasable for simulation of commercial scale reactors. In this work the Euler-Euler models are used for simulation pilot-plant scale reactors. The governing equations for the gas and solid phase will be presented in this chapter.

2.2 Governing Equations

The two-fluid model assumes the gas and solid phases as continuum and the instantaneous variables are averaged over a region that is large compared with the particle spacing, but smaller than the flow domain. Each solid phase is described by a unique particle diameter, density and other properties. A phase varible volume fraction is used to distinguish between the different

phases. By definiton the sum of the volume fractions of all phases add to one.

$$\varepsilon_{\mathrm{g}} + \sum_{\alpha=1}^{N} \varepsilon_{\mathrm{s}\alpha} = 1.0 \tag{2.1}$$

where ε_{g} and $\varepsilon_{\mathrm{s}\alpha}$ are the volume fractions of gas and α^{th} solid phase respectively. N refers to the total number of solid phases.

2.2.1 Conservation of Mass

The continuity equation for the gas and particle phase are

$$\frac{\partial}{\partial t}(\varepsilon_{\mathrm{g}}\rho_{\mathrm{g}}) + \nabla \cdot (\varepsilon_{\mathrm{g}}\rho_{\mathrm{g}}\mathbf{u}_{\mathrm{g}}) = 0 \tag{2.2}$$

$$\frac{\partial}{\partial t}(\varepsilon_{\mathrm{s}\alpha}\rho_{\mathrm{s}\alpha}) + \nabla \cdot (\varepsilon_{\mathrm{s}\alpha}\rho_{\mathrm{s}\alpha}\mathbf{u}_{\mathrm{s}\alpha}) = 0 \tag{2.3}$$

where $\mathbf{u}_{\mathrm{g}}$, $\mathbf{u}_{\mathrm{s}\alpha}$ are the gas and α^{th} particle phase velocities. ρ_{g} and $\rho_{\mathrm{s}\alpha}$ are the gas and α^{th} particle phase densities. The first term on the left in Eq. 2.2 and Eq. 2.3 accounts for the rate of mass accumulation per unit volume, and the second term is the net rate of convective mass flux. In this work the right hand side term is considered zero except in Chapter 6, where the volume fractions of the particle phase change due to aggregation and breakage.

2.2.2 Conservation of Momentum

The momentum equation for the gas and particle phase are

$$\frac{\partial}{\partial t}(\varepsilon_{\mathrm{g}}\rho_{\mathrm{g}}\mathbf{u}_{\mathrm{g}}) + \nabla \cdot (\varepsilon_{\mathrm{g}}\rho_{\mathrm{g}}\mathbf{u}_{\mathrm{g}}\mathbf{u}_{\mathrm{g}}) = -\varepsilon_{\mathrm{g}}\nabla p + \nabla \cdot \bar{\bar{\tau}}_{\mathrm{g}} + \sum_{\alpha=1}^{N} f_{\mathrm{g}\alpha} + \varepsilon_{\mathrm{g}}\rho_{\mathrm{g}}\mathbf{g} \tag{2.4}$$

$$\begin{aligned} \frac{\partial}{\partial t}(\varepsilon_{\mathrm{s}\alpha}\rho_{\mathrm{s}\alpha}\mathbf{u}_{\mathrm{s}\alpha}) + \nabla \cdot (\varepsilon_{\mathrm{s}\alpha}\rho_{\mathrm{s}\alpha}\mathbf{u}_{\mathrm{s}\alpha}\mathbf{u}_{\mathrm{s}\alpha}) &= -\varepsilon_{\mathrm{s}\alpha}\nabla p - \nabla p_{\mathrm{s}\alpha} + \nabla \cdot \bar{\bar{\tau}}_{\mathrm{s}\alpha} - f_{\mathrm{g}\alpha} + \\ &\quad \sum_{\alpha=1}^{N} f_{\beta\alpha} + \varepsilon_{\mathrm{s}\alpha}\rho_{\mathrm{s}\alpha}\mathbf{g} + \mathbf{F}_{q\mathrm{s}\alpha} \end{aligned} \tag{2.5}$$

where $\bar{\bar{\tau}}_{\mathrm{g}}$, $\bar{\bar{\tau}}_{\mathrm{s}\alpha}$ are the gas and α^{th} particle phase stress tensor, $f_{\mathrm{g}\alpha}$ is the interaction force between the gas and α^{th} particle phase, $f_{\beta\alpha}$ is the interaction force between the β^{th} and α^{th} particle phases, $\mathbf{g}$ is the gravity contribution, $\mathbf{F}_{q\mathrm{s}\alpha}$ is the electrostatic force acting on the α^{th}

particle phase. The first term on the left in the momentum equations represents the net rate of momentum increase. The second term on the left represents the net rate of momentum transfer by convection. The first two terms on the right in the gas momentum equation are the normal and shear surface stresses, the third term is gas-particle interaction force and the fourth term is the body force. The second and third term term on the right in the particle phase momentum equations are the normal and shear surface stresses. The fourth term represents the gas-particle interaction force, the fifth term is the particle-particle interaction force and the sixth term is the body force.

2.3 Constitutive Relations

To solve the governing equations, closures for the gas and particle phase stress tensor, interaction forces and the electrostatic force are required. The closures for the particle phase stress tensor are obtained from kinetic theory of granular flow (KTGF) and frictional theory. The details of the electrostatic force model are given in Chapter 3. The closures used in this work are described as follows.

2.3.1 Gas-Particle Interaction Force

The drag models widely used in literature are the Gidaspow model [38], Syamlal-O'Brien [39] and Wen-Yu model [40]. Wen-Yu model is applicable in dilute particle flow regime and Gidaspow model can be used for dense regimes. In this work the Gidaspow model is used and follows the Wen-Yu model for $\varepsilon_{\mathrm{g}} > 0.8$ and Ergun equation for $\varepsilon_{\mathrm{g}} \leq 0.8$. Gas-particle drag force is defined as

$$f_{\mathrm{g}\alpha} = K_{\mathrm{s}\alpha\mathrm{g}}(\mathbf{u}_{\mathrm{g}} - \mathbf{u}_{\mathrm{s}\alpha}) \tag{2.6}$$

where $K_{\mathrm{s}\alpha\mathrm{g}}$ is the drag coefficient

$$K_{\mathrm{s}\alpha\mathrm{g}} = \frac{3}{4}\frac{\mathrm{C_d}\varepsilon_{\mathrm{g}}\varepsilon_{\mathrm{s}\alpha}\rho_{\mathrm{g}}\left|\mathbf{u}_{\mathrm{s}\alpha} - \mathbf{u}_{\mathrm{g}}\right|}{d_{\mathrm{s}\alpha}}\varepsilon_{\mathrm{g}}^{-2.65} \qquad \varepsilon_{\mathrm{g}} < 0.8$$

$$K_{\mathrm{s}\alpha\mathrm{g}} = 150\frac{\varepsilon_{\mathrm{s}\alpha}(1-\varepsilon_{\mathrm{g}})\mu_{\mathrm{g}}}{\varepsilon_{\mathrm{g}}d_{\mathrm{s}\alpha}^2} + 1.75\frac{\rho_{\mathrm{g}}\varepsilon_{\mathrm{g}}\left|\mathbf{u}_{\mathrm{s}\alpha} - \mathbf{u}_{\mathrm{g}}\right|}{d_{\mathrm{s}\alpha}} \qquad \varepsilon_{\mathrm{g}} \geq 0.8 \tag{2.7}$$

where $d_{s\alpha}$ is the diameter of the α^{th} particle phase. C_d is defined as

$$C_d = 0.44 \qquad Re_{p\alpha} > 1000$$

$$C_d = \frac{24}{\varepsilon_g Re_{p\alpha}} \left[1 + 0.15(\varepsilon_g Re_{p\alpha})^{0.687}\right] \qquad Re_{p\alpha} \leq 1000$$

$$Re_{p\alpha} = \frac{\rho_g d_{s\alpha} \left|\mathbf{u}_{s\alpha} - \mathbf{u}_g\right|}{\mu_g} \tag{2.8}$$

where $Re_{p\alpha}$ is the α^{th} particle phase reynolds number.

2.3.2 Particle-Particle Drag Interaction

The particle-particle drag force is defined as

$$f_{\beta\alpha} = K_{s\alpha\beta} \left(\mathbf{u}_{s\alpha} - \mathbf{u}_{s\beta}\right) \tag{2.9}$$

$$\begin{aligned} K_{s\alpha\beta} &= 3\left(1 + e_{s\alpha\beta}\right)\left(\frac{\pi}{2} + C_{fr,\alpha\beta}\frac{\pi^2}{8}\right)\frac{\left(d_{s\alpha} + d_{s\beta}\right)^2}{\left(\rho_{s\alpha} d_{s\alpha}^3 + \rho_{s\beta} d_{s\beta}^3\right)} \\ &\quad \left(\frac{\varepsilon_{s\alpha}\varepsilon_{s\beta}\rho_{s\alpha}\rho_{s\beta} g_{0,\alpha\beta}}{2\pi}\right) + C_1 P^* \end{aligned} \tag{2.10}$$

where $K_{s\alpha\beta}$ is the solid-solid exchange coefficient [41]. $e_{s\alpha\beta}$ is the particle coefficient of restitution. A value of 0.8 is used for restitution coefficient in this work. $C_{fr,\alpha\beta}$ is the coefficient of friction between the α^{th} and β^{th} solid phase. $g_{0,\alpha\beta}$ is the radial distribution function between the α^{th} and β^{th} solid phase.

2.3.3 Radial Distribution Function

The radial distribution function g_0 modifies the probability of collision between particles. g_0 is close to one (dilute particle flows) and diverges to infinity at maximum packing in dense systems. There are several relations proposed in literature for radial distribution functions (Ogawa et al [42], Chapman and Cowling [43]). The following formulation [44] is used

$$g_{0,\alpha\beta} = \frac{1}{\varepsilon_g} + \frac{3\left(\sum_{\alpha=1}^{N} \frac{\varepsilon_\alpha}{d_\alpha}\right)}{\varepsilon_g^2 (d_\alpha + d_\beta)} d_\alpha d_\beta \tag{2.11}$$

where d_α, d_β are diameter of α^{th} and β^{th} particle phase respectively.

2.3.4 Solids Pressure

The particle pressure need to be calculated to compute the pressure gradient term $\nabla p_{s\alpha}$ in the solid phase momentum equation. The solids pressure term is composed of a kinetic term (transport) and an additional term due to particle collisions.

$$p_{s\alpha} = \varepsilon_{s\alpha}\rho_{s\alpha}\Theta_{s\alpha} + \sum_{\alpha=1}^{N}(1+e_{s\alpha\beta})g_{0,\alpha\beta}\varepsilon_{s\alpha}\varepsilon_{s\beta}\rho_{s\alpha}\Theta_{s\alpha} \tag{2.12}$$

where $\Theta_{s\alpha}$ is the granular temperature of α^{th} particle phase.

2.3.5 Granular Temperature

The granular temperature of a solid phase is proportional to the kinetic energy of the random motion of the particles. The transport equation for granular temperature of the α^{th} solid phase is of the form

$$\begin{aligned}\frac{3}{2}\left[\frac{\partial}{\partial t}\left(\rho_{s\alpha}\varepsilon_{s\alpha}\Theta_{s\alpha}\right) + \nabla\cdot\left(\rho_{s\alpha}\varepsilon_{s\alpha}\Theta_{s\alpha}\mathbf{u}_{s\alpha}\right)\right] &= \left(-p_{s\alpha}\bar{\bar{\mathbf{I}}} + \bar{\bar{\tau}}_{s\alpha} : \nabla\mathbf{u}_{s\alpha}\right) + \nabla\cdot\left(k_{\Theta_s}\nabla\Theta_{s\alpha}\right) \\ &\quad -\gamma_{\Theta_{s\alpha}} + \phi_{gs\alpha}\end{aligned} \tag{2.13}$$

where $\left(-p_{s\alpha}\bar{\bar{\mathbf{I}}} + \bar{\bar{\tau}}_{s\alpha} : \nabla\mathbf{u}_{s\alpha}\right)$ is the generation of energy by the solid stress tensor, $k_{\Theta_s}\nabla\Theta_{s\alpha}$ is the diffusion of energy, $\gamma_{\Theta_{s\alpha}}$ is the collisional dissipation of energy, $\phi_{gs\alpha}$ is the energy exchange between gas and α^{th} solid phase, k_{Θ_s} is the diffusion coefficient. The diffusion coefficient of granular energy k_{Θ_s}(Syamlal Model) is given by

$$k_{\Theta_s} = \frac{15 d_{s\alpha}\varepsilon_{s\alpha}\sqrt{\Theta_{s\alpha}\pi}}{4(41-33\eta)}\left[1 + \frac{12}{5}\eta^2(4\eta-3)\varepsilon_{s\alpha}g_{0,s\alpha} + \frac{16}{15\pi}(41-33\eta)\eta\varepsilon_{s\alpha}g_{0,s\alpha}\right] \tag{2.14}$$

where $\eta = \frac{(1+e_{ss})}{2}$. The collisional dissipation of energy $\gamma_{\Theta_{s\alpha}}$ represents the rate of energy dissipation due to collisions between particles. This is given by

$$\gamma_{\Theta_{s\alpha}} = \frac{12(1-e_{ss}^2 g_{0,s\alpha})}{d_{s\alpha}\sqrt{\pi}}\rho_{s\alpha}\varepsilon_{s\alpha}\Theta_{s\alpha}^{3/2} \tag{2.15}$$

The transfer of the kinetic energy of random fluctuations in particle velocity from the α^{th} solid phase and gas phase is represented by $\phi_{gs\alpha}$

$$\phi_{gs\alpha} = -3K_{gs\alpha}\Theta_{s\alpha} \tag{2.16}$$

In this work an algebraic formualtion is used where the convection and the diffusion term in the transport equation are neglected.

2.3.6 Solids Shear Stresses

The solid shear stress tensor contains the shear and bulk viscosities arising from particle momentum exchange due to translation and collision. A frictional component is also included to account for the viscous-plastic transistion that occurs when particles of a solid phase reach a maximum solid volume fraction.

$$\mu_{s\alpha} = \mu_{s\alpha,\text{col}} + \mu_{s\alpha,\text{kin}} + \mu_{s\alpha,\text{fr}} \tag{2.17}$$

where $\mu_{s\alpha,\text{col}}$ is the collisional viscosity [44], $\mu_{s\alpha,\text{kin}}$ is the kinetic viscosity [44] and $\mu_{s\alpha,\text{fr}}$ is the frictional viscosity [45].

$$\mu_{s\alpha,\text{col}} = \frac{4}{5}\varepsilon_{s\alpha}\rho_{s\alpha}d_{s\alpha}g_{0,s\alpha}(1+e_{s\alpha})\left(\frac{\Theta_{s\alpha}}{\pi}\right)^{1/2}\varepsilon_{s\alpha} \tag{2.18}$$

$$\lambda_{s\alpha} = \frac{4}{3}\varepsilon_{s\alpha}\rho_{s\alpha}d_{s\alpha}g_{0,s\alpha}(1+e_{ss})\left(\frac{\Theta_{s\alpha}}{\pi}\right)^{1/2} \tag{2.19}$$

$$\mu_{s\alpha,\text{kin}} = \frac{\varepsilon_{s\alpha}d_{s\alpha}\rho_{s\alpha}\sqrt{\Theta_{s\alpha}\pi}}{6(3-e_{ss})}\left[1+\frac{2}{5}(1+e_{ss})(3e_{ss}-1)\varepsilon_{s\alpha}g_{0,ss}\right] \tag{2.20}$$

$$\mu_{s\alpha,fr} = \frac{p_{s\alpha}\sin\phi}{\sqrt{I_{2D}}} \tag{2.21}$$

where $p_{s\alpha}$ is the solid pressure of α^{th} solid phase, ϕ is the angle of internal friction, and I_{2D} is the second invariant of the deviatoric stress tensor.

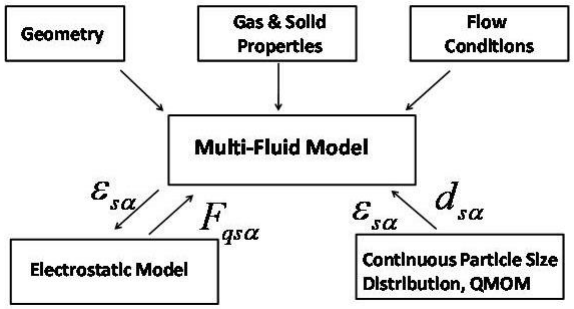

Figure 2.1 Algorithm for coupling between electrostatics and multi-fluid CFD model.

Multiphase Interphase Flow Exchanges (MFIX) and OpenFOAM (open source codes) and ANSYS FLUENT commerical CFD software are used in this thesis. The CFD software mentioned above are based on finite volume method. Grid generation is done using Gambit software and ANSYS Meshing. Given a catalyst size distribution, a reaction engineering model [6] is used to obtain the polymer size distribution. Simulations are run with multi-fluid model, initialized with the polymer size distribution. The algorithm for the coupling between the multi-fluid model, electrostatic model and quadrature method of moments (QMOM) is shown in Figure 2.1. In the next chapter the development, verification and validation of the electrostatic model will be presented.

3 ELECTROSTATIC MODEL

3.1 Introduction

Gas-solid flows are present in various industrial processes such as pneumatic conveyors, fluidized-beds, coal combustion and polymerization reactors. Due to particle-particle and particle-wall collisions, charge develops on the particles and this phenomena is known as tribo-electrification. The charged particles effect the hydrodynamics of the fluid flow and can cause channeling in pneumatic conveyors, defluidization and reactor fouling in fluidized-bed reactors. To describe these phenomena an electrostatic model is required and coupled with the existing CFD multi-fluid models.

Previous literature shows there are two works where an electrostatic force model is used in the area of two-dimensional bed with a central jet and riser flows. Both the models are based on the two-fluid eulerian-eulerian approach. Shih et al. [46] used an electric force (F = qE) acting on particle with charge (q) and the applied electric field (E) on a two dimensional bed with a central jet. They assumed a fixed charge on the particles and a constant value for the applied electric field. The bed consisted of coal (250 micron size) and pyrite (150 micron size) particles. The objective was to separate pyrites from coal. Both the particles had positive charge. Their simulations showed difference in bubble frequency, shape and size when the electric field is zero and constant value.

Mahdi et al. [9] studied the effect of static electrification in vertical riser flow. A steady, fully developed gas-solid flow model is used and a poisson equation for the electric field is solved. The particles were assumed to be monodisperse and a prescribed fixed charge. They observed radial segregation of particles and compared their results with published literature. In the present work a poisson equation for the electric potential is solved and coupled with the multi-fluid CFD model. Time-dependent electric field is computed. The electrostatic model is applied for a polydisperse flow with a fixed size dependent charge.

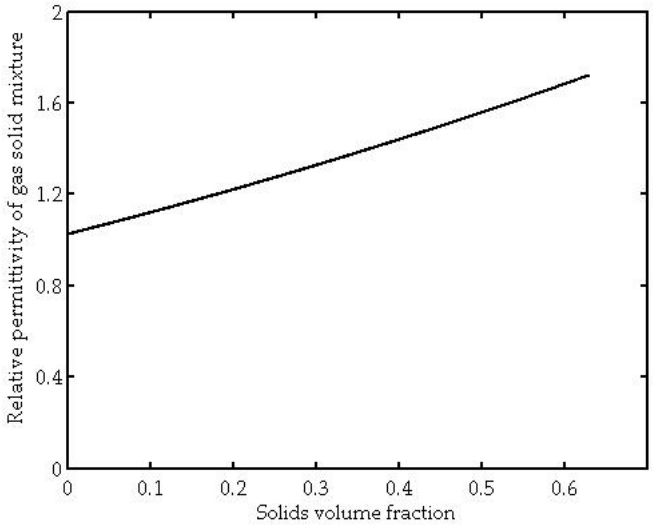

Figure 3.1 Permittivity of gas-solid mixture.

3.2 Model Description

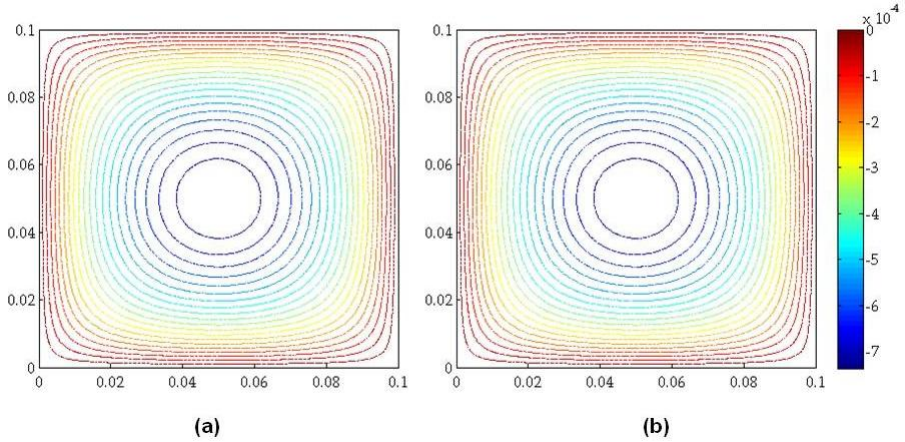

Figure 3.2 Contours of electric potential in volts (a) Fluent (b) Matlab.

The governing equations describing electromagnetic phenomena can be obtained from the well-known Maxwell equations [47]. The Maxwell equations are a set of four partial differential equations namely, Gauss's law for the electric field, Gauss's law for the magnetic field, Faraday's law of induction, and Ampere's law. These laws, along with the Lorentz force equation, describe the force acting on a point charge in the presence of electromagnetic fields. The Lorentz force

equation:

$$\mathrm{F} = \mathrm{q}(\mathrm{E} + v \times \mathrm{B}) \tag{3.1}$$

consists of two terms: the force due to the electric field $\mathrm{F}_e = \mathrm{qE}$ and the force due to magnetic fields $\mathrm{F_m} = \mathrm{q(v \times B)}$. A simple analysis comparing the electrostatic and magnetic forces indicates that the force due to the magnetic field can be neglected if the velocity of the charged particle is much less than the speed of light. In most applications of gas-solid flows the particle phase velocity is much less than the speed of light and hence the force due to the magnetic field can be neglected. The Lorentz force can then be reduced to F = qE. Based on this analysis, force due to electric field is sufficient to describe the force acting on a charged particle in gas-solid flows. Gauss's law in differential form is

$$\nabla \cdot D = \rho \tag{3.2}$$

where D is the electric displacement vector, ρ is the charge density, and ∇ is the gradient operator. The relation between the electric displacement and the electric field is

$$D = \in_0 E + P \tag{3.3}$$

where P is the induced polarization, and $\in_0$ is the permittivity of a vacuum. A constitutive relation is used to relate the induced polarization and electric field for an isotropic medium:

$$P = \in_0 \chi_e E \tag{3.4}$$

where χ_e is the electric susceptibility of the medium and $1 + \chi_e$ is the relative permittivity, which is measurable and its value can be found in literature. The electric field can then be equated to charge density as

$$\nabla \cdot (\in_m \in_0 E) = \rho \tag{3.5}$$

where $\in_m = 1 + \chi_e$.There are several equations available in literature for calculating the relative permittivity of the gas-solid mixture as a function of solids volume fraction. Some of the models are Looyenga, Bottcher and Bordewijk, Bruggeman, Iglesias-Peon, Kraszewski [48]. In this work the Bruggeman equation is used. It is important to note that all the above stated models gave similar expressions for the relative permittivity of the mixture as a function of

solids volume fraction. The relative permittivity $\in_m$ for a gas-solid mixture can be obtained from the Bruggeman equation [48].

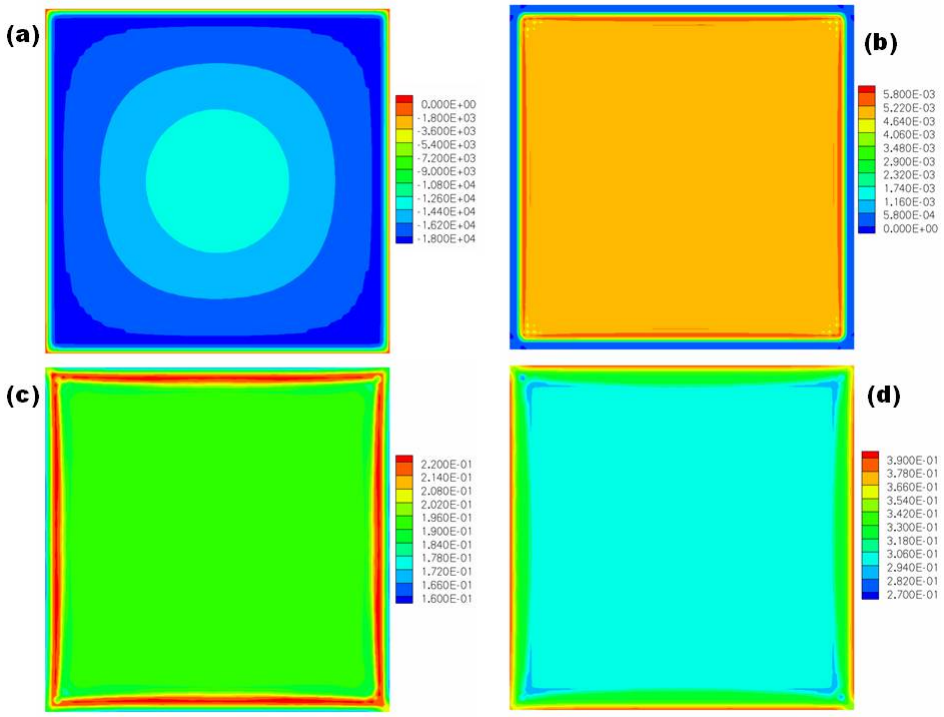

Figure 3.3 Instantaneous contours of electric potential and solid volume fractions at t=0.6 sec for zero potential wall boundary condition: (a) electric potential, (b) solid phase 1, (c) solid phase 2, (d) solid phase 3.

Table 3.1 Properties of phases used in the verification of the electrostatic model

Solid Phase	Small	Medium	Large
density, kg/m^3	843.0	843.0	843.0
diameter, μm	523.0	1176.0	1751.0
particle volume fraction	0.00453	0.1943	0.310
charge, coulomb/m^3	0.1081	-0.001	-0.00115
Gas Mixture			
density, kg/m^3	22.1		
viscosity, kg/(ms)	1.427e-05		

$$\varepsilon_g = \frac{\in_{\mathrm{s}} - \in_{\mathrm{m}}}{\in_{\mathrm{s}} - \in_{\mathrm{g}}} \left(\frac{\in_{\mathrm{g}}}{\in_{\mathrm{m}}} \right)^{\frac{1}{3}} \tag{3.6}$$

which calculates the permittivity of the gas-solid mixture if the relative permittivity of pure gas and solid are known. ε_{s} is the volume fraction of solid phase, $\in_{\mathrm{s}}$ is relative permittivity of

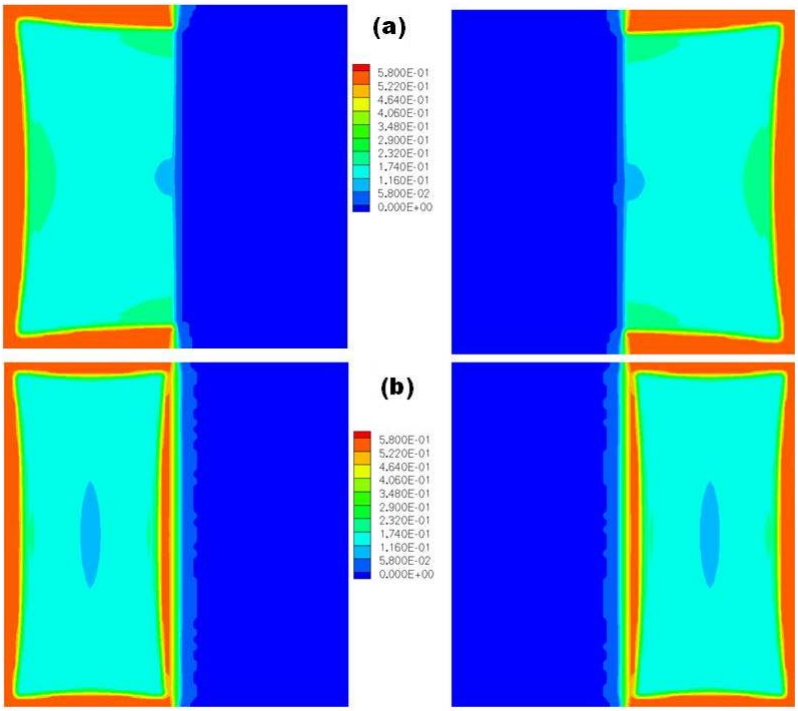

Figure 3.4 Instantaneous contours of solid volume fractions at t= 0.003 sec for zero potential wall boundary condition: (a) same polarity, (b) opposite polarity.

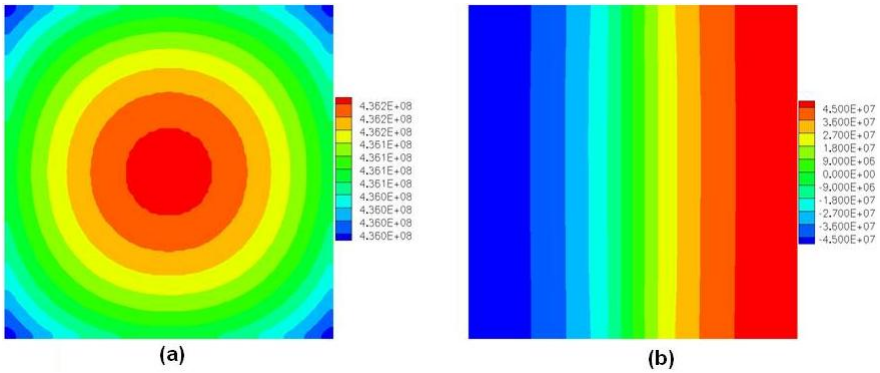

Figure 3.5 Instantaneous contours of electric potential for zero flux boundary condition: (a) same polarity, (b) opposite polarity.

Table 3.2 Properties of phases used in the verification of Coulomb's law

Solid Phase	Solid Phase-1	Solid Phase-2
density, kg/m^3	843.0	843.0
diameter, μm	500.0	500.0
particle volume fraction	0.25	0.25
case1 coulomb/m^3	0.1	0.1
case2 coulomb/m^3	-0.1	0.1

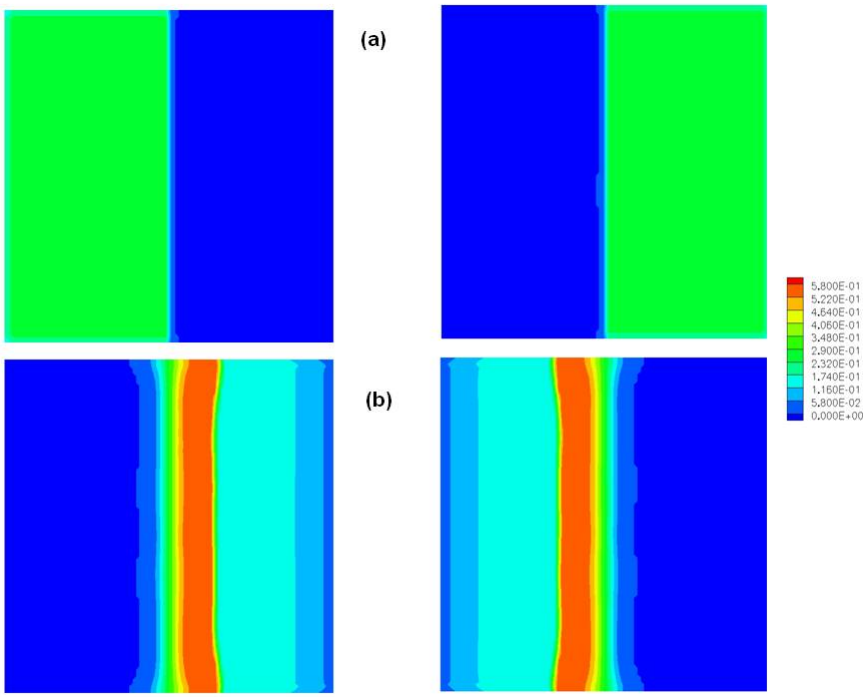

Figure 3.6 Instantaneous contours of solids volume fraction for zero flux boundary condition: (a) same polarity, (b) opposite polarity.

polyethylene (2.25 ([49], [50], [51])), $\in_{\mathrm{g}}$ is the relative permittivity of gaseous mixture (1.026), and $\in_{\mathrm{m}}$ is the relative permittivity of gas-solid mixture. The relative permittivity of gaseous mixture is obtained from a known composition of ethylene [52] and nitrogen [53] and their respective relative permittivities. The permittivity of gas-particle mixture from Eq. (3.6) is plotted as a function of the solids volume fraction in Figure 3.1. Using a linear fit to these data, we find

$$\in_{\mathrm{m}} = 0.97 + 1.20\varepsilon_{\mathrm{s}} = \varepsilon_{\mathrm{g}} \left(\frac{2.17}{\varepsilon_{\mathrm{g}}} - 1.20 \right) \tag{3.7}$$

which is more convenient for finding $\in_{\mathrm{m}}$ given ε_{s} than Eq. (3.6). The total electric charge density ρ is given by

$$\rho = \sum_{\alpha=1}^{N} q_{\mathrm{s}\alpha} \varepsilon_{\mathrm{s}\alpha} \tag{3.8}$$

where $q_{\mathrm{s}\alpha}$ is the charge on the α^{th} solid phase per unit volume and $\varepsilon_{\mathrm{s}\alpha}$ is the volume fraction of the α^{th} solid phase. Substituting the permittivity of the gas-solid mixture and charge density in the electric field equation, we have an equation for the electric field given the particle charge:

$$\nabla \cdot \left(\varepsilon_{\mathrm{g}} \left(\frac{2.17}{\varepsilon_{\mathrm{g}}} - 1.20 \right) E \right) = \frac{\sum_{\alpha=1}^{N} q_{\mathrm{s}\alpha} \varepsilon_{\mathrm{s}\alpha}}{\in_0} \tag{3.9}$$

The curl of the electric field is zero ($\nabla \times E = 0$) [62] and the scalar potential φ is defined as

$$E = -\nabla\varphi \tag{3.10}$$

Substituting for the electric field in Eq. (3.9) a Poisson equation for the electric potential is formed:

$$\nabla \cdot \left(\varepsilon_{\mathrm{g}} \left(\frac{2.17}{\varepsilon_{\mathrm{g}}} - 1.20 \right) \nabla\varphi \right) = -\frac{\sum_{\alpha=1}^{N} q_{\mathrm{s}\alpha} \varepsilon_{\mathrm{s}\alpha}}{\in_0} \tag{3.11}$$

This Poisson equation is coupled with the multi-fluid CFD model through the volume fractions of the gas and solid phases, and thus must be solved at every time step in the CFD simulation. In this work, the wall boundary condition for electric potential is zero (i.e., the walls are assumed to be grounded). The gradient of the electric potential found by solving Eq. (3.11) is used to obtain the electrostatic force. The electrostatic force acting on the α^{th} solid phase is

$$\mathrm{F}_{\mathrm{qs}\alpha} = -\mathrm{q}_{\mathrm{s}\alpha} \varepsilon_{\mathrm{s}\alpha} \nabla\varphi \tag{3.12}$$

The steady-state charge $\mathrm{q}_{\mathrm{s}\alpha}$ as a function of particle size is a required input for the model. Note that the electrostatic force is a function of charge and solids volume fractions $\varepsilon_{\mathrm{s}\alpha}$ hence, the multi-phase CFD model and Eq. (3.11) must be solved in a fully coupled manner.

3.2.1 Coupling of Electrostatic and Multi-Fluid Models

As described above, the electrostatic model needs to be coupled with the multi-fluid CFD model. The algorithm for the coupling is as follows.

Step 1: Solve the multi-fluid model equations shown in chapter 2 at every grid point. From the multi-fluid model we obtain the volume fractions of the gas and solid phases.

Step 2: Solve the Poisson equation (Eq. 3.11) for the electric potential using the volume fractions of the gas and solid phases from step 1 and the user-defined specified charges.

Step 3: Evaluate the electrostatic force (Eq. 3.12) using the gradient of the electric potential.

Step 4: Add electrostatic force to each of the solid-phase momentum equations and repeat steps 1-4 for the next iteration.

3.2.2 Verification of the Electrostatic Model

In this section the numerical implementation of the electrostatic model in FLUENT 6.3 is discussed. After the numerical implementation of the electrostatic model, the generic Poisson solver in FLUENT is verified by solving a simple test case with uniform volume fractions. After the verification of the Poisson solver, the multi-fluid CFD model is coupled with the electrostatic model and segregation due to electrostatics is studied using a simple test case where the volume fractions evolve due to the electrostatic force. Finally, a test case that verifies Coulombs law is performed.

3.2.2.1 Numerical implementation of the electrostatic model

FLUENT 6.3 has an option to solve for a user-defined scalar (UDS) field. The UDS for a multiphase system in FLUENT has the form

$$\frac{\partial}{\partial t}(\varepsilon_{\mathrm{g}}\rho_{\mathrm{g}}\varphi) + \nabla\cdot(\varepsilon_{\mathrm{g}}\rho_{\mathrm{g}}\mathbf{u}_{\mathrm{g}}\varphi - \varepsilon_{\mathrm{g}}\Gamma_{\mathrm{g}}\nabla\varphi) = S_{\mathrm{g}} \tag{3.13}$$

The electric potential equation (Eq. 3.11) does not have the unsteady and convection terms. By canceling the unsteady and convection terms, the final form of the UDS equation is

$$\nabla\cdot(\varepsilon_{\mathrm{g}}\Gamma_{\mathrm{g}}\nabla\varphi) = -S_{\mathrm{g}} \tag{3.14}$$

where $\Gamma_{\mathrm{g}} = \left(\frac{2.17}{\varepsilon_{\mathrm{g}}} - 1.20\right)$ and $S_{\mathrm{g}} = \frac{\sum_{\alpha=1}^{N} q_{\mathrm{s}\alpha}\varepsilon_{\mathrm{s}\alpha}}{\in_0}$. This equation is solved at every time step using the built-in Poisson equation solver in FLUENT.

3.2.2.2 Verification of Poisson solver

The objective of this simulation is to check the generic UDS solver. A simple Poisson equation of the form

$$\nabla^2\varphi = -1(-1) \tag{3.15}$$

is solved on a square domain in FLUENT and in MATLAB. The source term in the equation is negative and it is chosen to simplify the computation. The electric potential boundary condition

is zero at the walls. Note that there is no gas or solid flow and so the multi-fluid CFD model equations are not solved in this simulation. Contours of electric potential obtained are shown in Figure 3.2. As the source term is negative the computed electric potential is negative at the center of the square domain and zero near the walls. The contours plots obtained from simulations of FLUENT and MATLAB compare well and thus the generic UDS solver can be used to solve for electric potential with confidence.

Table 3.3 Experimental conditions

U/Umf	0.4
Gas velocity, (m/s)	0.522
Fluidization regime	Slugging
Column diameter, (m)	0.10
Column height, (m)	1.27
Charge of fine particles, (nC/Kg)	33395.8
Charge of wall particles, (nC/Kg)	-42820.9
Charge of dropped particles, (nC/Kg)	-706.1
Weight % of fine particles	0.45
Weight % of wall particles	1.54
Weight % of dropped particles	95.78

Table 3.4 Properties of gas and solid phase used in the simulation

Solid Phase	Fine Particles	Wall Particles	Dropped Particles
mass %	0.50	3.50	96.0
density, kg/m^3	843.0	843.0	843.0
diameter, μm	134.4	431.0	660.0
volume fraction	0.0023388	0.0163716	0.449
charge, coulomb/m^3	0.02815	-0.0360	-0.000595
Gas Phase			
density, kg/m^3	4.93		
viscosity, kg/(ms)	1.821e-05		

3.2.2.3 Verification of the complete algorithm

The objective of this simulation is to check the total algorithm described in Section 2.1. The multi-fluid CFD model coupled with the electrostatic model is solved on a square domain. The width of the square domain is equal to the diameter of a pilot-plant reactor (D $\sim$ 0.4-0.6m). There are no inlets or outlets and no gravitational forces in this test case. In reality the gravity

plays an important role in the segregation of the particles with wide particle size distribution. The gas and solid phases are initialized with zero velocity and uniformly distribution on the square domain. The goal of this test case is to observe if any segregation occurs due to the presence of charges on the solid phases. The wall boundary condition for the electric potential is zero. To approximate realistic conditions, the multi-fluid CFD model is used to solve for one gas and three solid phases. The gas- and solid-phase properties are shown in Table 3.1. From Table 3.1 we see that the mean charge is negative, small particles have positive charge, medium and large particles have negative charge. The solid phase density is approximated to polyethylene density, and the diameter and volume fractions of the solid phases, representative of actual polymerization reactors, are obtained from the quadrature method of moments [7].

The electric potential evolves as the simulation progresses due to segregation of charged particles. The instantaneous contours of electric potential and volume fractions of all solid phases are shown in Figure 3.3. A non-uniform electric field develops due to the presence of charged particles, and the gradient of the electric potential causes the particles to segregate inside of the square domain. As seen from the contour plot, the electric potential is zero at the walls and negative at the center of the domain. The electric field points from a region of a high potential towards low potential. Any positively charged particle will move from the high to the low potential and vice-versa for a negatively charged particle. In this simulation the negatively charged larger particles move towards the walls, and the positively charged small particles towards the center of the domain. At t=0.6 sec, a band of solid phase is formed with the larger particles found near the wall, and the medium size particle sandwiched in between the large and small particles. A higher volume fraction of large particles is found near the walls because of the presence of high charge on them. Another simulation was performed with zero charge on all the solid phases and no segregation of particles was observed. From these simulations, we can conclude that segregation is observed only due to electrostatics, and that the fully coupled CFD model is able to capture particle segregation due to electrostatics. It is important to note the typical computation time of the fully coupled model and the multi-phase CFD model with electrostatics. For a two-dimensional pilot plant scale simulations the fully coupled model computes 10-10.5 sec and the multi-phase CFD model calculates 9.5-10

sec of flow time in one day on a high performance parallel computing machine at Iowa State University. These typical computation times show that the inclusion of the electrostatic model does not add extra computational resources.

3.2.2.4 Verification of basic law of electrostatics

The aim of these test cases is to verify that the fully coupled CFD model is able to capture the phenomenon where like charges repel and unlike charges attract. The multi-fluid CFD model solves for one gas and two solid phases in a square domain. The properties of the gas and solid phases are shown in Table 3.2. The left half of the square domain is filled with a volume fraction of 0.25 of solid phase 1, and the right half of the square domain with volume fraction of 0.25 of solid phase 2. The density and particle size of both solid phases are the same. Two cases are run to illustrate that the model predicts that like charges repel and unlike charges attract. In the first case the magnitude and polarity on both phase are the same, and in the second case the magnitude is same but opposite in polarity. The electric potential at the walls is zero. Figure 3.4(a) shows the instantaneous volume fraction of solid phases 1 and 2 for the first case. Since the solid phases have the same polarity they repel each other. In the second case shown in Figure 3.4(b), the solid phases are attracted to each other along the centerline. These simulations verify that the fully coupled CFD model is able to capture the basic phenomena observed in electrostatics.

Verification cases are also done with zero-flux boundary condition for the electric potential. Two cases are run similar to zero potential boundary condition. In the first case the magnitudes and polarities on both phases are the same, and in the second case the magnitudes are the same but they are opposite in polarity. Figure 3.5 shows the instantaneous contours of electric potential for the same and opposite charge cases. In the case for opposite polarity, particles segregate towards the center of the square domain as shown in Figure 3.6(a). When the solid phases have the same polarity and zero-flux boundary conditions (Figure 3.6(b)), the particles behave as neutral and no segregation is observed. The electric potential is uniform and the gradient of the potential, which causes segregation, is zero.

3.3 Electrostatic Model Validation

Sowinksi et al [2, 54] used an online Faraday cup technique to measure the electrostatic charge of the particles in their entirety using a lab-scale gas-solid fluidized-bed. The system was operated with dry air and with a wide size distribution of commercially produced polyethylene particles. The experiments were conducted at two different fluidization regimes, bubbling and slug flow. Bipolar charging was observed with fine entrained particles being predominantly positively charged and the bulk bed particles being predominantly negatively charged. The charge-to-mass ratio (q/m) of the particles was measured and used as an input to the electrostatic model. Solid phase distribution in the CFD simulations were compared with the experimental observations. The remainder of this article is organized as follows. First, the description of the experiments is presented where the experimental set-up, procedure conditions, and observations will be described. The second section discusses the CFD model, simulation parameters and boundary conditions. The third section describes the simulation results and comparison with experiments. The final section summarizes the conclusions of this work.

3.3.1 Experimental Set Up

The following section gives a brief summary of the experimental set up, procedure, overview of conditions and observations. For more details, refer to Sowinski et al. [2]. A schematic diagram of the experimental set-up is shown in Figure 3.7. The fluidization column is made of carbon steel with a 0.0859 m inner diameter and 1.27 m in height. The cylindrical column consists of two online Faraday cups, one at the top and the other at the bottom, below the distributor plate. A filter bag at the top of the column is used to capture the entrained fines and a modified knife gate valve is used as the distributor plate. A Faraday cup is used as an online technique that enables the measurement of the overall net particle charge. The bottom Faraday cup measures the bulk charge on bed particles and the top Faraday cup measures the cumulative charge of the entrained fine particles. Dry air or nitrogen is used as the medium to fluidize polydisperse polyethylene particles.

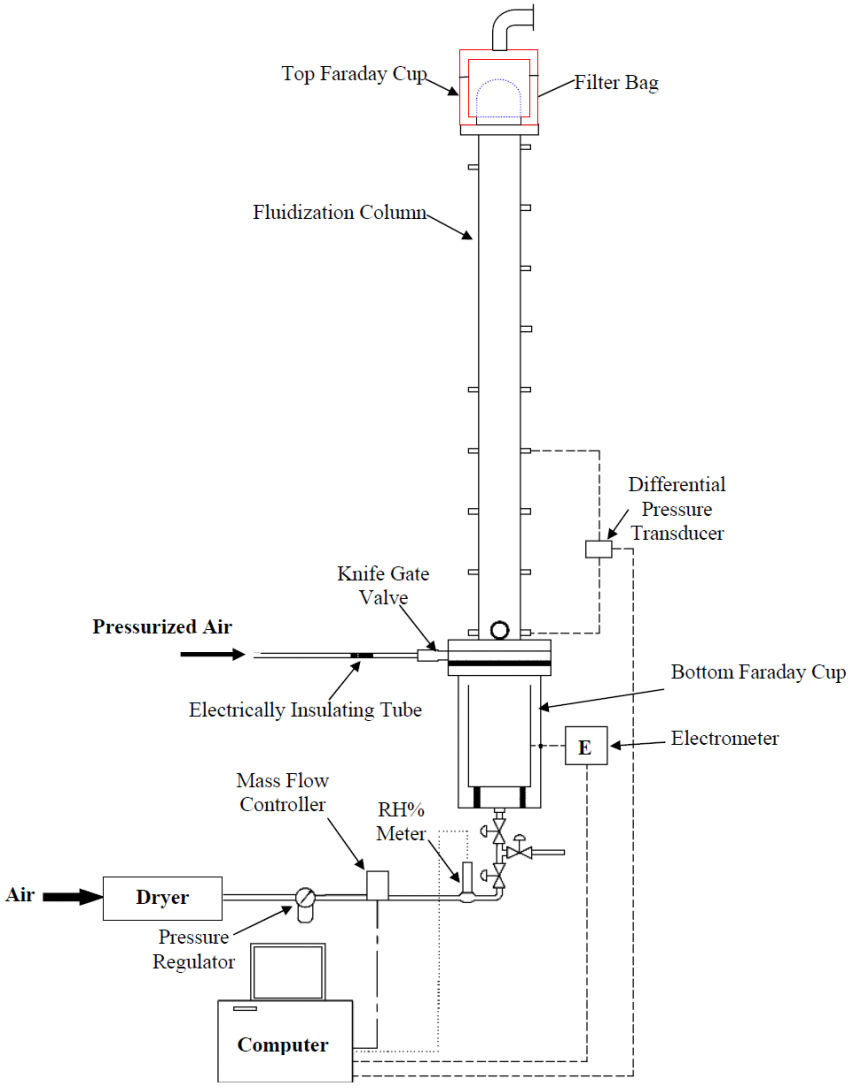

Figure 3.7 Experimental set up of lab scale fluidized-bed (copied from Sowinski et al. [2]).

3.3.2 Experimental Procedure

The experiments were performed to investigate the effect of fluidization gas velocity on the electrostatic charges generated inside the bed. Before each run the entire system is purged with fluidizing medium and cleaned to remove any particles adhered to the wall. The fluidization column and the distributor plate are grounded to remove any accumulated charge between experiments. The charge and mass of a sub-sample the INITIAL particles is measured before they are placed inside the fluidization column. Particles are fluidized at a desired superficial gas velocity for a set period of time. After the completion of the fluidization period, the fluidizing gas is turned off. The filter bag is removed, and the charge and mass of the entrained fines is measured. A sample of fines is then used for particle size analysis. These entrained particles are called FINES. The knife gate valve, which acts as distributor plate, is opened to allow the bed particles to drop into the bottom Faraday cup. The mass and net charge of bed particles is measured. These particles are referred as DROPPED. If any particles are observed to be sticking to the column wall, their layer thickness and height are measured. These particles are referred as WALL. The charge of wall particles was measured by tapping the sides of the column to deposit several of these into the bottom Faraday cup. The particle size analysis of the dropped and wall particles was also performed. From the analysis, the mean particle size of FINES, WALL and DROPPED particles is obtained and used in the CFD simulations.

3.3.3 Overview of Experiments

The fluidization gas velocity is varied and it corresponds to two fluidization regimes, namely the bubbling and slug flow regimes. The gas velocity and mean particle size for each regime are shown in Table 3.5. The CFD simulations are performed with one gas phase and three particle phases (FINES, DROPPED and WALL). Particle mass, net charge and the mean size of each group (FINES, DROPPED and WALL) measured after fluidization are used to initialize the CFD model. The particle mass is used to compute the initial volume fraction and the net charge is used to calculate the electrostatic forces. The CFD model does not include charge generation, dissipation or transfer between particle-particle collisions or particle-wall collisions

and so charge on the particle phases is assumed to remain constant during the simulation.

Table 3.5 Experimental conditions, $\mathbf{U}_{\mathrm{mf}} = 0.131\mathrm{m/s}$

Flow Regime	$\mathbf{U}/\mathbf{U}_{\mathrm{mf}}$	DROPPED, μm	WALL, μm	FINES, μm
Bubbling	1.5	712.3	346.4	69.2
Slug Flow	4.0	660.1	431.3	134.4

3.3.4 Experimental Results

Before each run the initial net charge of the particles was measured by a bench-scale Faraday cup using a small sample from the initial bed mass. The details of the measurement technique are not described here and can be found in [2]. The bulk charge measured before fluidization is predominantly negative for all experimental runs. The entrained fine particles (FINES) are captured by the filter and found to be positively charged. After fluidization is stopped, the charge of the bed particles was measured in two sections. The particles that dropped when the distributor plate was opened (DROPPED) and the particles that were stuck to the wall of the column (WALL). First the charge on the DROPPED particles and then the WALL particles were measured by taking a picture of the wall layer from below and performing some analysis. The thickness and the height of the WALL particles attached to the column wall were also measured. The charge of WALL particles is then measured by tapping the side of the column. Both the dropped and wall particles were predominantly negatively charged and it is important to note that the wall particles had a higher charge-to-mass ratio compared to the dropped particles.

Figure 3.8 shows the particle segregation observed in the experiments, with the fines at the top of the bed, wall particles at the column wall close to the distributor plate and the dropped particles at the center of the bed. Table 3.6 shows the mass and charge of each particle group in the bubbling and slug flow regimes. Table 3.7 shows the height and thickness of the particles attached to the wall in both flow regimes. Ideally, given the initial particle size distribution, the CFD simulation should predict the mean size of each particle group, charge and segregation pattern. Such predictions are beyond the capabilities of the current multi-fluid and electrostatic model. In the current CFD simulations, the mean particle size and charge

from the experiments for each particle group are used as an input to predict the hydrodynamic and electrostatic segregation.

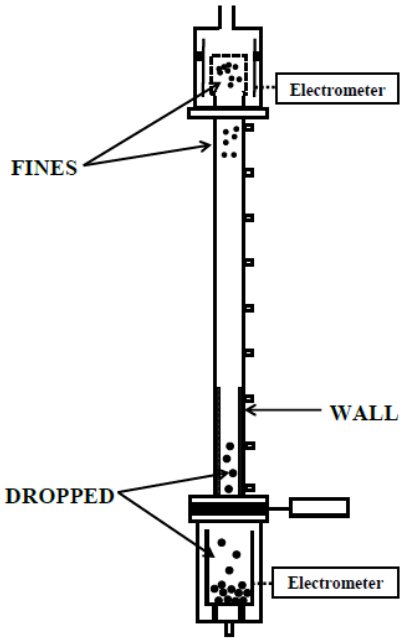

Figure 3.8 Particle distribution of the FINES, DROPPED and WALL particles after fluidization.

Table 3.6 Experimental measurements

	Regime	Mass, g	Charge, μC/Kg
DROPPED	Bubbling	1023.04	-0.6686
	Slug	1009.04	-0.7061
WALL	Bubbling	22.82	-54.670
	Slug	16.26	-42.821
FINES	Bubbling	0.66	20.768.
	Slug	4.71	33.396

3.4 CFD Simulation Conditions and Parameters

The fluidized-bed in Fig. 3.7 is a cylindrical column with 0.0859 m inner diameter and 1.27 m in height. The center plane of the bed is used and simulated as a two-dimensional geometry. A three dimensional simulation would be realistic, but is computationally expensive

Table 3.7 Experimental observations

WALL particles	Thickness, mm	Height, mm
Bubbling	0.5-0.75	300
Slug Flow	2-3	100

for simulating one gas and three solid phases. The thickness of wall coating is small (0.5 - 3 mm) and a two-dimensional simulation can be run to represent the fluidized-bed. A uniform grid size of 4 mm are used in all the simulations. This grid size is used, so as to balance the accuracy of results with computational time. The uniform grid size can be used to represent the macro scale behavior such as bed height, pressure drop, bubble shape and bubble dynamics. To simulate the thickness of wall coating a refined non uniform grid with 2.5 mm grid size at the center and 1 mm grid near the wall is also used. The initial bed height is 0.34 m with the total solids volume fraction of 0.63. The initial volume fraction and charge of each particle phase is shown in Table 3.8. The volume fraction is computed based on the mass of each particle phase (FINES, WALL, DROPPED) after fluidization, from the experiment. The particle charge measured in the experiments is multiplied by the particle density and the resulting charge density is used as an input in the model. Simulation conditions are shown in Table 3.9. The simulations are divided in two stages. At flow time equal to zero, the three particle groups are uniformly distributed. In the first stage, simulations are run from flow time equal to zero to eighty seconds. The last seventy seconds are time averaged. At flow time equal to eighty seconds, the gas flow is stopped and the bed is allowed to settle. In the second stage, after the bed is settled the gas velocity inlet boundary condition is changed to pressure outlet and the particles are allowed to drop down. The simulations are run for twenty seconds of flow time for particles with and without charge for both flow regimes. With the non-uniform refined grids, only the first stage is simulated for 15 seconds of flow time and the last ten seconds are used for time averaging. Unless mentioned, the results presented are for the uniform grid size. Simulation without particle charge are the conventional two-fluid models and act as base case for comparison.

The fluidized-bed is initialized with three particle phases distributed uniformly. Fixed gas velocity is specified at the inlet. At the outlet, a pressure boundary condition is specified. For

Table 3.8 Particle volume fraction and charge used in the CFD simulations

	FINES	**DROPPED**	**WALL**
Volume fraction			
Bubbling	0.00039	0.6158	0.0137
Slug	0.00280	0.6074	0.0097
Charge (C/m^3)			
Bubbling	0.0175	-0.0005636	-0.0461
Slug	0.0281	-0.0005952	-0.0361

Table 3.9 Simulation conditions and parameters

Description	**Value**
Gas velocity, bubbling bed, m/s	0.1965
Gas velocity, slug flow, m/s	0.524
Gas density, kg/m^3	4.93
Gas viscosity, kg/ms	1.8e-05
Particle density, kg/m^3	843.0
Restitution coefficient, e	0.8
Discretization scheme (spatial, temporal)	Second order
Time step, s	0.0001

the gas phase, a no slip wall boundary condition is used. A no slip wall boundary condition is used for the particle phase. The wall is assumed to be grounded and zero electric potential is used. The influence of the particle phase and potential boundary conditions will be described in detail in the results section.

3.5 Simulation Results

In this section, bubbling bed and slug flow simulation results and comparison with experiments will be discussed. The instantaneous contours of gas volume fraction for the bubbling bed and slug flow are shown in Figure 3.9 and Figure 3.10. It is important to note that the same fluidized-bed (diameter: 0.0859 m, height: 1.27 m) column is used for both flow regimes, though the simulation contour plots show different column width. Second order discretization schemes are necessary to resolve the bubble shape, as bubbles resolved by first order methods result in unphysical and pointed structures due to numerical diffusion. Large gas bubbles close to bed width characteristic of slug flow regime are shown in Figure 3.10

The measured bed-height from experiments is 0.478 m and 0.958 m in the bubbling-bed and

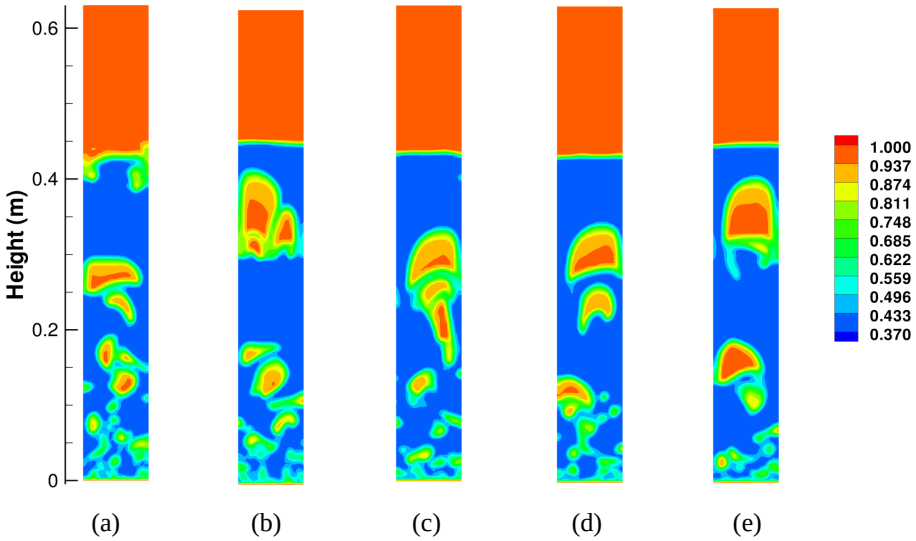

Figure 3.9 Instantaneous contours of gas volume fraction in bubbling-bed at different flow times. (a) 2.30 s (b) 2.70 s (c)3.30 s (d) 5.50 s (e) 5.70 s.

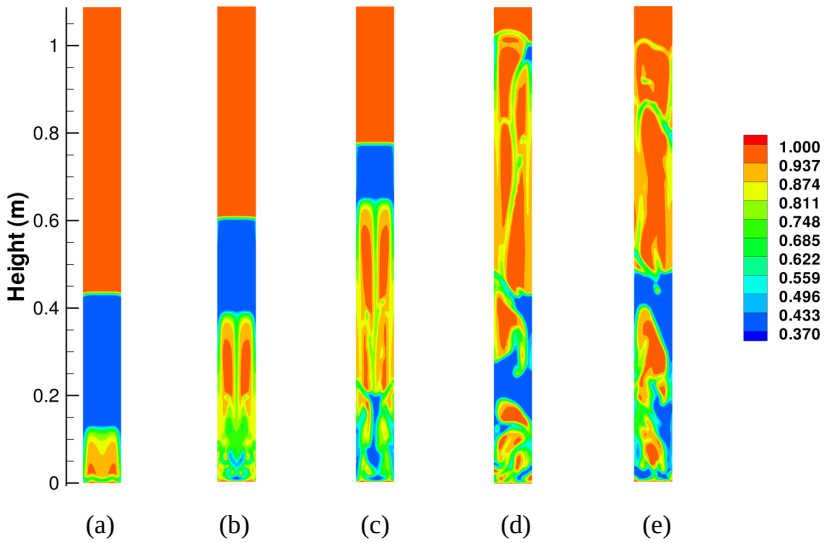

Figure 3.10 Instantaneous contours of gas volume fraction in slug flow at different flow times. (a) 0.22 s (b) 0.62 s (c) 1.02 s (d) 1.62 s (e) 1.82 s.

slug flow regime. The gas velocity is higher in the slug flow regime ($4.0\mathbf{U}_{mf}$) compared to the bubbling-bed ($1.5\mathbf{U}_{mf}$) and so bed expansion is higher. The multi-fluid simulations predicted time average bed height of 0.46 m and 0.7 m. The bubbling bed height simulation results compared reasonably well with the experimental measurements, but there is a difference in the slug flow bed height. The column is made of carbon steel and so it is not possible to make visual observations of the expanded bed height and therefore difficult to measure. Measurements are made by looking down from the top of the column. The bed in the bubbling regime is more stable and easier to record than compared to slugging where the bubbles burst. The slug flow simulations predicted the bubble burst and instantaneous bed height of 1.0 m is observed at some flow times.

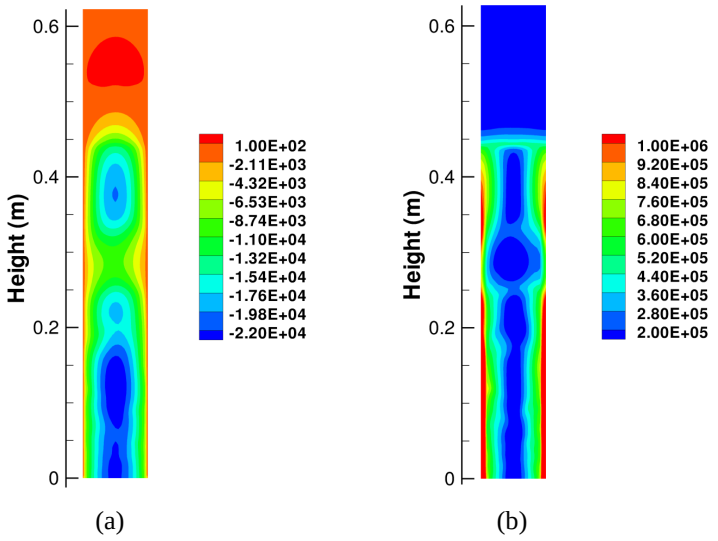

Figure 3.11 Instantaneous contours of (a) electric potential (Volts)(b) radial component of electric field (Volts/m) in the bubbling fluidized-bed.

The presence of charge on particles, creates an electric field that causes the particles to segregate depending upon the particle charge, polarity and local electric potential. From experimental measurements (Table 3.6), the overall bed charge is negative and this is due to high volume fraction of negatively charged WALL and DROPPED particles. Figure 3.11 shows the contours of instantaneous electric potential and electric field from bubbling-bed simulations. The electric potential is negative below and positive above the bed height. Such opposite polarity is observed [55, 56, 57] in the case of bipolar charging. Due to the drag force, the fine

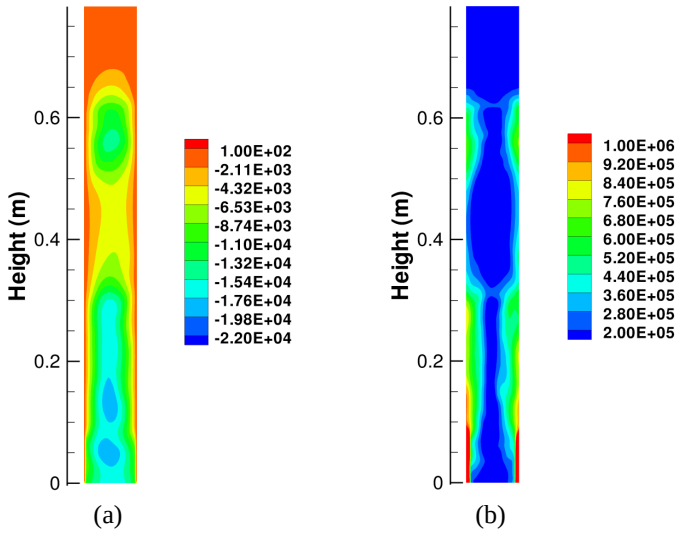

Figure 3.12 Instantaneous contours of (a) electric potential (Volts) (b) radial component of electric field (Volts/m) in the slug flow fluidized-bed.

particles segregate towards the upper section of the fluidized bed and positive electric potential is observed, while the bigger bed particles move towards the lower section and hence negative potential below the bed height. The contours of the electric field represent the absolute value of the gradient of the potential in the radial direction. The contours show high electric potential gradients near the wall close to the distributor, which causes the highly negatively charged particles to segregate. Figure 3.12 shows the contour of instantaneous electric potential and electric field for the slug flow simulations. The region where the potential changes sign is different in the bubbling-bed and slug flow, due to the difference in the bed-height. In the bubbling-bed, high electric potential gradients are observed up to bed-height of ~ 0.15 m and ~ 0.08 m in the slug flow.

The segregation of particles due to electrostatic forces is explained using Figure 3.13. Assume a situation where the electric potential is positive at location x_1 inside the bed and zero at the wall, x_0 . The electrostatic force in the radial direction is defined by $F_{qx} = -q\varepsilon_{\mathrm{p}} \left(\nabla\varphi\right)_x$. The potential gradient at the two locations (x_0, x_1) is approximated as $(\varphi_1 - \varphi_0)/(x_1 - x_0)$ and this is positive in this given condition. Assuming, the electrostatic force is most significant of all forces, it would be important to know the motion of a charged particle at the location x_1. The potential gradient is positive, the direction of the electrostatic force is now dependent

upon the polarity of the charged particle. If a positively charged particle is at location x_1, the electrostatic force acts on the particle and segregate towards the wall. This can also be explained as a positively charged particle in a positive potential region would cause repulsion and the particle will segregate. According to the analysis, as the potential in region below the bed height is negative and zero wall boundary condition, a negatively charged particle in this region would segregate towards the wall. For the same reason, a positively charged particle above the bed height would segregate towards the wall.

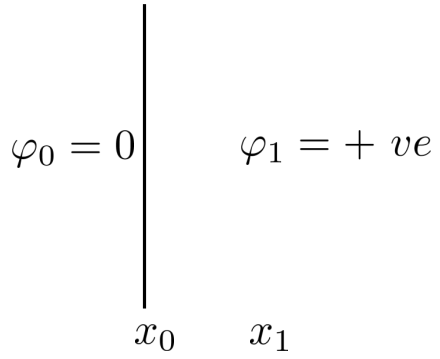

Figure 3.13 Illustration to explain particle segregation due to electrostatic forces.

3.5.1 Particle Segregation

In the CFD simulations, a zero wall boundary condition for the electric potential is used. The walls are grounded only between experiments and hence a zero potential boundary condition is incorrect. A dynamic boundary condition needs to be used, which is a function of local collisions between the polyethylene particles and the column wall made of carbon steel. The work function of carbon steel ~ 4.5 eV and polyethylene is ~ 5.3 eV, so the collisions will cause the polyethylene particles to be negatively charged and the column wall to be positively charged. Carbon steel is at the center of the triboelectric series [58], which shows that there is less tendency to gain or lose electrons and zero potential boundary condition is a reasonable assumption. It is important to note that using zero potential boundary condition would reduce the electrostatic forces (the gradient of the potential is less with zero boundary condition compared to a positive potential), but does not change the segregation pattern of the WALL and DROPPED particles.

The solid phase distribution in the bubbling-bed case will be discussed next. The volume fraction and particle size of fine particles is small compared to the wall and dropped particles. All the fine particles entrained out of the fluidized-bed due to gas-particle drag force in the first fifty seconds of flow time, and the results are independent of the presence or absence of charge. Figure 3.14 shows the mean volume fraction of wall particles without and with charge. When charged, the wall particles segregate (Fig. 3.14 b) towards the column wall close to the distributor plate. A uniform distribution (Figure 3.14 a) of wall particles is observed when there is zero charge on the particle phase. The observations in the experiments compare well with charged case. From the contour plot the height of the wall coating is 150 mm and the experimental measured value was 300 mm. The simulations need to be run with high grid resolution to compare the measured thickness of wall coating (0.5 - 0.75 mm). The grid size used in the simulations is 4 mm and so the thickness of wall coating is not captured by the uniform grids. To capture the wall thickness, a non uniform refined grid with 2.5 mm grid size at the center and 1 mm grid size near the wall is used. This grid is also not sufficient to resolve the bubbling-bed case near the wall but adequate for the slug flow case.

Figure 3.15 shows the mean volume fractions of WALL particles with refined non uniform grids. In the bubbling-bed case, the thickness of the wall particles extends from 3 - 4 cells (3 - 4 mm) with high particle volume fraction in the first cell. Figure 3.16 shows the mean volume fraction of DROPPED particles without and with charge. The particle volume fraction is high near the walls for the charged case compared to uncharged case. In the slug-flow simulations, 90 percent of the fine particles entrained in the first fifty seconds of flow time. Though the gas-velocity is high in slug flow condition, the FINE particle size is bigger than in bubbling-bed case and some fine particles are left inside the bed. Figure 3.17 shows the mean volume fraction of WALL particles in the slug-flow simulations. The height of the wall coating in slug flow simulations is 80 mm compared to 100 mm in experiments. In the refined case (Figure 3.18) in the slug-flow case the WALL particle thickness is 5 - 6 cells (5 - 6 mm) with high volume fraction in the first two cells. Figure 3.19 shows the solid phase distribution of DROPPED particles in the slug flow simulation. Higher particle volume fractions are observed for the charged case similar to the bubbling bed.

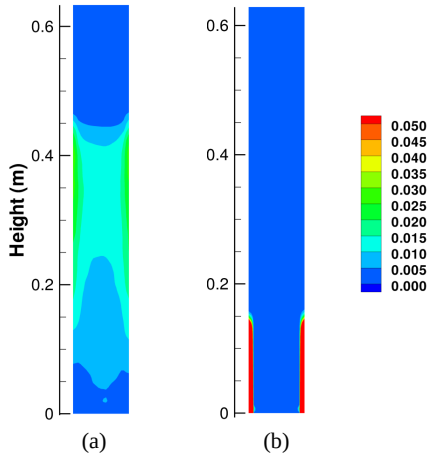

Figure 3.14 Mean volume fraction of WALL particles in bubbling-bed simulations. (a) zero charge (b) charged.

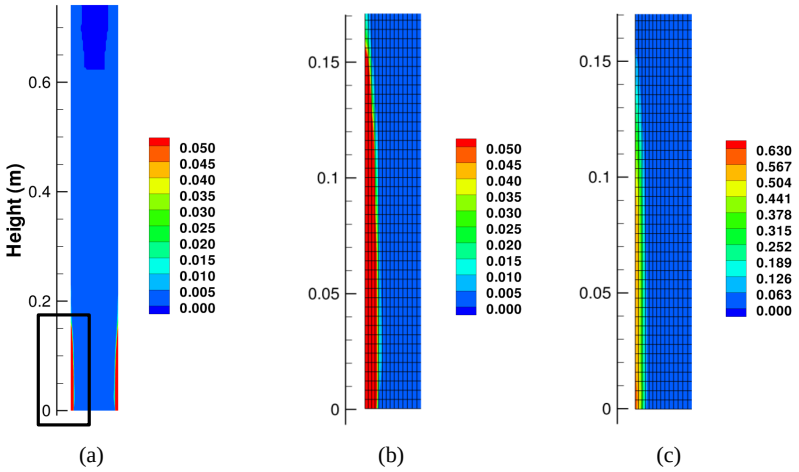

Figure 3.15 Mean volume fraction of WALL particles in bubbling-bed simulations with refined grid. (a) charged (b) left wall near the distributor (c) left wall near the distributor with different range.

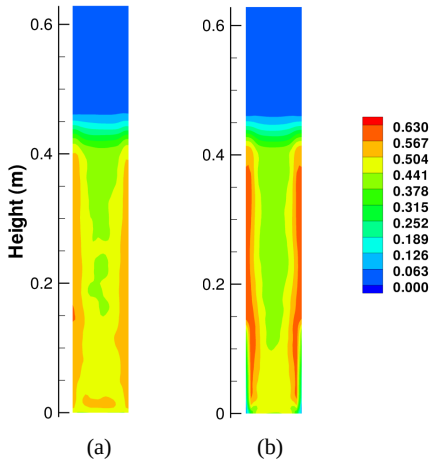

Figure 3.16 Mean volume fraction of DROPPED particles in bubbling-bed simulations. (a) zero charge (b) charged.

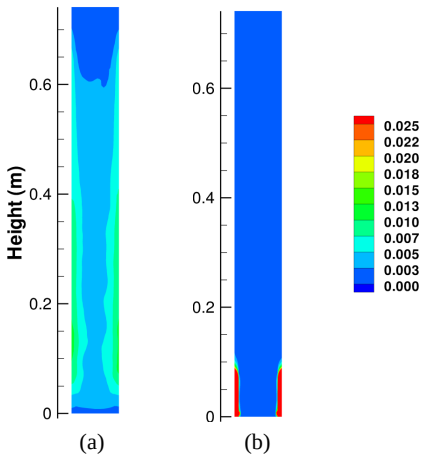

Figure 3.17 Mean volume fraction of WALL particles in slug flow simulations. (a) zero charge (b) charged.

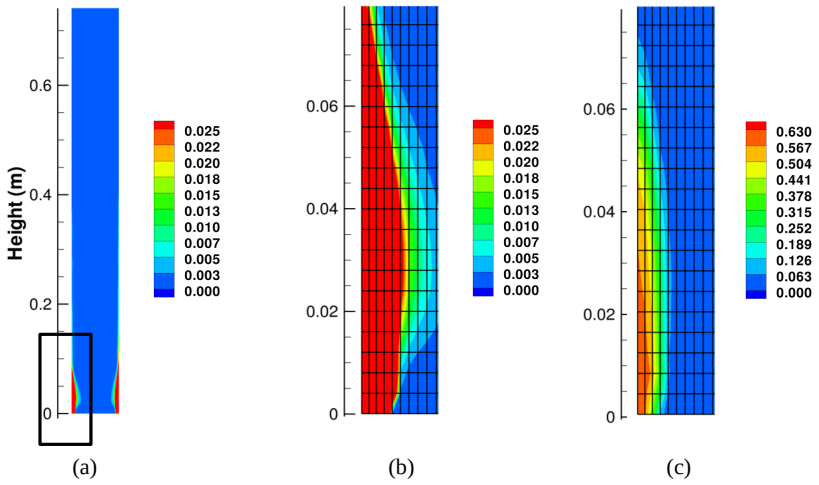

Figure 3.18 Mean volume fraction of WALL particles in slug flow simulations with refined grid. (a) charged (b) left wall near the distributor (c) left wall near the distributor with different range.

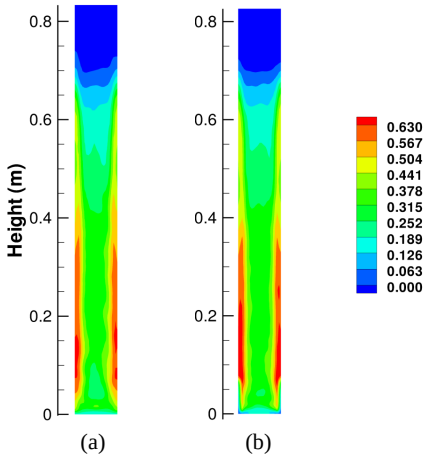

Figure 3.19 Mean volume fraction of DROPPED particles in slug flow simulations. (a) zero charge (b) charged.

3.5.2 Particle Discharge

In the experiments, after the bed is fluidized for a period of time, the gas is shut off and particles are allowed to settle. After the bed is settled, the distributor plate is removed and particles are allowed to drop down in the bottom Faraday cup. After all the bed particles dropped down, there are particles sticking to the column wall, known as WALL particles. The objective of the particle discharge simulations is to simulate the qualitative observations in the experiments. In the simulations at flow time equal to 80 seconds, the gas inlet velocity is initialized to zero and the particles are allowed to settle to close packing. The inlet boundary condition is changed to pressure outlet and the particles are allowed to fall down. The simulations results for the bubbling-bed case will be discussed here. Simulation with and without particle charge are run for twenty seconds of flow time. All the particles dropped down when there is no charge in the first 3-4 seconds. For the charged particle case, the DROPPED particles dropped down, but the WALL particles are still present at the wall. Only ten percent of the wall particles dropped down during the twenty seconds of flow time after the boundary conditions are changed. The electrostatic forces on the WALL particles are high enough to prevent the particles to drop down, but the boundary condition does not allow the particles stick permanently. It is expected that the wall particles would eventually fall down, if the simulations are run for a long time.

3.5.3 Model Sensitivity Study

All the fluidized-bed experiments are repeated two to three times and an error bar is associated with the measurements. The mean particle size in each group is reasonably close in all the experiments, but the charge measurements have an error bar with variation of more than ten percent [2]. To study the sensitivity of the electrostatic model two cases are simulated. In the first case (case 1), the magnitude of the charge of each particle phase is increased by ten percent and in the second case (case 2), decreased by ten percent. The size of each particle phase and other simulation conditions are the same as the original case. The contours of mean volume fraction of WALL particles for bubbling bed is shown in Figure 3.20 and slug flow in

Figure 3.21. The segregation of the particle phase in both cases is similar to the original case and the height of the WALL particles did not change appreciably. The mean charge in the bed is increased or decreased by ten percent, when the charge on each particle phase is varied by ten percent. As the mean charge is still negative, the highly negative charged WALL particles segregated towards the column wall and the less negatively charged DROPPED particles moved to the center of the bed.

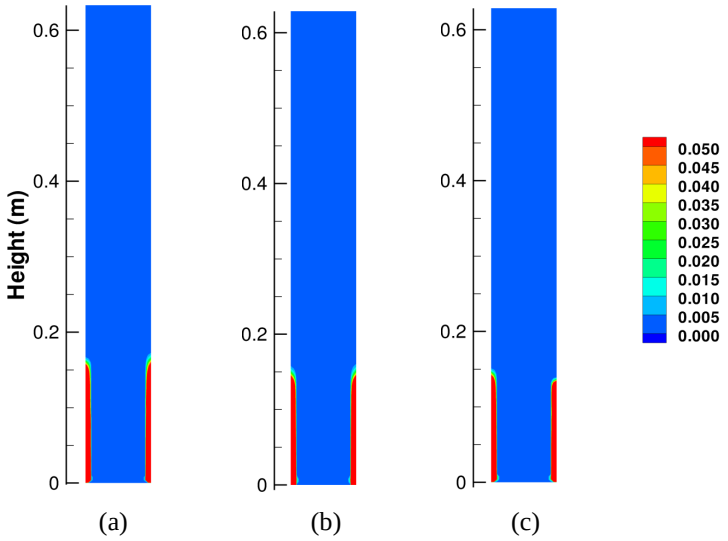

Figure 3.20 Mean volume fraction of WALL particles in bubbling bed: (a) case 1 (b) original case (c) case 2.

3.6 Conclusions

The predictions of the electrostatic model [59] are compared with experimental observations. The model predicted the hydrodynamic and electrostatic segregation observed in the experiments. The height of the wall coatings in both flow regimes are predicted fairly accurately. The model was able to predict mean properties such as bed height and solid phase distribution inside the bed, even though a mechanistic model for the adhesion of particles to the column wall and charge generation or dissipation is not accounted for. The prediction of the wall particles is important for the smooth operation of the process. In a reactive environment such as polymerization and catalytic processes, poor mixing near the walls would cause the wall particles to melt and could result in sheets. The sheets can be formed in different regions of

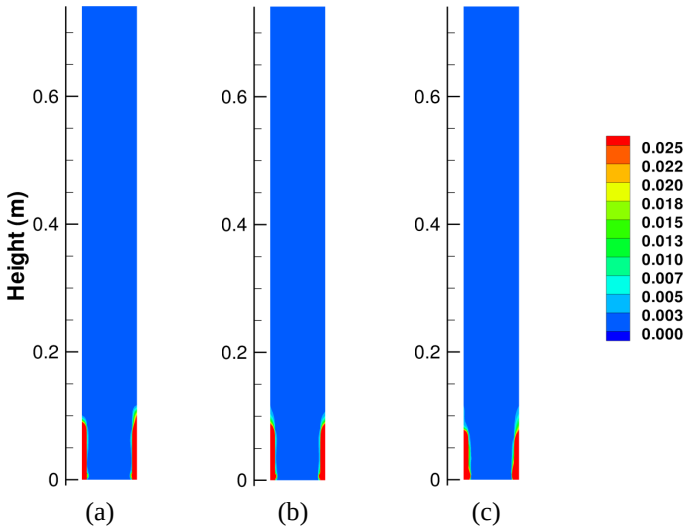

Figure 3.21 Mean volume fraction of WALL particles in slug flow: (a) case 1 (b) original case (c) case 2.

the fluidized-bed depending upon the local potential, particle charge, particle polarity (bipolar charge effects) and can result in process upsets. CFD simulations can be used to predict regions of sheet formation and help reduce such process upsets. For future numerical studies, it would be of interest to develop a model for charge generation and dissipation in order to predict the evolution of the particle charge.

4 PILOT SCALE REACTOR SIMULATIONS

4.1 Introduction

The objective of this work is to apply the developed electrostatic model on the pilot-plant reactor and to understand the effects of charged particles on the hydrodynamics of the fluidized-bed reactor. Gas-solid fluidized-beds can be modeled using two approaches, namely Euler-Lagrange and Euler-Euler. The Euler-Lagrange models ([35], [3], [34]) consider the gas phase as a continuum and Newton's equations are solved for each solid phase at the particle level. The trajectory and motion of each particle is calculated at each time step, and this increases computational resources so that there is a limitation of the number of particles used in large-scale simulations. At present these models are restricted to dilute gas-solid flows or laboratory-scale experiments. The Euler-Euler models ([60], [61], [7]) treat the gas and solid phases as interpenetrating continua. The solid pressure and viscosity are obtained using the kinetic theory of granular flow and frictional theory. These models can be used to simulate large-scale reactors like pilot-plant or commercial reactors.

In this work an Euler-Euler model is used to model a pilot-plant-scale polymerization fluidized-bed reactor. There are only a few works in the literature that deal with modeling of large-scale pilot-plant or commercial reactors. Gobin et al. [32] used the Euler-Euler approach to simulate a commercial-scale fluidized-bed reactor. They did two- and three-dimensional simulations to obtain the mean flow properties, such as volume fraction, bed height, and pressure drop, and their results matched well with the experimental data. Fan et al. [62] used the Euler-Euler approach to predict hot spots in a pilot-plant fluidized-bed reactor. In their work they developed a chemical reaction engineering model and the quadrature method of moments (QMOM) was used to predict the final polymer particle size distribution and temperature.

Only a limited number of publications deal with modeling of electrostatics in gas-solid fluidized beds. Mahdi et al. [9] analyzed gas-particle flow in a vertical riser. They neglected

hydrodynamic segregation and studied segregation due to the presence of charge on particles. They assumed a prescribed charge on all particles and observed radial segregation in the riser. Shih et al. [46] used a two-fluid model to study the shapes and sizes of bubbles with and without an electric field and assumed a fixed charge on particles. They did simulations on a two-dimensional bed with a central jet and simulated a flow time of one second. The above two works on electrostatics were for monodisperse cases. In this work we develop an electrostatic model for a polydisperse case and couple it with a multi-fluid CFD code. The electric field is computed at every grid point and time step. Using the quadrature method of moments three solid phases are used to represent the polymer particle size distribution. The volume fractions of each solid phase are obtained from the weights and abscissas found using QMOM [62]. The charge on each solid phase is assumed to be a function of the particle size and is used as an input to the electrostatic model. In its present form, the CFD model does not account for charge generation or dissipation. The approach is verified with a simple test case and validated with published literature as shown in previous chapter and then applied on the pilot-plant-scale olefin polymerization fluidized-bed reactor.

This work is organized as follows. The second section deals with the coupling of polymerization kinetics and computational fluid dynamics. The third section describes the application of the electrostatic model to a pilot-plant polymerization fluidized-bed reactor. Three cases are considered here. The first is the effect of the magnitude of charge on the distribution of solid phases, the second is the continuous injection of catalyst in the fluidized bed, and the third is the effect of electrostatics on entrainment of fines. The effect of grids used on the computation of electrostatics is presented in fourth section. A test case is taken to show that a uniform grid is required to predict accurate segregation of particles. Three-dimensional simulations are performed for the case of the effect of magnitude of charge on the distribution of solid phases are also presented. The final section reports the conclusions.

4.2 Polymerization Reaction Kinetics and Fluidized-Bed Dynamics

The solid phase residence time for polyethylene polymerization is on order of hours and the time scale of fluid dynamics is on the order of seconds. It is computationally expensive to run

a CFD simulation for hours. In this work the CFD model is decoupled with the polymerization reaction part. Given a catalyst size distribution and using the reaction engineering model developed by Fan [6] the steady state polymer size distribution can be obtained. The CFD simulation is initialized with steady state polymer size and during the simulation the assumption is that the change in particle size and temperature is small.

4.2.1 Pilot-Plant Process

After the verification and validation of the electrostatic model in the previous chapter, the CFD model is applied to a pilot-plant fluidized-bed reactor. A sketch of a typical pilot-plant polymerization fluidized-bed reactor is shown in Figure 4.1. The reactor consists of three zones, namely a fluidized-bed zone, a disengagement zone, and a dome section. The disengagement zone has a larger diameter (2-4 D) than the fluidized zone (D) so as to reduce the gas velocity to minimize the entrainment and elutriation of catalyst and polymer particles. The initial bed height is 4-6 D. The value of D is in the range of 0.4-0.6 m. The fluidizing medium comprises of a gas mixture of monomer (ethylene), comonomer, hydrogen and inert gases. The gas is operated at a velocity of 7-9 times the minimum fluidization velocity of the polymer particles. As the gas passes through the bed of particles it diffuses through a growing porous polymer and reaches the active sites of the catalyst where the reaction takes place. The polymer particles grow in size (500-3000 micro-meters) until the catalyst is deactivated. Due to segregation based on size, the smaller particles move towards the disengagement zone and, if the gas velocity is high enough, then the particles will entrain out of the reactor. The larger polymer particles gain weight during the polymerization reaction and move towards the bottom, and are removed periodically near the distributor plate. In the CFD simulations the size of the polymer particles does not change and they will not be removed from the fluidized-bed reactor.

4.2.2 Multi-scale Features of Polymerization Fluidized-Bed Reactors

Figure 4.2 shows the different phenomena and length scales associated with olefin polymerization in fluidized-bed reactors. The length scales are divided into three scales of interest: microscale (1-100 A), mesoscale (10-3000 microns) and macroscale (1-10 m). On the microscale,

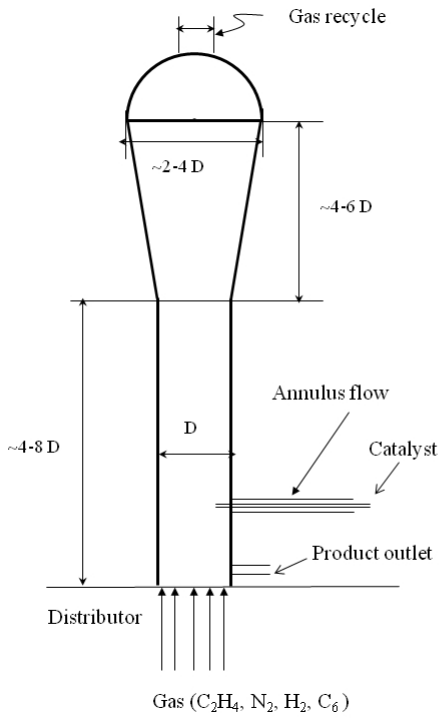

Figure 4.1 Sketch of a Unipol pilot scale gas-phase polymerization fluidized-bed reactor.

the active sites are where the reaction takes place. The important steps at this scale are: initiation of active sites, chain propagation, chain transfer and deactivation of active sites. The polymerization mechanism has to be modeled correctly as it affects the mesoscale processes. The molecular weight distribution and particle composition depends on the polymerization chemistry. During the early stage of polymerization, particle fragmentation takes place due to hydraulic forces. The mesoscale accounts for features at the particle length scale. At this scale the heat and mass transfer to and from the particle are important. There are several models that deal with processes at the single particle level. Also, as described earlier, there are effects of thermal and electrostatic phenomena at the mesoscale. At the macroscale, there are additional features like segregation, mixing of polymer particles due to bubbles and elutriation/entrainment that must be modeled.

Phenomena over a wide range of length scale are involved in fluidized-bed polymerization reactors. The reactor diameter is on the order of meters, the particle diameter varies from 10-3000 microns, sub-fragments are on the order of 1-10 nanometers and catalyst active sites are of the order of angstroms. In order for reaction to occur, the monomer must diffuse

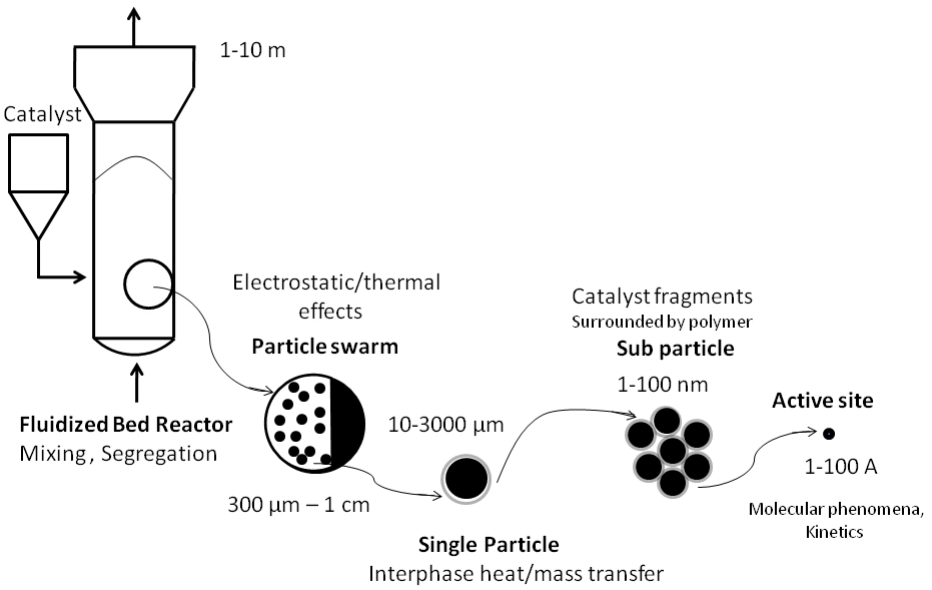

Figure 4.2 Multi-scale phenomena associated with olefin polymerization fluidized-bed reactor.

across the boundary layer surrounding the particle, through the macropores in the particle, and to an active site of the catalyst where the polymerization reaction takes place. Because the catalyst is injected continuously, the residence time of each particle is different. Hence, the particles will have different sizes resulting in a particle size distribution (PSD). Under unfavorable operating conditions, particles can agglomerate or break into fragments depending on the local temperature and produce a wide distribution of particle sizes. A wide distribution of particle sizes can cause phenomena such as segregation and elutriation. Large particles produced by polymerization and agglomeration move towards the bottom of the reactor where they are removed. This phenomenon can result in particle segregation. At high gas velocities smaller particles are elutriated through the top of the reactor. Heat and mass transfer to and from the particle controls the local particle temperature and phenomena like agglomeration and breakage. The reaction kinetics depends upon the heat and mass transfer to the active sites. All of the above stated phenomena are highly coupled and have a strong influence on the hydrodynamics of the fluidized bed. At present, it is difficult to have a single model that can explain all of the multiscale phenomena of fluidized-bed polymerization reactors. Because the

time scale of the polymerization reaction is of the order of hours and the fluid dynamic time scales are on the order of seconds, it is too expensive to run a three-dimensional CFD simulation that captures the entire range of time scales using the current computational resources and codes. Thus, in the present work, the reaction processes occurring on long time scales are decoupled from the fluid mechanics as described below.

A wide range of phenomena with disparate length and time scales are involved in the production of polyethylene using fluidized-bed reactors. A simple mechanistic scheme [62] is used to describe the microscale polymerization kinetics. The fundamental reactions considered are the initiation, propagation and termination of the active sites. A uniformly distributed lumped thermal model is used to represent the mesoscale phenomena and a chemical reaction engineering model solves the mass, energy and species balances for an individual growing particle. The catalyst size distribution is represented by a few nodes using the QMOM, and the CRE (chemical reaction engineering) model [62] is applied on the nodes and the final polymer size distribution is obtained. The CFD model is now initialized with the polymer PSD (particle size distribution). The results from the CRE and multi-fluid models can be used to describe the macroscale phenomena such as segregation, entrainment in the reactor. This macroscale information is useful in design and scale-up of fluidized-bed polymerization reactors.

4.2.3 Industrial Scale Reactors

The reactor modeled in this work is a pilot-plant-scale, so it is important to look at experimental evidence of fouling in pilot-plant/commercial-scale fluidized beds. There is abundant patent literature with evidence of agglomerate formation in commercial-scale olefin polymerization fluidized-bed reactors. These experimental results are different from the academic lab-scale fluidized-bed results discussed in previous chanpter since one needs to consider the nature of the highly exothermic polymerization reaction and where it is taking place. Ali and Hagerty [63] used a two-stage reactor system to produce bimodal ethylene polymer compositions. They claimed to prevent pressure tap fouling in the first fluidized bed and avoid fouling in a downstream gas fluidized by adding 0.1-0.6 ppmv of water. Goode et al. [64] also used water around 3 ppmv to reduce the electrostatic effects. Addition of water aids to increase the charge dissi-

pation rate by increasing the electrical conductivity. Ali et al. [65] used tetraethylorthosilicate (TEOS), 16-40 ppm for reducing negative static and water for positive static in the bed. Brant et al. [66] used a catalyst that contains a static modifier, which is effective in inducing the static charges and does not substantially interfere with catalyst activity. Brown and O'Shaughnessy [67] used a mixture of aluminum or chromium salts of an alkylsalicylic acid and alkali metal alkyl sulfosuccinate, Chirillo et al. [68] used vanadium- or titanium-based compounds as catalysts together with alkyl aluminum co-catalysts, Poliafico et al. [69] used hydroxyethyl alkylamine or its derivatives, Wilcox [70] used alkyl sulfosuccinate agents, Eisinger et al. [71] and Fulks et al. [72] used titanium-based catalysts to reduce or eliminate electrostatic effects, and recently Neal-Hawkins et al. [73] and McKay et al. [74] used antistatic agents on supported catalysts to reduce static or fouling problems. Bartilucci et al. [75] took a polymer sample exiting the reactor and measured the charge using Faraday drums and then, based on the range of accepted values and polarity of the sample, a negatively- or a positively- charged chemical is added. Muhle and Hagerty [76] monitored acoustic emissions and determined events, such as the onset of reactor stickiness, sheeting. Markel and Agapiou [77] measured entrainment static and then added control agents to alter the bed charges. Llinas and Selo [78] used temperature probes to find out fluctuations in temperature, which are indicative of onset of sheeting. Haardt et al. [79] fitted detection devices to the fluidization grids and used the signals whenever agglomerates or sheets hit the devices. Muhle et al. [80] coated the reactor using a titanium based compound of 100 micron thickness to reduce buildup of static on reactor walls. Mihan et al. [81] used an antistatic layer of 0.1-800 microns thickness to coat the inner walls of the reactor. The coating is a mixture of a poly alpha olefin and a nonvolatile antistatic agent. Cohen et al. [82] used a coating composition containing a straight chain or branched polyaromatic amine dissolved in an aqueous solution and thereafter the coated surface was flushed or rinsed with water without drying the same. Gupte et al. [83] fed the catalyst into the reactor in a stream of gas containing at least 75 percent noble gas to reduce static. Painter et al. [84] generated a gas tangential flow at the dome section of the reactor to reduce entrainment and drooling.

4.3 CFD Simulations of Pilot Plant Scale Reactor

The multi-fluid CFD model described in the chapter 2 is used to describe segregation of polymer particles due to hydrodynamic and electrostatic effects in gas-solid polymerization fluidized beds. Grid generation for the pilot-plant reactor geometry is done using the Gambit 2.3 software. A Cartesian coordinate system is used for grid generation and quadrilateral cells are formed for the two-dimensional case. Time-dependent simulations are performed for the pilot-plant reactor. One hundred seconds of flow time is simulated and the results are obtained by averaging the last ninety seconds of flow time and data is sampled after every time step. The simulation and wall boundary conditions are shown in Table 4.1. No-slip for the gas phase and free-slip boundary conditions for the solid phase are employed. A convergence criterion of scaled residuals of 10^{-4} is used. A second-order upwind scheme for spatial derivatives, and a second-order accurate time stepping method for temporal derivatives are used. Although the pilot-plant reactor is three dimensional, two-dimensional simulations are done as three-dimensional simulations are computationally expensive. However, the fully-coupled CFD model can be easily extended to three dimensions as shown below in the section on three-dimensional simulations. The volume fractions of the polymer particles are obtained from the chemical reaction engineering model [62]. Table 4.2 shows the properties of solid and gas phases used in the pilot-plant simulations. Three cases are considered here. In the first case the effect of charge on the spatial distribution of polymer particles is studied. The charge on each solid phase is increased keeping the mean charge constant. It is shown in the literature ([85], [18]) that catalyst/fine particles carry more charge per unit mass than large particles. In such cases the electrostatic effects will be strong. The second case is performed to study the distribution of a catalyst phase continuously injected into a bed of polymer particles of mean negative charge. The third case investigates the effect of electrostatics on the entrainment of fine particles out of the reactor.

Description	Value
Pressure based solver	2ddp
Unsteady formulation	2^{nd} order implicit
Momentum discretization	2^{nd} order methods
Time step, seconds	0.0001-0.0005
Data sampling for time statistics	1
Particle-particle restitution coefficient	0.8
Boundary conditions	
inlet	velocity inlet
outlet	pressure outlet
wall	
gas phase	zero slip
solid phase	free slip
electric potential	zero

Table 4.1 Simulation parameters for pilot-plant reactor

Solids	Small	Medium	Large
density, kg/m^3	843.0	843.0	843.0
diameter, micro-meter	523.0	1176.0	1751.0
volume fraction	0.00453	0.1943	0.310
charge, coulomb/m^3	0.1081	-0.001	-0.00115
Gas Mixture			
density, kg/m^3	22.1		
viscosity, kg/(m-s)	1.427e-05		

Table 4.2 Properties of phases used in pilot-scale simulations

4.3.1 Effect of Charge on the Spatial Distribution of Polymer Particles

The objective of this simulation is to study the effect of charge on the spatial distribution of polymer particles. The idea is to observe whether more segregation is observed when the charge on the each solid phase is increased, keeping the mean bed charge constant. The mean bed charge is known to be negative from experimental results. The small polymer particles are positively charged, and the medium and large polymer particles are negatively charged. Since the charge as a function of particle size is unknown the charge on each solid phase is varied and its effect is observed. The mean bed charge is kept constant but the standard deviation is varied from 0.001 to 0.01 coulombs/m^3 to evaluate the effect of the dispersion of the overall charge distribution about the mean. Even this small variation of standard deviation caused a change in the solid phase spatial distribution. The charges on the solid phase are approximated to the realistic charges present in polymerization fluidized-bed reactors. The three solid phases are uniformly distributed in the beginning of the simulation. Three cases are run with the above-stated simulation conditions. In the first case the charges on the solid phases are initialized to zero. The second and third cases were run with low and high charges, respectively. The first case acts as a base case and is used to compare the results with the other cases. Table 4.3 shows the mean charge and charge on each solid phase for the three cases. The variation of mean static pressure along the bed height is shown in Figure 4.3 for the three cases. The mean static pressure variation is nearly the same for the three cases as the pressure drop is mainly due to the bed weight. Electrostatic effects have the minimal effect on the overall pressure drop. Figure 4.4 shows the instantaneous contours of volume fraction of gas at different flow times. At t=3sec large slugs are seen which compares well with the experimental observations.

	Mean Charge	Standard Deviation
Zero charge	0.0	0.0
Low charge	-1.264e-04	0.0011
High charge	-12.264e-04	0.01

Table 4.3 Charges on polymer particles used in pilot-plant simulations

The instantaneous contours of electric potential are shown in Figure 4.5. For clarity, the contour plot is divided into positive and negative ranges. The reason for high potential values

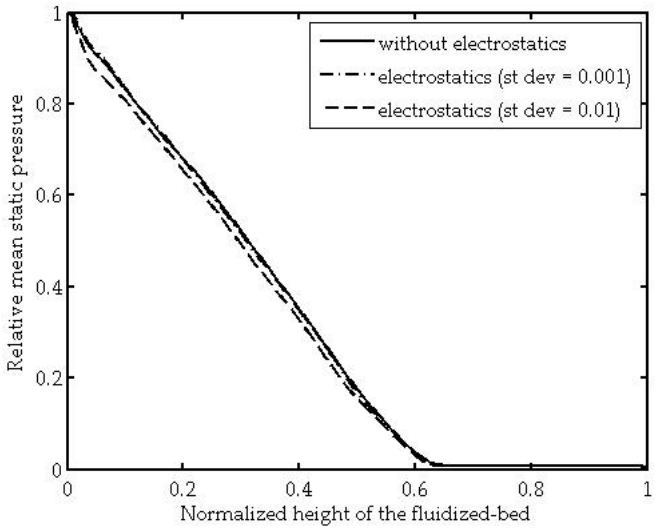

Figure 4.3 Variation of mean static pressure along height of the fluidized bed.

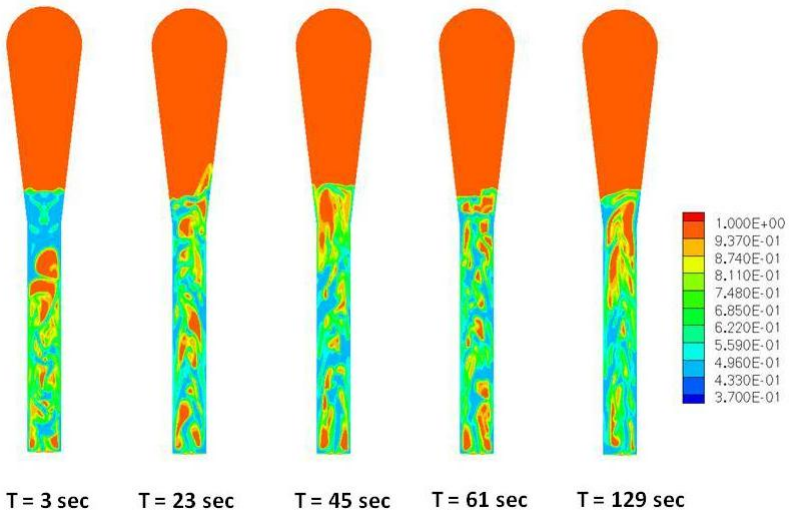

Figure 4.4 Instantaneous contours of gas volume fraction of two-dimensional simulation at different flow times.

is described in the section on three dimensional simulations. Due to hydrodynamic segregation, a higher volume fraction of the small positively charged polymer particles is observed in the expansion section. For this reason a positive potential is seen at the top of the reactor. Similarly higher volume fractions of the negatively charged medium and large polymer particles are observed in the fluidized-bed zone. For this reason the electric potential is negative towards the bottom and near the distributor plate. This is due to bipolar charging in polymerization fluidized-bed reactors, which is well supported by the literature ([17], [18], [85]). In actual reactor operation there is abundant evidence that shows that most electrostatic effects are found near the distributor plate and near the expansion and dome sections of the reactor. The maximum absolute negative potential is observed at the centerline, above the distributor plate [85] and the maximum positive potential is observed just above the bed height. The zero potential is found below the bed height where we have both the positive and negative charged polymer particles, which makes the source term in the Poisson equation zero. The instantaneous electric potential and total solids volume fraction at the centerline of the reactor along the bed height is shown in Figure 4.6. A Z-shaped profile is seen, similar to the profile reported in experiments of Fang et al. [85].

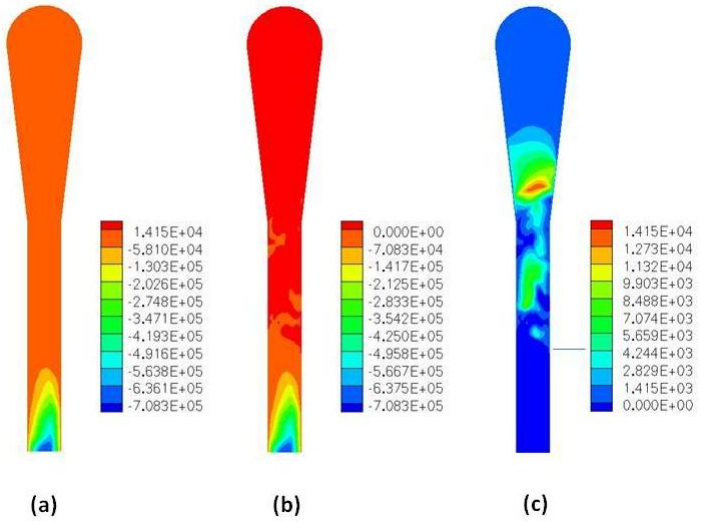

Figure 4.5 Instantaneous contours of electric potential of pilot-plant fluidized-bed reactor for standard deviation = 0.01 at t=129.5 sec: (a) total range, (b) negative range, (c) positive range.

It is also important to find out where the gradient of the electric potential is highest as such

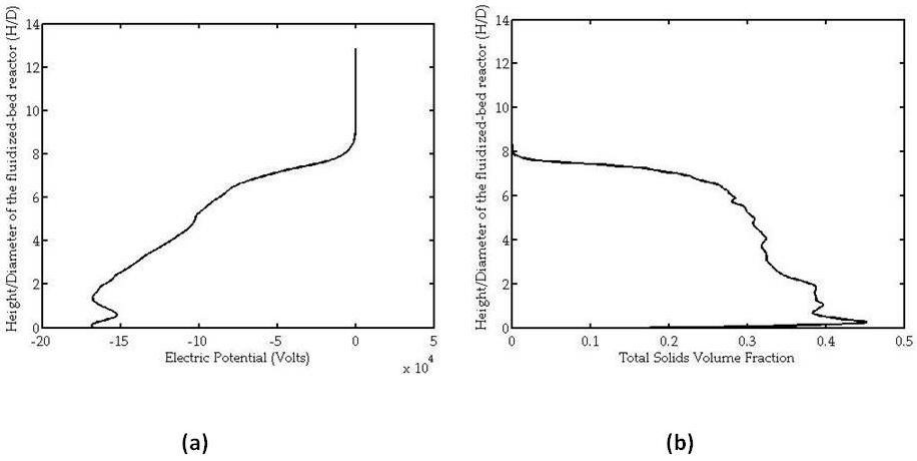

Figure 4.6 Instantaneous plot of (a) electric potential and (b) total solids volume fraction at the center and along the bed height at t= 100 sec.

locations are more prone to electrostatic forces. The electric field, which is the gradient of the electric potential in the radial and axial directions, is shown in Figure 4.7. The electric field is highest near the wall close to the distributor plate. The gradient in electric potential is higher in the radial direction compared to the axial direction. Hence, the electrostatic forces push the particles towards the walls of the reactor. The electric field in the axial direction (shown with a reduced scale) has the strongest effect near the distributor plate.

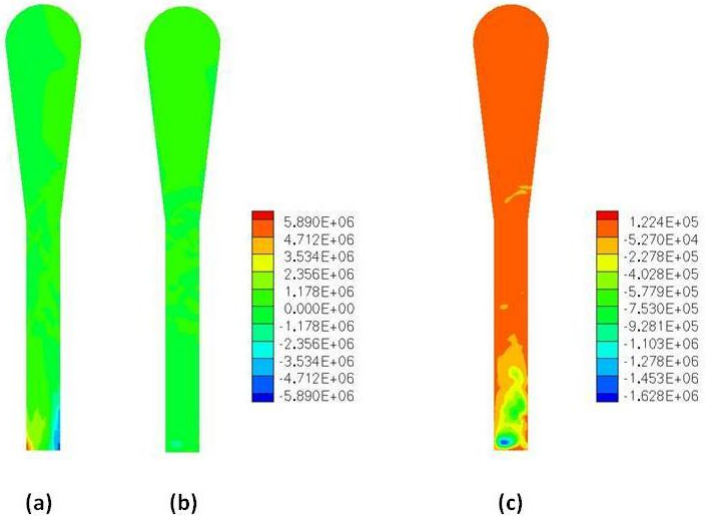

Figure 4.7 Instantaneous contours of electric field of pilot-plant fluidized-bed reactor for standard deviation = 0.01 at t=129.5 sec: (a) radial direction, (b) axial direction (same scale), (c) axial direction (reduced scale).

Figure 4.8 shows the mean volume fractions of small positively charged, medium negatively charged and large negatively charged polymer particles for the three cases. From the basic electrostatic laws a negatively charged particle is pushed away from a region of high negative potential field. For this reason near the distributor plate the negatively charged particles are pushed towards the walls and the positively charged particles towards the center of the reactor. This behavior is seen clearly in the case of standard deviation equal to 0.01. Similarly a positively charged particle near the expansion section is pushed away from a region of high positive potential field. This behavior is not clearly visible in Figure 4.8 due to the low volume fraction of the positively charged particles used in the simulations.

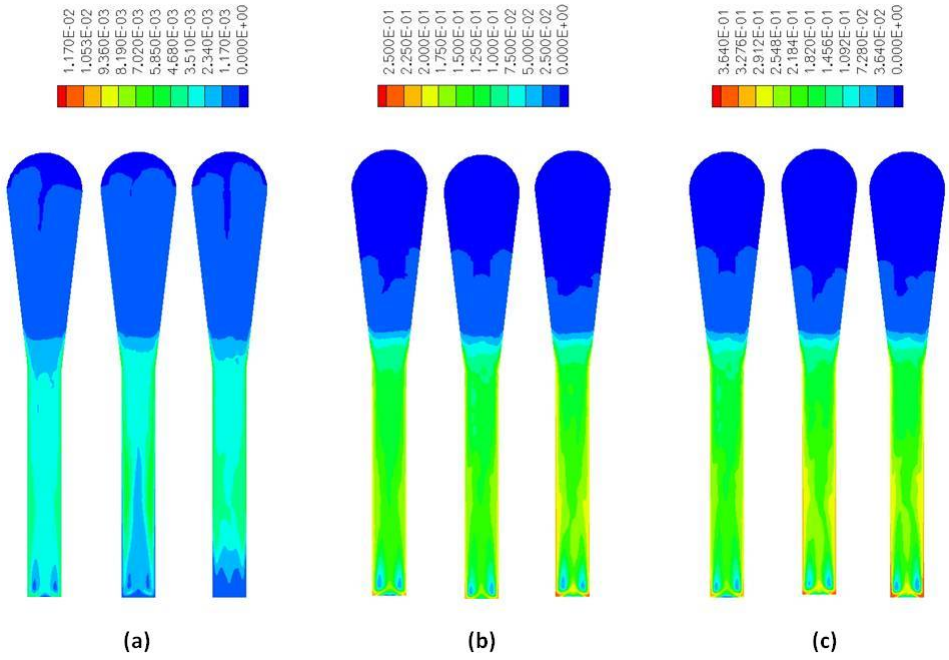

Figure 4.8 Contours of mean volume fraction of small positively charged and large negatively charged particles: (a) zero charge, (b) standard deviation = 0.001, (c) standard deviation = 0.01.

Another simulation was run with approximately ten times the charge of the 0.01 standard deviation case for each solid phase. Figure 4.9 shows the mean contour plots of the three solid phases. High volume fractions of medium and large particles are seen near the walls of the reactor close to the distributor plate. This example clearly illustrates that sufficiently high charges on the solid phase can cause agglomeration and defluidization in gas-solid fluidized

beds [73].

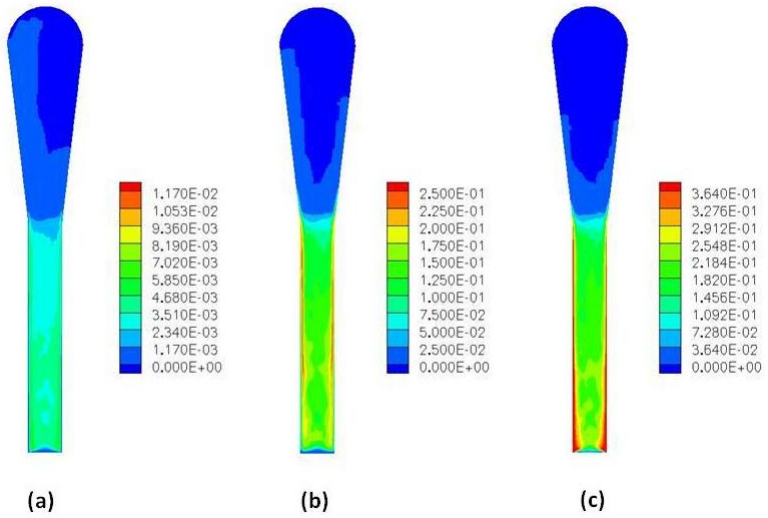

Figure 4.9 Contours of mean volume fraction of highly charged case: (a) small positively charged particles, (b) medium negatively charged particles, (c) large negatively charged particles.

4.3.2 Continuous Catalyst Injection

It is known from the experimental literature that electrostatic effects are considerable for fine polymer particles and catalyst particles as the charge per unit mass on them is high. The objective of this simulation is to study the effect of charge on a continuously injected catalyst phase (which mimics the operation of polymerization reactors). The multi-fluid CFD model solves for one gas phase and four solid phases including the catalyst phase. The properties of the catalyst and the charge on the catalyst phase are shown in Table 4.4. The catalyst is injected at a mass flux of 6.5kg/m^{2}s after the bed is fully fluidized with small, medium and large polymer particles (t=12.5 sec). The catalyst is injected into the side of the reactor about one reactor diameter above the plate Low volume fractions of catalyst phase approximating realistic conditions are used. Three cases are run with different charges on the catalyst phase. A base case with zero charge was compared to cases where, positive-, and negative charges were considered. The charge magnitude is approximated to realistic catalyst charges and the mean bed charge is negative-, as is observed in polyethylene polymer particles [17].

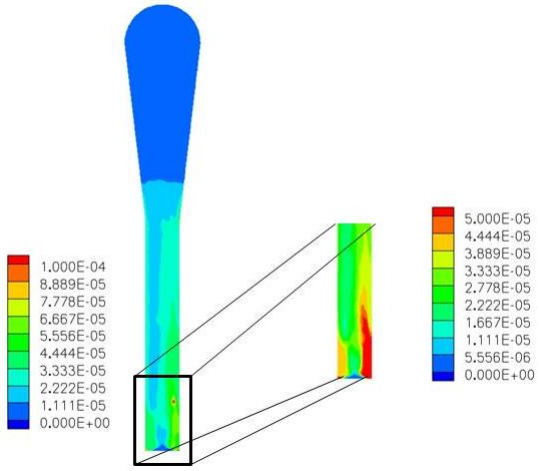

Figure 4.10 Contours of mean volume fraction of negatively charged catalyst particles.

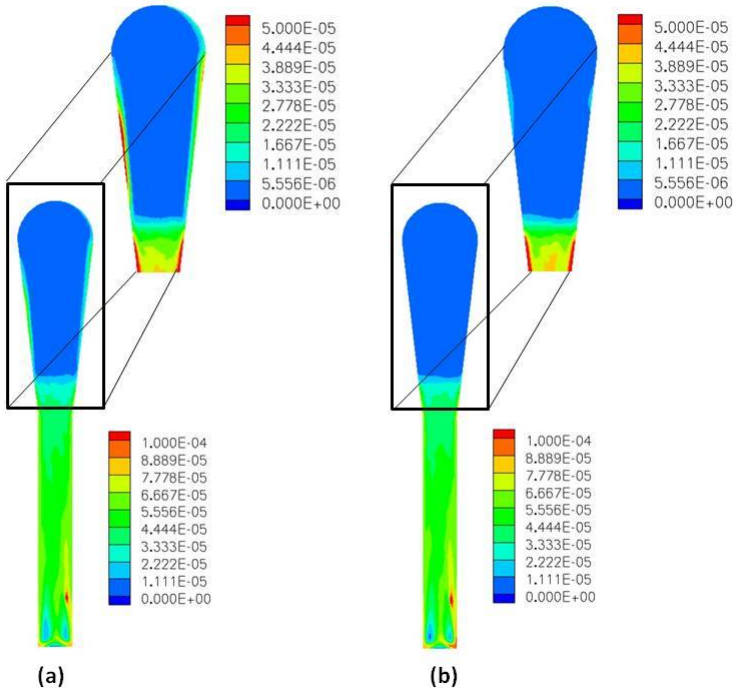

Figure 4.11 Contours of mean volume fraction of catalyst phase: (a) positive charge, (b) zero charge.

The instantaneous contour plot of volume fraction for the negatively charged catalyst phase is shown in Figure 4.10. Since the bigger particles are negatively charged and the mean bed charge is negative, the electric potential close to the injection point and near the distributor plate is negative. Due to the negative potential, the injected negatively charged catalyst particles are pushed towards the walls of the fluidized-bed zone near the distributor plate. Over a period of time the stagnant catalyst particles can form an adhered wall agglomerate or sheet if it is not remixed into the main bed. This simulation is an example where the electrostatic effects are high compared to the drag forces (even though the latter is quite large due to the small size of the catalyst particles).

Catalyst	Density, kg/m^3	Diameter,micro-meter	Charge, coulomb/m^3
	1000.0	55.0	-0.5, 0.0, 0.5

Table 4.4 Properties of solid phases used in the continuous catalyst injection simulations

Figure 4.11 shows the mean volume fractions of zero and positively charged catalyst phases. Zero charged catalyst particles followed the gas flow and are entrained out of the reactor. The positively charged catalyst particles also follow the gas phase into the expansion section where the positive electric potential pushes the positively charged catalyst particles towards the walls of the expansion and disengagement zones. High volume fractions of positively charged catalyst particles are present near the walls in the dome section of the reactor. Over a period of time such particles can also form an adhered wall layer that would lead to dome fouling.

4.3.3 Effect of Electrostatics on the Entrainment of Fines

The goal of this simulation is to study the electrostatic effects on entrainment of fine polymer particles (or fines). Three different cases are considered where the size and charge of the fines are varied. In each case simulations with and without charge are performed to study the effect of electrostatics on entrainment of the fines. The multi-fluid CFD model solves for one gas phase and four solid phases including fines. The properties of the fines are shown in Table 4.5. In these simulations the fines are considered to have the maximum positive charge ([85], [18]). Figure 4.12 shows the variation of charge as a function of particle size. The charge and particle size are normalized by their average values. q_{avg} and d_{avg} are defined as the average charge and

particle size. The bed is initialized with uniform spatial distribution of small, medium, large polymer particles and fines. The charge distribution as a function of particle size is obtained from experimental measurements at the University of Ottawa [86]. A low volume fraction of fines is used so as not to affect the bed dynamics and the mean bed charge is negative. The mass of fines in the simulation domain is computed at every time step for cases with and without charge on the fines.

	Small	Medium	Large
Density, kg/m^3	843.0	843.0	843.0
Volume fraction	0.0001	0.0001	0.0001
Diameter, micro-meter	60	120	180
Charge, coulomb/m^3	0.92	0.832	0.72

Table 4.5 Properties of fines used in entrainment study

Fines, micro-meter	Without charge,g/cm^{2}s	With charge, g/cm^{2}s
60	0.02282	0.00515
120	0.01437	0.00071
180	0.00651	0.000078

Table 4.6 Entrainment flux of fine polymer particles

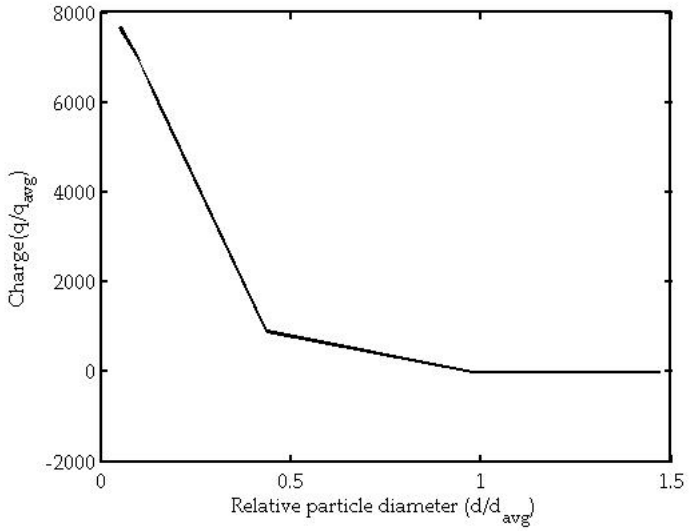

Figure 4.12 Charge distribution as a function of polymer particle size.

Figure 4.13 shows the variation of mass of fines as a function of flow time. In the first few seconds there is no entrainment observed as fines take time to reach the fluidized-bed outlet.

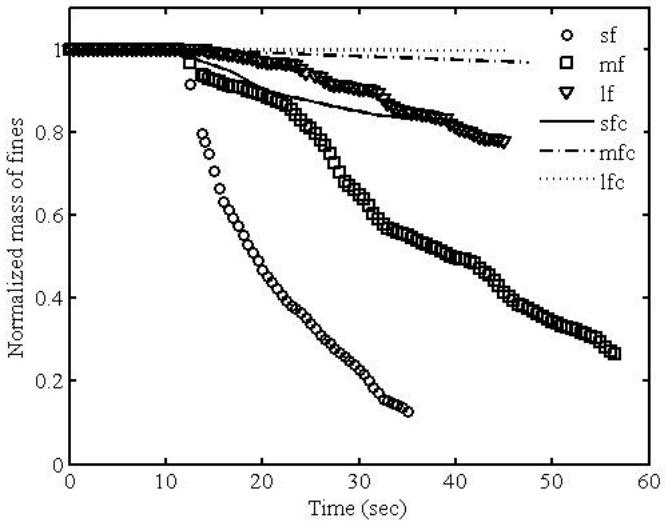

Figure 4.13 Variation of normalized mass of fines with time: sf = small fines, mf = medium fines, lf = large fines, sfc = small fines with charge, mfc = medium fines with charge, lfc = large fines with charge..

In the three cases lower entrainment is observed when there is charge on fines compared to no charge. As discussed earlier the gradient of the electric potential pushes the fines towards the walls of the reactor in the expansion and dome sections and this reduces the entrainment rate. The slope of the mass of fines versus time gives the entrainment rate and, if divided by cross-sectional area of outlet, gives the entrainment flux of fines (shown in Table 4.6). The entrainment flux decreased as the fines size increased and is lower when there is charge on fines. These predicted trends are in good agreement with experimental observations of pilot-scale polymerization reactors.

4.4 Three Dimensional Simulations

The simulations so far discussed are all two-dimensional simulations (2D). The reason is due to the high computation time and resources required for three-dimensional simulations (3D). The pilot-plant reactor and the fluidized-bed dynamics are all three-dimensional and so 3D CFD simulations are required for accurate results. Extending the two-dimensional simulations to three-dimnensions is straightforward for the simulation of the hydrodynamics of the fluidized-bed, but not for the simulation of electrostatics. In three-dimensional simulations a uniform

grid is required for the computation of electrostatics and this is explained in the next section.

4.4.1 Effect of Grid Node Distribution

The objective of this work is to study the effect of uniformity of the grid node distribution on the computation of electrostatics in gas-solid flows. A negatively charged catalyst is continuously injected into a fluidized-bed of mean negative charge. Since the bed charge is negative the computed electric potential close to the distributor plate is negative, and the injected highly negatively charged catalyst particles move towards the wall of the reactor close to the distributor plate. Figure 4.14 shows the instantaneous contours of volume fraction of catalyst at different angles of a three-dimensional simulation. From the contour plot the observed catalyst segregation due to electrostatics is in a preferential direction. To understand why segregation of catalyst particles occurred in a preferential direction, two dimensional simulations are done on circle cross section. The goal is to find out if the preferential segregation is due to any physical phenomena or due to the grid used in the simulations. To test four different grids are considered.

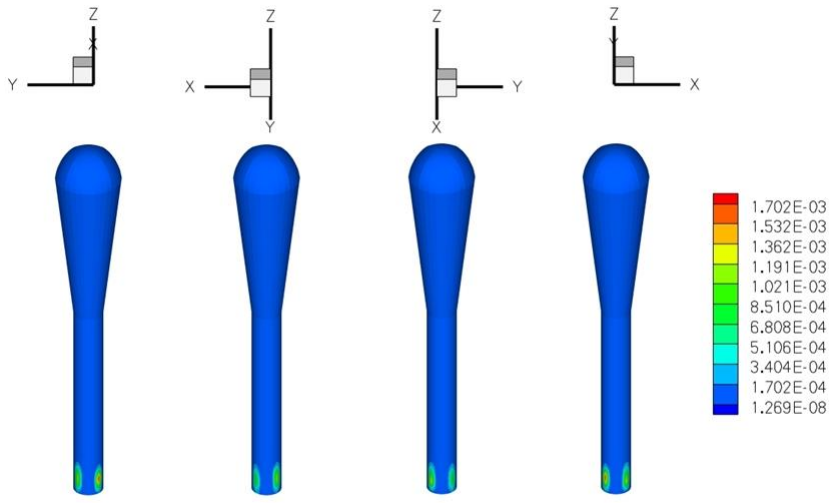

Figure 4.14 Mean negatively charged catalyst volume fraction of a three-dimensional simulation.

Figure 4.15 shows the four different grids used in the test case simulations. Mesh-1 is used in the 3D pilot-plant reactor simulations (Figure 4.14). Along with this mesh-1 three other different meshes namely mesh-2, mesh-3 and mesh-4 are also tested. Mesh-1, mesh-2,

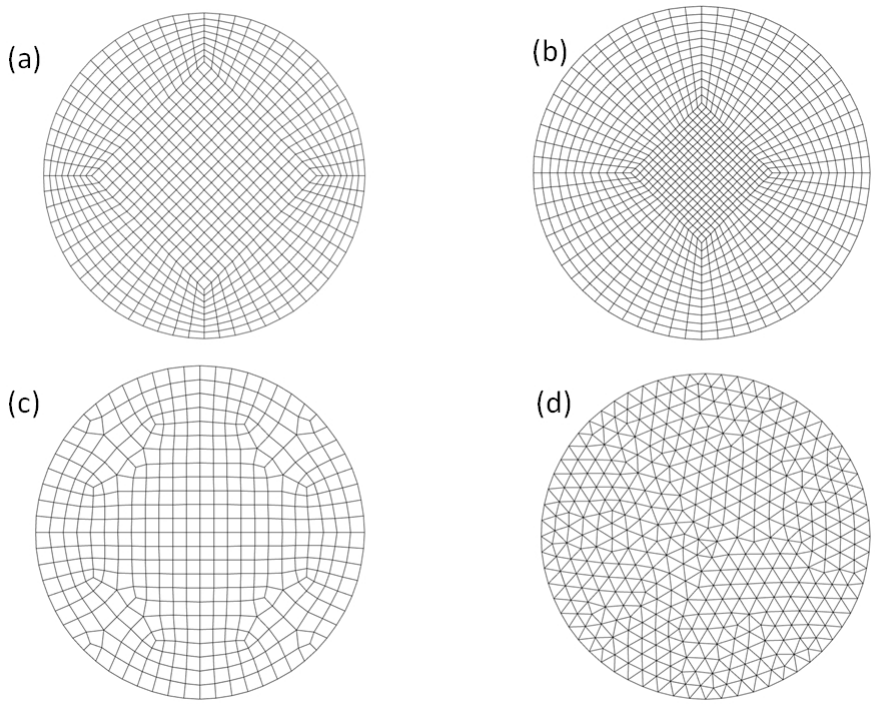

Figure 4.15 Grid used in the simulations (a) mesh-1 (b) mesh-2 (c) mesh-3 (d) mesh-4.

mesh-3 are non-uniform and show preferential directions and mesh-4 is uniform in structure. To test this multi-fluid model simulations are done on the four grids. The multi-fluid CFD model coupled with the electrostatic model is solved on a circle cross-section domain. The diameter of the domain is equal to the pilot-plant reactor diameter. There are no inlets or outlets and no gravitational forces in this test case. The gas and solid phases are initialized with zero velocity and uniformly distributed on the domain. In previous chapter (verification of electrostatic model) it is shown that segregation occurs due to the presence of charge on solid phase. The goal of this test case is to observe if any unphysical segregation occurs due to the grid used in the simulations. The wall boundary condition for the electric potential is zero. To approximate realistic conditions, the multi-fluid CFD model is used to solve for one gas and three solid phases. The gas- and solid-phase properties are shown in Table 4.2. From Table 4.2 we see that the mean charge is negative, small particles have positive charge, and medium and large particles have negative charge. The solid phase density is equal to polyethylene density, and the diameter and volume fractions of the solid phases, are obtained from the quadrature method of moments and reaction engineering model.

The electric potential evolves as the simulation progresses due to segregation of charged particles. The instantaneous contours of electric potential, gas volume fraction and volume fraction of solid phase-1, 2, 3 are shown in Figure 4.16, Figure 4.17, Figure 4.18, Figure 4.19 and Figure 4.20 for the different grids used in the simulations.

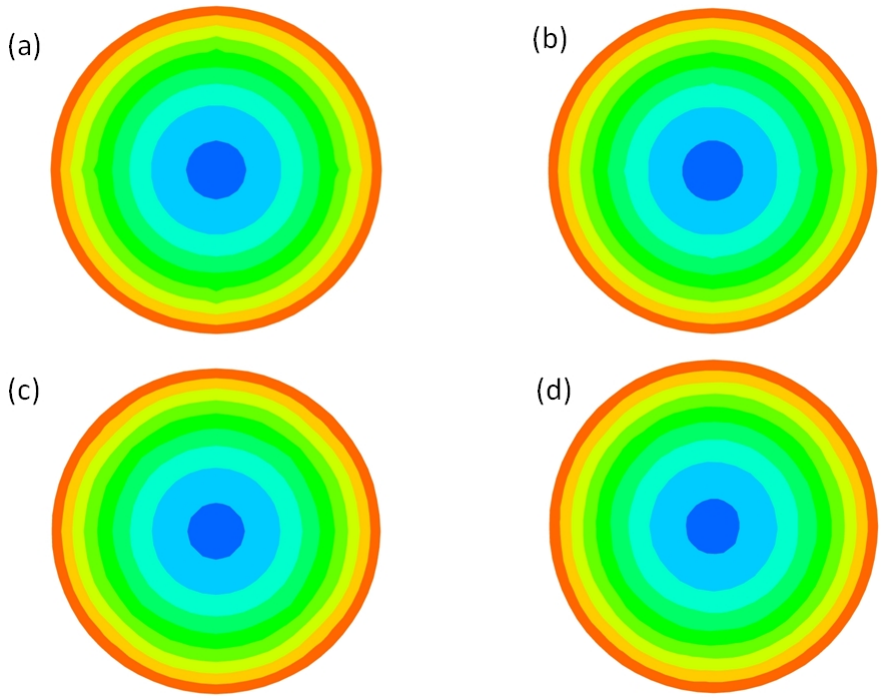

Figure 4.16 Contours of electric potential (a) mesh-1 (b) mesh-2 (c) mesh-3 (d) mesh-4.

A non-uniform electric field develops due to the presence of charged particles, and the gradient of the electric potential causes the particles to segregate inside of the cirlce domain. As seen from the contour plot, the electric potential is zero (marked by red) at the walls and negative (marked by blue) at the center of the domain. The electric field points from a region of a high potential towards low potential. Any positively charged particle will move from a region of high to a region of low potential and vice-versa for a negatively charged particle. In this simulation the negatively charged larger particles moved towards the walls, and the positively charged small particles towards the center of the domain. As we are interested in only the qualitative results the legends for the contour plots are not presented here. Figure 4.16 shows the instantaneous contour of electric potential for the four grids. The electric potential contour plots all look the same, but on close observation shows the difference in contour levels. This is

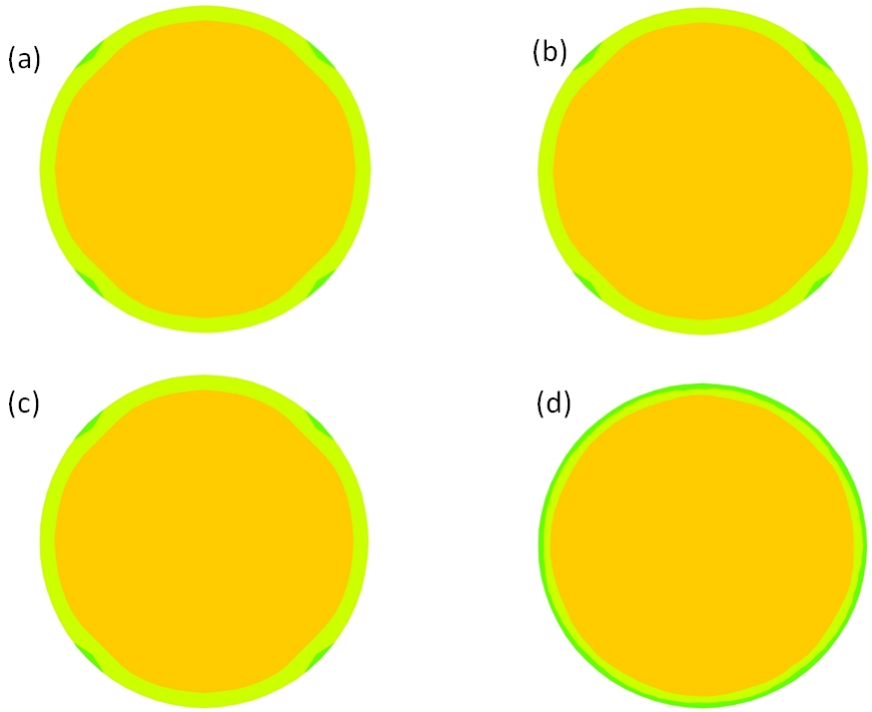

Figure 4.17 Contours of gas phase volume fraction (a) mesh-1 (b) mesh-2 (c) mesh-3 (d) mesh-4.

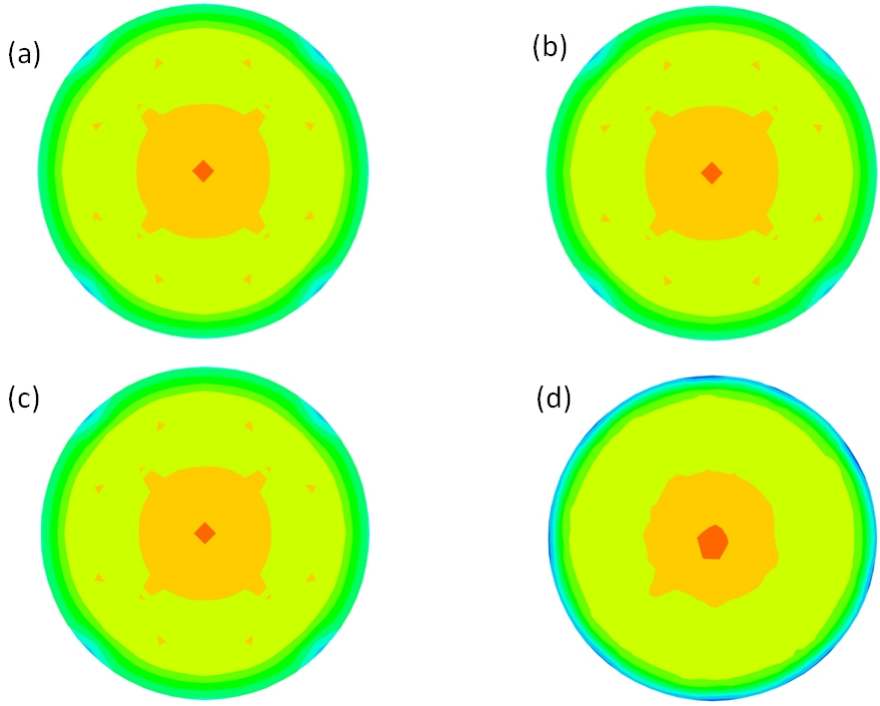

Figure 4.18 Contours of positively charged solid phase-1 volume (a) mesh-1 (b) mesh-2 (c) mesh-3 (d) mesh-4.

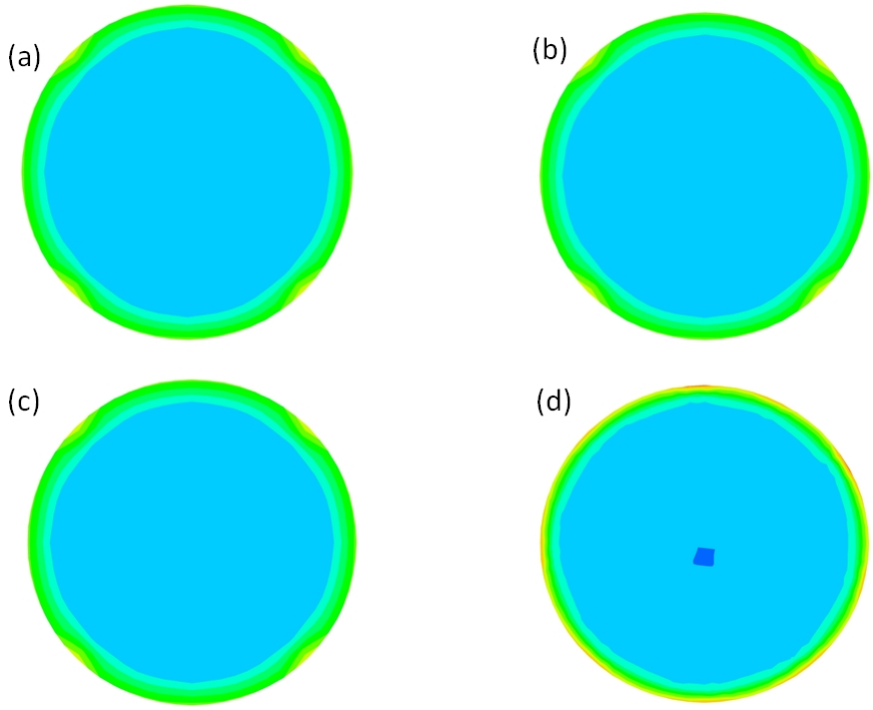

Figure 4.19 Contours of negatively charged solid phase-2 volume fraction (a) mesh-1 (b) mesh-2 (c) mesh-3 (d) mesh-4.

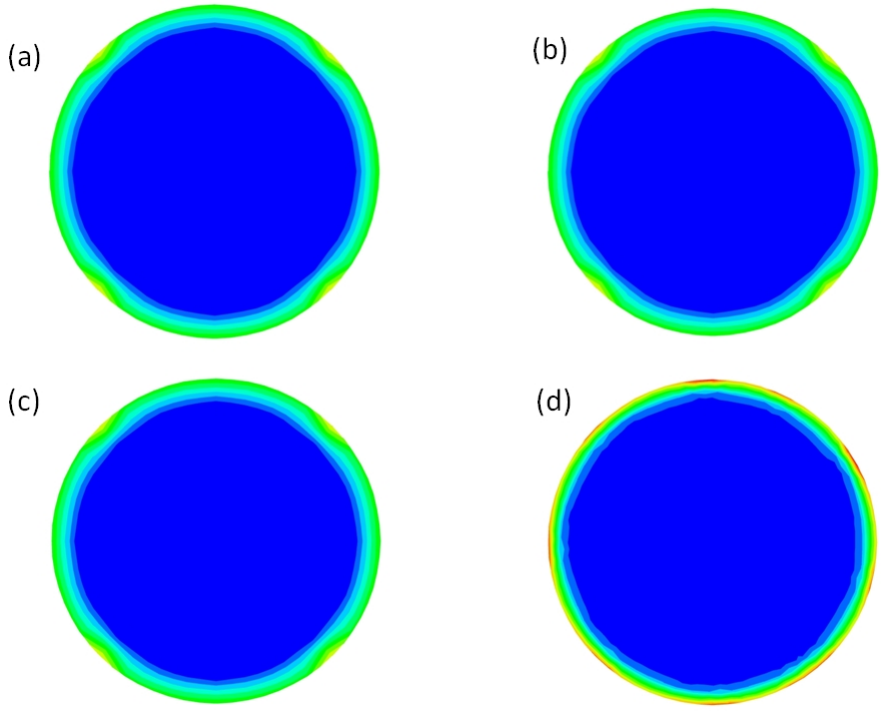

Figure 4.20 Contours of negatively charged solid phase-3 volume fraction (a) mesh-1 (b) mesh-2 (c) mesh-3 (d) mesh-4.

shown in instantaneous contours of volume fraction of gas and positively charged solid phase (Figure 4.17 and Figure 4.18) near the wall. The gas volume fraction (Figure 4.17) shows preferential direction in mesh-1, mesh-2 and mesh-3 and no such preferential direction in mesh-4. Similar behavior is seen in contours of positively charged volume fraction (Figure 4.18). In Figure 4.19, Figure 4.20 the contours of negatively charged solid phase-2, 3 are shown. For mesh-1, 2 and 3 there are regions of preferential directions and so not suitable when electrostatic model is solved. Mesh-4 also had regions of high and low, but they are almost distributed uniformly along the wall. Electrostatic model is coupled with the multi-fluid model to study the effect of grids used. Unphysical results are observed when non-uniform grids are used. When uniform grids (mesh-4) are used the simulations results look realistic and correct. Mesh-4 can now be used to run three-dimensional simulations.

4.4.2 Pilot-Scale Simulations

Three dimensional simulations of the pilot-plant reactor are run to show that segregation does occur due to electrostatics. Since it is expensive to run three dimensional simulations for all the cases, only the effects of charge magnitude on the distribution of the solid phases are simulated. The grid used in three-dimensional simulations is completely unstructured and uniform. A uniform grid is necessary to simulate electrostatic potential and its effects accurately in circular cross section geometries. The results shown here are on the Z=0 cross section in the 3D simulations. Figure 4.21 shows the contour plots of mean volume fraction of all the solid phases. The smaller positive particles (i.e. solid phase-1) segregate away from the wall close to the distributor plate. There is not much segregation observed due to the charge on bigger particles and this shows that the electrostatics effects are high for small particles compared to bigger particles. The reason is due to the high charge per unit mass of small particles. Figure 4.22 shows the contour plots of potential. The maximum value of the potential (standard deviation = 0.01) decreased from 795 kV in two-dimensional simulations to 195 kV in three-dimensional simulations. This is due to the wall effects in three-dimensional simulations. In pilot-plant reactor experiments a potential of 1-5 kV is measured next to the reactor wall. The simulation results show the potential of 10 kV which is reasonably close to the experimental

observations. Since the exact charge on the particles is not known this may also contributes to the high potential values seen in simulations. It was reported by [20] that the electric potential in a fluidized-bed frequently exceeds 20 kV.

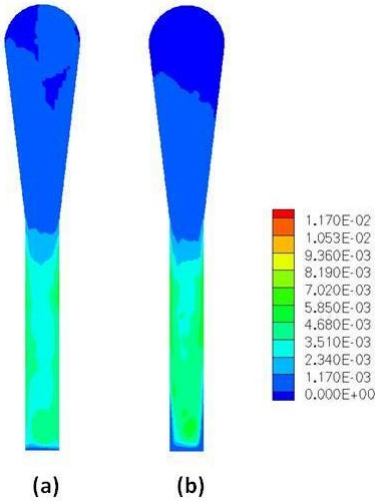

Figure 4.21 Contours of mean volume fraction of small positively charged particles of a three dimensional simulation: (a) zero charge, (b) standard deviation = 0.01.

4.5 Conclusions

An electrostatic model is coupled with a multi-fluid CFD model for gas-solid flows. Segregation of polymer particles is found and high charges were shown to induce defluidization. The electric potential and electric field results predicted from simulations are in agreement with the experimental observations in gas-solid fluidized beds. Simulations showed that the distribution of the catalyst phase depends on its charge and polarity relative to polymer particles. Electrostatics also effects the entrainment of fines due to segregation induced by the charge. Future work is needed to incorporate charge generation and dissipation mechanisms into the electrostatic model. However, by employing the known specific charges for different polymer particle sizes, the current model is able to give good qualitative estimates of the mean properties, such as the solid-phase spatial distribution and the pressure drop, and captures the trends observed when electrostatic effects are important.

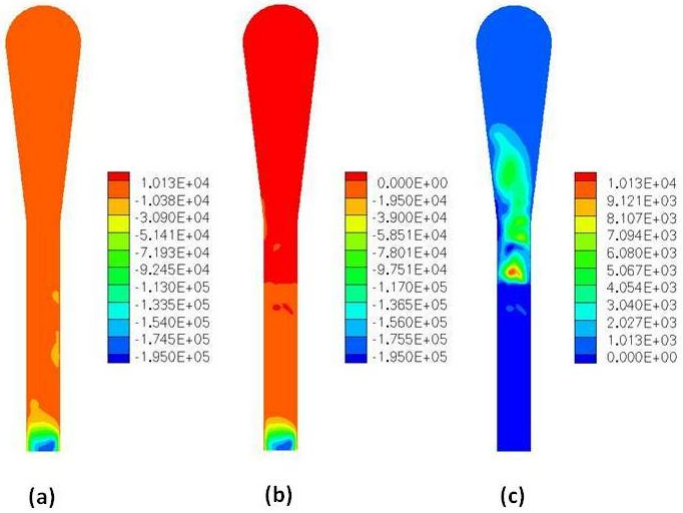

Figure 4.22 Instantaneous contours of electric potential of three-dimensional simulation of pilotplant fluidized-bed reactor for standard deviation = 0.01 at t = 35 sec: (a) total range, (b) negative range, (c) positive range.

5 FILTERED MODELS FOR GAS PARTICLE FLOWS

5.1 Introduction

Computational fluid dynamics (CFD) has only recently been explored in multiphase polymerization reactors. This is due, in large part, to the complexity of modeling these systems. There are several different length and time scales. Large-scale convection and diffusion occur on a macroscale, mid-scale mixing and particle interactions take place at the mesoscale, while complex polymerization chemistries and molecular transport are evident at the microscale. The individual catalyst particles are modeled as batch microreactors and incorporate interphase heat and mass transport as well as intraparticle diffusion. The dynamics of these different scales, the gas and solid phase interactions, heterogeneity of the different sizes of both the polymer and catalyst, and the coupling of the chemical kinetics must be considered in the CFD model. Interparticle forces include the familiar van der Waals, drag and gravity forces, but there is a growing realization of the importance of electrostatic and capillary factors as well.

CFD when coupled with today's high-performance computers, newly developed numerical and visualization algorithms and improved user interfaces has the potential to truly transform the current commercial paradigm. In today's ever more competitive environment, it important that process engineers have access to technology that allows them to make well-informed design, scale-up, and operational choices in a timely and cost-efficient manner. In this work a CFD based Eulerian-Eulerian two-fluid model will be used for scale-up studies. Using refined grids on large scale commercial fluidized-bed reactors is not possible. In such cases coarse grids have to be used and they do not resolve all the flow structures. The effect of unresolved flow structures on resolved need to be included through closure relations. The closure relations can be obtained by highly resolved simulations.

Gas-Particle flows can be modeled using two different approaches, Euler-Lagrange and Euler-Euler. In the Euler-Lagrange models the particle positon and velocity is obtained by

solving Newton's law and the fluid phase is described as a continuum. The particle-particle and particle-wall interactions are treated in a realistic manner. Fluid-particle interactions are described as closure such as Gidaspow drag law, Wen-Yu model, Syamlal model etc. In pilot and industrial scale reactors, the number of particles are the order of 10^9 and above. To solve governing equations for each particlc is computationally expensive and so the Euler-Lagrange models are restricted for systems with less number of particles, as in laboratory scale systems. Euler-Euler models treat both fluid and particle phase as continuum phase and modified Navier-Stokes equations are used to solve the mass and momentumm balance for both phases. The particle phase properties such as particle pressure and viscosities are computed using kinetic theory of granular flow and fritional theory.

Parmentier et al [87] showed the effect of grid resolution on the bubbling bed height for three particle types, Geldart A, Geldart AB and Geldart B. They observed improvements on bed-height predictions for small cell sizes. The bed-height reduced by a factor of two for Geldart A particles and unchanged for Geldart B particles. The simulations were done on a two-dimensional lab scale fluidized-bed reactor. From their conclusions, refined grids need to be performed to predict correct bed expansion in the fluidized-bed simulations. Running two-fluid refined simulations on pilot and industrial scale reactors is computationally expensive. Large industrial scale reactors typically have bed diameter $\sim$ 1 - 6 m and height of 10 - 40 m. The objective of this study is to run simulations on pilot and industrial scale reactors with coarse grids, and include sub grid models to account for the unresolved effects. The main interest is to predict correct bed expansion in dense bubbling and slug flow fluidized bed reactors. In this work a filtered model approach as described in Parmentier et al [88] and Ali [89] is used. In our study, Geldart B polymer particles ($\sim$ 1 mm)are used.

An open source OpenFOAM® CFD code is used in this study. Section 5.2 discusses the granular multiphase two-fluid code in OpenFOAM®. The code is verified and validated with published experiments and simulation results. Section 5.3 describes the governing equations of the filtered model. Section 5.4 gives details of the filtered simulations results.

5.2 Eulerian Granular Multiphase Code in OpenFOAM®

This section discusses the Eulerian-Eulerian granular (two-fluid) multiphase CFD code in OpenFOAM® ([90], [91]). The current work uses the Passalacqua and Fox [92] implementation of the continuum granular multiphase model with kinetic and frictional theory closures for particle phase in OpenFOAM®. OpenFOAM® (Open Field Operation and Manipulation) is an unstructured C++ open source finite volume CFD code. The open source code has capabilities of simulating complex, multiphase, reacting turbulent flows. The main advantage of OpenFOAM is its open source nature and the user could change the source code.

A brief description of the CFD code is presented here. Mass and momentum balance equations for gas and particle phase are solved on co-located grids using finite volume method. A fully conservative form of the equations are solved to overcome the limitations of the non conservative and semi conservative form. The particle pressure term is included in the particle phase continuity equation and solved implicitly to overcome the convergence issues. The implicit treatment of particle pressure ensured the packing condition can be enforced. An improved Rhie and Chow interpolation ([92], [93]) procedure is used. The coupling between the phases is done using partial elimination algorithm (PEA).

5.2.1 Verification and Validation

Parmentier et al [87] performed two-dimensional simulations of Geldart A, AB and B type particle bubbling-bed simulations. They performed grid refinement simulations for the three particle types and studied the influence of mesh size on the bed height predictions. Simulation cases corresponding to the Geldart particle type described in Parmentier et al [87] are used to verify and validate the multiphase granular continuum code in OpenFOAM®. The simulation geometry is two-dimensional and rectangular for each case. Table 5.1 shows the dimensions of the simulation geometry, initial conditons, gas and particle phase properties. It is important to note that the grid size used for Geldart A type particle is smaller compared to the Geldart AB and B type. The grids used are uniform square cells. A uniform gas velocity is specified as the inlet boundary condition. A full partial differential equation is solved to compute the

granular temperature. The boundary conditions for the gas and particle phase are shown in Table 5.2. The numerical schemes used in the simulation and the under relaxation factors for the different variables are shown in Table 5.3 and Table 5.4. Kinetic theory of granular flow (KTGF) and frictional theory are used to calculate particle phase properties such as particle pressure and viscosity.

Table 5.1 Properties of gas and solid phase used in the verification and validation of OpenFOAM® simulation

Particle type	Group A	Group AB	Group B
Width, m	0.03	0.138	0.138
Height, m	0.50	1.00	1.00
Initial height, m	0.10	0.20	0.20
Inital particle volume fraction	0.55	0.58	0.58
Particle diameter, μm	75	125	350
Particle density, kg/m^3	1500	2500	2500
Restitution coefficient	0.95	0.80	0.80
Gas density, kg/m^3	1.186	1.4	1.4
Gas viscosity, Pa.s	1.8e-05	1.8e-05	1.8e-05
Superficial velocity, m/s	0.10	0.26	0.54
Mesh size, mm	1	3	10

Table 5.2 Boundary conditions used in the verification and validation simulation

Region	Boundary Condition
Inlet	Velocity of gas phase
Outlet	Pressure outlet
Wall	Zero slip for gas phase
	Partial slip for particle phase (Johnson-Jackson [94])
	Johnson-Jackson condition for granular temperature

Figure 5.1 shows the instantaneous contours of particle volume fraction for the three Geldart type particles. Flow structures such as bubble shapes are well resolved in the simulations. Higher order discretization schemes and small grid sizes are necessary to avoid numerical diffusion and simulate bubbles with accurate shape. Spatially inhomogeneous structures are seen with regions of low (dilute) and high (dense) volume fraction of particles. There is particle recirculation and mixing due to the resolved bubbles. Figure 5.2, 5.3 and 5.4 shows the

Table 5.3 Numerical schemes of verification and validation simulations

Term	Numerical configuration
$\partial/\partial t$	Euler implict
$\nabla\psi$	cellLimited Gauss linear 1
∇p	Gauss linear
$\nabla\cdot\psi$	cellLimited Gauss linear 1
$\nabla\cdot(\mathbf{U}_i\mathbf{U}_i)$	Gauss linearUpwindV cellLimited Gauss linear 1
$\nabla\cdot(\mathbf{U}_i\alpha_i)$	Gauss linearUpwind cellLimited Gauss linear 1
$\nabla\cdot\tau_i$	Gauss linear
$\nabla^2\psi$	Gauss linear corrected
$\nabla^{\perp}\psi$	Corrected
$(\psi)_{\mathrm{f}}$	Linear

Table 5.4 Numerical settings used in the verification and validation simulation

Variable	Under relaxation factor
$\mathbf{U}_i$	0.7
p	0.3
α_i	0.2
Θ_{p}	0.2

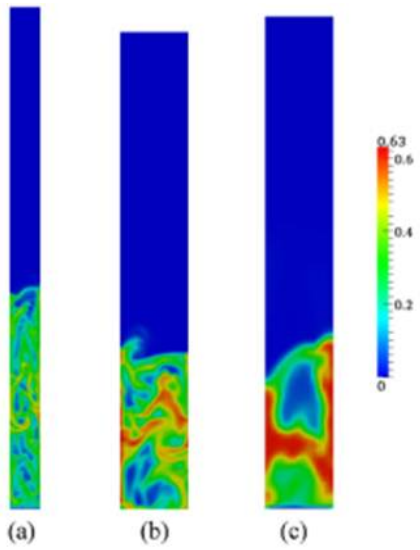

Figure 5.1 Instantaneous contours of particle volume fraction (a) Geldart A (b) Geldart AB (c) Geldart B, blue region: zero particle volume fraction, red region: 0.63 particle volume fraction.

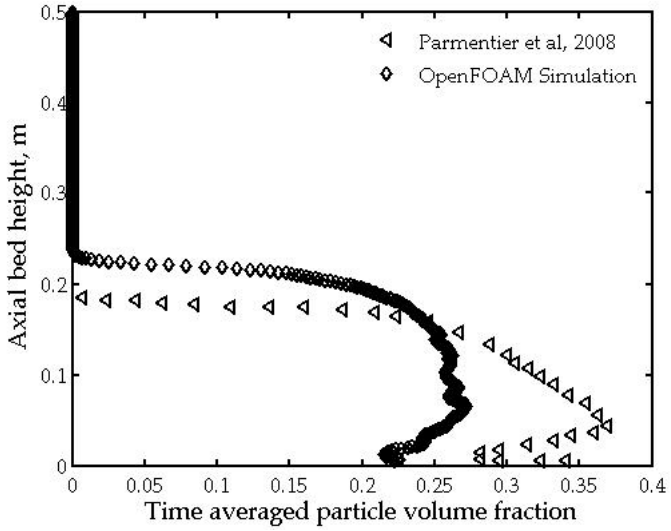

Figure 5.2 Mean particle volume fraction for Geldart A type particle along the fluidized-bed height.

time averaged axial particle volume fractions for Geldart A, AB and B type in OpenFOAM® and published simulation results [87]. The time averaged particle volume fraction decreased along the bed height. There is a good comparison between the OpenFOAM two-fluid model and published simulation results. Figure 5.5 and 5.6 shows the time averaged particle volume fractions along the radial direction. High particle volume fraction near the walls due to segregation observed in experiments [95] is well predicted by current CFD simulations.

5.2.2 Effect of Grid Resolution on Bed Height

The section describes the effect of grid resolution on bed height in a pilot scale fluidized-bed reactor. For simplicity, the expansion section as described in Chapter 4 is replaced by straight section. The gas and particle phase properties are shown in Table 5.5. Two-fluid model simulations are run with different mesh sizes ranging from 6 to 75 mm. The mean contours of particle volume fraction at two different bed heights in shown in Figure 5.7 and 5.8. For coarse grids, flat volume fraction profiles are observed. With refined grids, higher particle volume fraction is observed near the wall, due to particle segregation and consistent with experimental observations. Instantaneous and mean contours of particle volume fraction are shown in Figure 5.9 and 5.10. With higher grid resolution, the instantaneous contours

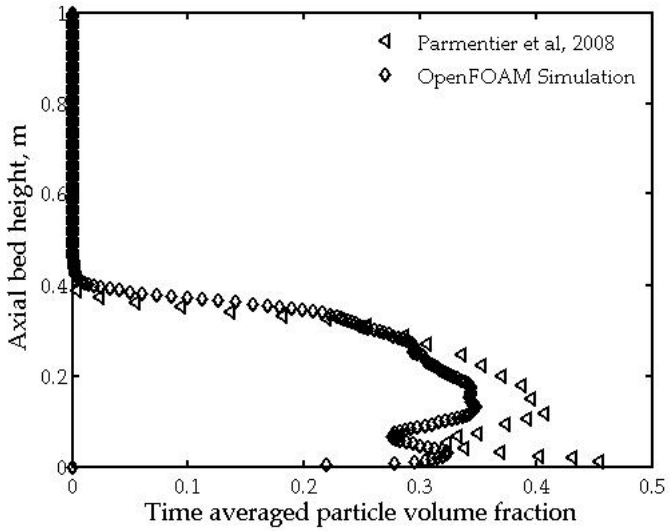

Figure 5.3 Mean particle volume fraction for Geldart AB type particle along the fluidized-bed height.

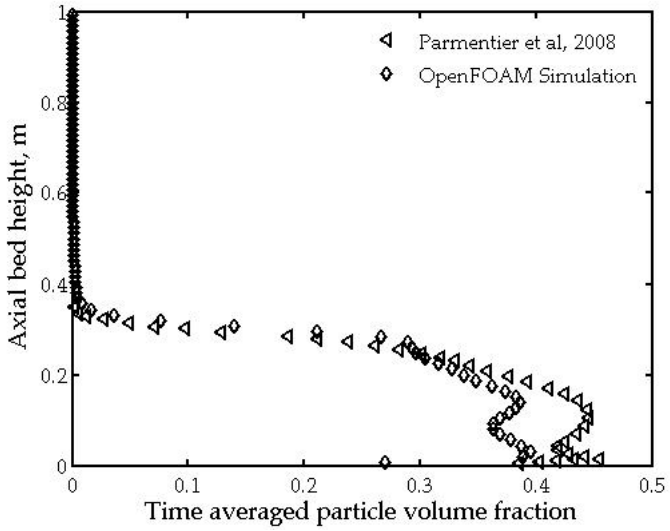

Figure 5.4 Mean particle volume fraction for Geldart B type particle along the fluidized-bed height.

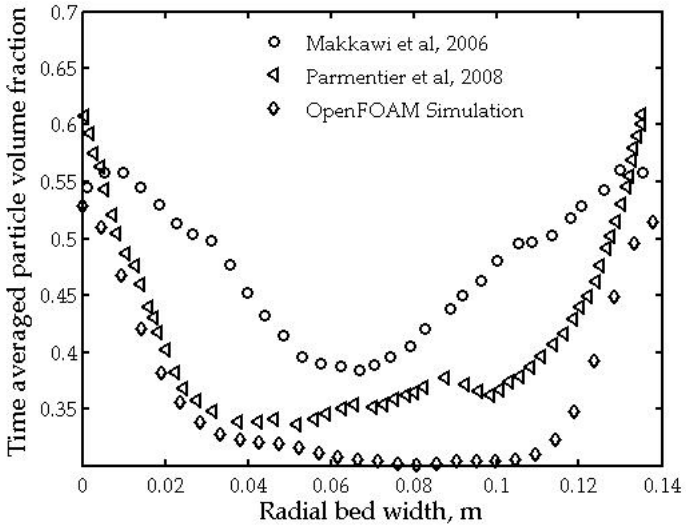

Figure 5.5 Mean particle volume fraction for Geldart AB type particle along the fluidized-bed width.

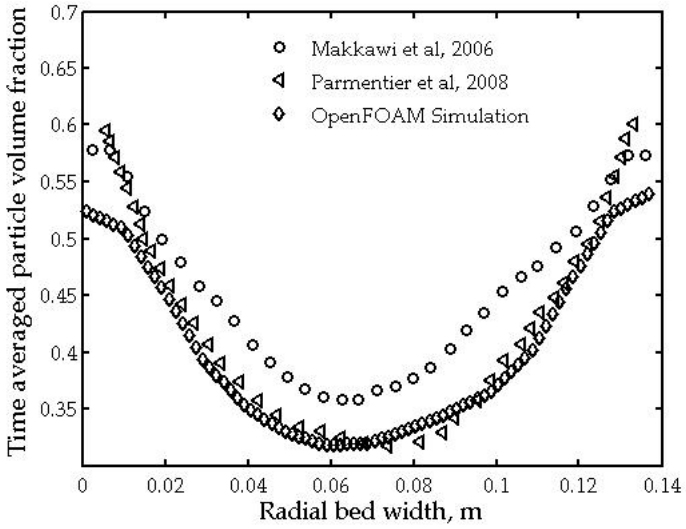

Figure 5.6 Mean particle volume fraction for Geldart B type particle along the fluidized-bed width.

show more particle clusters, with particle volume fraction close to packing limit (red region: 0.63), where as the coarse grids did not simulate such structures and uniform volume fractions are observed. The bed height decreased (Figure 5.10) as the grid resolution is increased and a grid independent bed height is obtained for small grid sizes. The mean contours also show high particle volume fraction near the wall for refined mesh cases. Figure 5.11 shows the mean static pressure along the axial fluidized-bed height. The mean static pressure decreased linearly and constant above the bed height. Figure 5.12 shows the mean static pressure profile close to the fluidized-bed distributor plate.

Table 5.5 Properties of gas and solid phase used in the simulation

Pilot Scale Simulation Conditions	
Width, m	0.40 - 0.60
Height, m	6.00 - 10.00
Particle diameter, μm	1200
Particle density, kg/m^3	843
Restitution coefficient	0.8
Gas density, kg/m^3	22.1
Gas viscosity, Pa.s	1.427e-05
Superficial velocity, m/s	0.61
Mesh size, mm	6 - 75

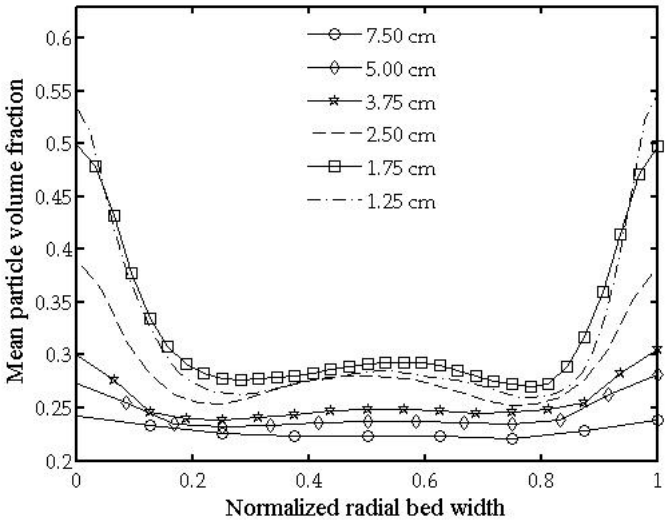

Figure 5.7 Mean particle volume fraction along the bed width at normalized bed height = 0.27.

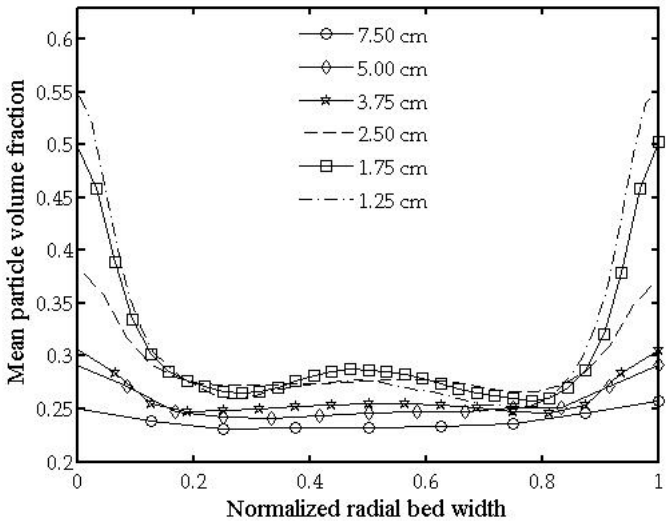

Figure 5.8 Mean particle volume fraction along the bed width at normalized bed height = 0.40.

5.3 Filtered Models

In the previous section, it is shown that small structures are predicted and resolved by refined two-fluid simulations. Refined grids are a requirement to predict correct bed expansion, but its application on pilot and industrial scale reactors is not possible due to practical limitations. The objective of this research is to use coarse grids and the effect of unresolved structures are accounted through subgrid scale models. The filtered approach described in Parmentier et al [88] and Ali [89] is used in this work. The idea is similar to single phase large eddy simulations (LES), where the large eddies are resolved and smaller unresolved structures are modeled.

The physical variables are written as a resolved and an unresolved (subgrid) part. The resolved part of the variable is computed in the coarse grid simulation and the sugrid correction is included as a model. By definition, $\overline{f}(\mathbf{x},t)$ is the resolved or filtered part of a variable $f(\mathbf{x},t)$

$$\overline{f}\left(\mathbf{x},t\right)=\int\int\int G\left(\mathbf{x}-\mathbf{y}\right)f\left(\mathbf{y},t\right) \tag{5.1}$$

G is a weight function and satisfies $\int\int\int G(y)dy=1$.

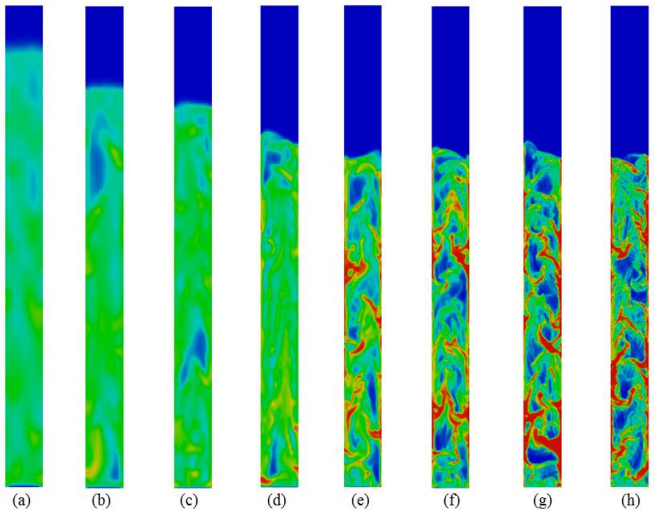

Figure 5.9 Instantaneous contours of particle volume fraction for grid sizes (a) 7.50 cm (b) 5.00 cm (c) 3.75 cm (d) 2.50 cm (e) 1.75 cm (f) 1.25 cm (g) 0.90 cm (h) 0.75 cm. blue region: zero volume fraction, red region: 0.63

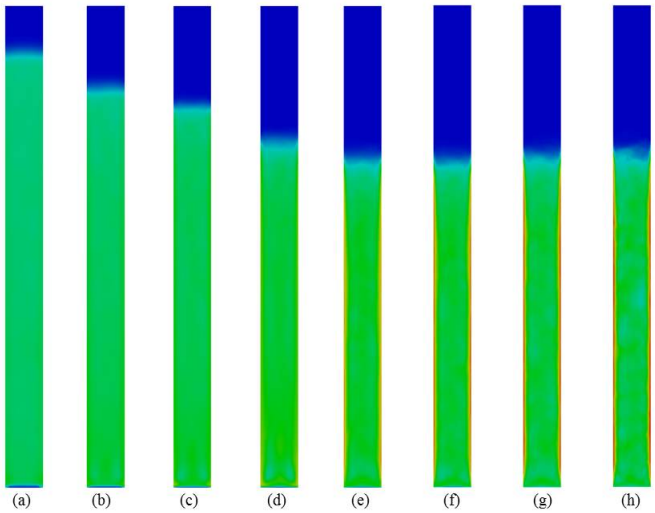

Figure 5.10 Mean contours of particle volume fraction for grid sizes (a) 7.50 cm (b) 5.00 cm (c) 3.75 cm (d) 2.50 cm (e) 1.75 cm (f) 1.25 cm (g) 0.90 cm (h) 0.75 cm.blue region: zero volume fraction, red region: 0.63

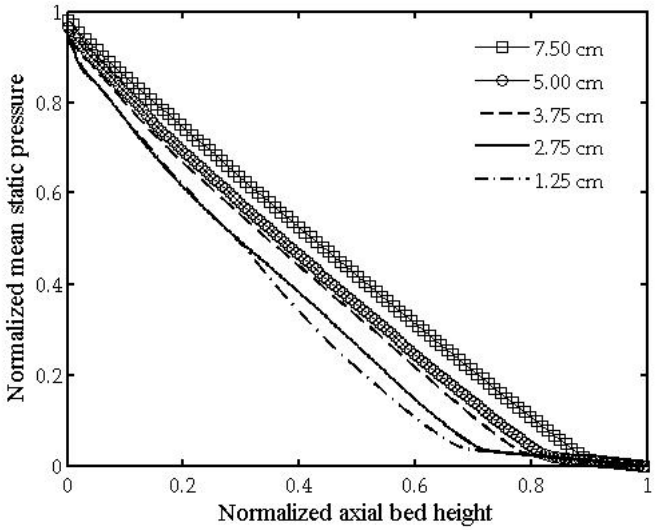

Figure 5.11 Mean static pressure along the bed height for different grid sizes.

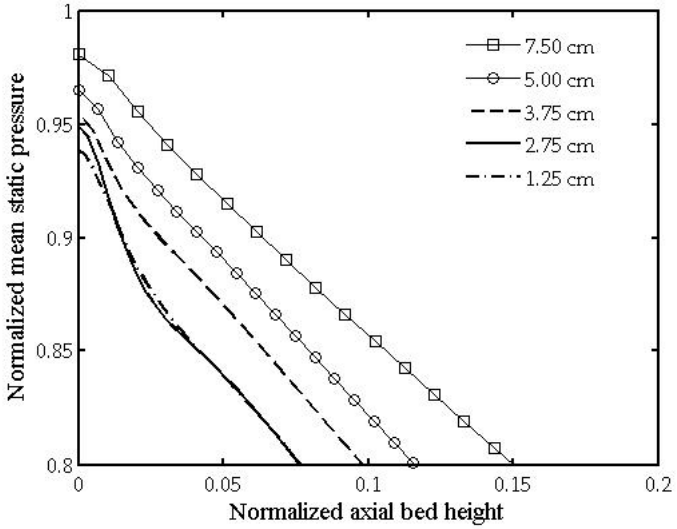

Figure 5.12 Mean static pressure along close to the distributor plate for different grid sizes.

5.3.1 Governing Equations

The filtered model governing equations for the particle and gas phase are given below. Filtered particle volume fraction $\overline{\alpha}_{\mathrm{p}}(\mathbf{x},t)$ is defined as

$$\overline{\alpha}_{\mathrm{p}}(\mathbf{x},t) = \int\int\int G(\mathbf{x}-\mathbf{y})\,\alpha_{\mathrm{p}}(\mathbf{y},t) \tag{5.2}$$

Filtered gas phase $\tilde{\mathbf{U}}_{\mathrm{g}}(\mathbf{x},t)$ and particle phase velocities $\tilde{\mathbf{U}}_{\mathrm{p}}(\mathbf{x},t)$ are defined by

$$\tilde{\mathbf{U}}_{\mathrm{p}}(\mathbf{x},t) = \frac{1}{\overline{\alpha}_{\mathrm{p}}}\int\int\int G(\mathbf{x}-\mathbf{y})\,\alpha_{\mathrm{p}}(\mathbf{y},t)\,\mathbf{U}_{\mathrm{p}}(\mathbf{y},t) \tag{5.3}$$

$$\tilde{\mathbf{U}}_{\mathrm{g}}(\mathbf{x},t) = \frac{1}{\overline{\alpha}_{\mathrm{g}}}\int\int\int G(\mathbf{x}-\mathbf{y})\,\alpha_{\mathrm{g}}(\mathbf{y},t)\,\mathbf{U}_{\mathrm{g}}(\mathbf{y},t) \tag{5.4}$$

The filtered velocities can also be written as $\tilde{\mathbf{U}}_{\mathrm{p}} = \frac{\overline{\alpha_{\mathrm{p}}\mathbf{U}_{\mathrm{p}}}}{\overline{\alpha}_{\mathrm{p}}}$, $\tilde{\mathbf{U}}_{\mathrm{g}} = \frac{\overline{\alpha_{\mathrm{p}}\mathbf{U}_{\mathrm{g}}}}{\overline{\alpha}_{\mathrm{g}}}$, and filtered granular temperature $\tilde{\Theta}_{\mathrm{p}} = \frac{\overline{\alpha_{\mathrm{p}}\Theta_{\mathrm{p}}}}{\overline{\alpha}_{\mathrm{p}}}$ The filtered continuity equations for the gas and particle phase are:

$$\frac{\partial}{\partial t}(\overline{\alpha}_{\mathrm{p}}\rho_{\mathrm{p}}) + \nabla\cdot(\overline{\alpha}_{\mathrm{p}}\rho_{\mathrm{p}}\tilde{\mathbf{U}}_{\mathrm{p}}) = 0 \tag{5.5}$$

$$\frac{\partial}{\partial t}(\overline{\alpha}_{\mathrm{g}}\rho_{\mathrm{g}}) + \nabla\cdot(\overline{\alpha}_{\mathrm{g}}\rho_{\mathrm{g}}\tilde{\mathbf{U}}_{\mathrm{g}}) = 0 \tag{5.6}$$

The filtered momentum equation of the gas phase is

$$\begin{aligned}\frac{\partial}{\partial t}(\overline{\alpha}_{\mathrm{g}}\rho_{\mathrm{g}}\tilde{\mathbf{U}}_{\mathrm{g}}) + \nabla\cdot(\overline{\alpha}_{\mathrm{g}}\rho_{\mathrm{g}}\tilde{\mathbf{U}}_{\mathrm{g}}\tilde{\mathbf{U}}_{\mathrm{g}}) \;=\; & -\overline{\alpha}_{\mathrm{g}}\nabla\overline{P} - \Phi_b^{\mathrm{sgs}} \\ & -\nabla\cdot(\overline{\alpha}_{\mathrm{g}}\tilde{\boldsymbol{\tau}}_{\mathrm{g}}) - \Phi_{\mathrm{g,s}}^{\mathrm{sgs}} \\ & \tilde{K}_{\mathrm{gp}}(\tilde{\mathbf{U}}_{\mathrm{p}} - \tilde{\mathbf{U}}_{\mathrm{g}}) + \Phi_{\mathrm{g,d}}^{\mathrm{sgs}} \\ & -\nabla\cdot\left(\overline{\alpha}_{\mathrm{g}}\rho_{\mathrm{g}}\boldsymbol{\sigma}_{\mathrm{g}}^{\mathrm{sgs}}\right) + \overline{\alpha}_{\mathrm{g}}\rho_{\mathrm{g}}\mathbf{g}\end{aligned} \tag{5.7}$$

The first line on the RHS of the above equation is the resolved buoyancy ($\overline{\alpha}_{\mathrm{g}}\nabla\overline{P}$) and sub grid contribution (Φ_b^{sgs}). The second line is the resolved gas phases stresses ($\nabla\cdot(\overline{\alpha}_{\mathrm{g}}\tilde{\boldsymbol{\tau}}_{\mathrm{g}})$) and sub grid stresses contribution ($\Phi_{\mathrm{g,s}}^{\mathrm{sgs}}$). Third line is the resolved gas-particle interaction force ($\tilde{K}_{\mathrm{gp}}(\tilde{\mathbf{U}}_{\mathrm{p}} - \tilde{\mathbf{U}}_{\mathrm{g}})$) and subgrid drag contribution ($\Phi_{\mathrm{g,d}}^{\mathrm{sgs}}$). First term on the fourth line is the reynolds stress like contribution and obtsined from filtering the convection term. The last term

is the resolved gravity contribution. The filtered particle phase momentum equation is defined as:

$$\begin{aligned}\frac{\partial}{\partial t}(\overline{\alpha}_{\mathrm{p}}\rho_{\mathrm{p}}\tilde{\mathbf{U}}_{\mathrm{p}}) + \nabla\cdot(\overline{\alpha}_{\mathrm{p}}\rho_{\mathrm{p}}\tilde{\mathbf{U}}_{\mathrm{p}}\tilde{\mathbf{U}}_{\mathrm{p}}) &= -\overline{\alpha}_{\mathrm{p}}\nabla\overline{P} - \Phi_b^{\mathrm{sgs}} \\ &\quad -\nabla\overline{p}_{\mathrm{p}} - \Phi_{\mathrm{p,p}}^{\mathrm{sgs}} \\ &\quad -\nabla\cdot(\overline{\alpha}_{\mathrm{p}}\tilde{\boldsymbol{\tau}}_{\mathrm{p}}) - \Phi_{\mathrm{p,s}}^{\mathrm{sgs}} \\ &\quad \tilde{K}_{\mathrm{gp}}(\tilde{\mathbf{U}}_{\mathrm{g}} - \tilde{\mathbf{U}}_{\mathrm{p}}) + \Phi_{\mathrm{p,d}}^{\mathrm{sgs}} \\ &\quad -\nabla\cdot\left(\overline{\alpha}_{\mathrm{p}}\rho_{\mathrm{p}}\boldsymbol{\sigma}_{\mathrm{p}}^{\mathrm{sgs}}\right) + \overline{\alpha}_{\mathrm{p}}\rho_{\mathrm{p}}\mathbf{g}\end{aligned} \tag{5.8}$$

The description of the terms are similar to the gas phase filtered equation. Terms in the second line are the resolved particle pressure ($\nabla\overline{p}_{\mathrm{p}}$) and its subgrid contribution ($\Phi_{\mathrm{p,p}}^{\mathrm{sgs}}$). The gas and particle phase resolved stresses are defined as:

$$\tilde{\boldsymbol{\tau}}_{\mathrm{g}} = \mu_{\mathrm{g}}\left[\nabla\tilde{\mathbf{U}}_{\mathrm{g}} + \left(\nabla\tilde{\mathbf{U}}_{\mathrm{g}}\right)^{\mathrm{T}}\right] - \frac{2}{3}\mu_{\mathrm{g}}\left(\nabla.\tilde{\mathbf{U}}_{\mathrm{g}}\right)\mathbf{I} \tag{5.9}$$

$$\tilde{\boldsymbol{\tau}}_{\mathrm{p}} = \tilde{\mu}_{\mathrm{p}}\left[\nabla\tilde{\mathbf{U}}_{\mathrm{p}} + \left(\nabla\tilde{\mathbf{U}}_{\mathrm{p}}\right)^{\mathrm{T}}\right] + \left(\tilde{\lambda}_{\mathrm{p}} - \frac{2}{3}\tilde{\mu}_{\mathrm{p}}\right)\left(\nabla.\tilde{\mathbf{U}}_{\mathrm{p}}\right)\mathbf{I} \tag{5.10}$$

The resolved drag coefficients are described as:

$$\tilde{K}_{\mathrm{gp}} = \begin{cases} \frac{3}{4}\frac{\tilde{C}_{\mathrm{d}}\overline{\alpha}_{\mathrm{g}}\overline{\alpha}_{\mathrm{p}}\rho_{\mathrm{g}}|\tilde{\mathbf{U}}_{\mathrm{g}}-\tilde{\mathbf{U}}_{\mathrm{p}}|}{d_{\mathrm{p}}} & \overline{\alpha}_{\mathrm{p}} < 0.2 \\ 150\frac{\mu_{\mathrm{g}}\overline{\alpha}_{\mathrm{p}}^2}{\overline{\alpha}_{\mathrm{p}}^2 d_{\mathrm{p}}^2} + 1.75\frac{\rho_{\mathrm{g}}\overline{\alpha}_{\mathrm{p}}}{\overline{\alpha}_{\mathrm{g}}d_{\mathrm{p}}}|\tilde{\mathbf{U}}_{\mathrm{g}} - \tilde{\mathbf{U}}_{\mathrm{p}}| & \overline{\alpha}_{\mathrm{p}} > 0.2 \end{cases} \tag{5.11}$$

$$\tilde{C}_{\mathrm{d}} = \begin{cases} \frac{24}{\tilde{R}e_{\mathrm{p}}}\left(1 + 0.15\tilde{R}e_{\mathrm{p}}^{0.687}\right) & \tilde{R}e_{\mathrm{p}} < 1000 \\ 0.44 & \tilde{R}e_{\mathrm{p}} \geq 1000 \end{cases} \tag{5.12}$$

$$\tilde{R}e_{\mathrm{p}} = \frac{\rho_{\mathrm{g}}d_{\mathrm{p}}|\tilde{\mathbf{U}}_{\mathrm{g}} - \tilde{\mathbf{U}}_{\mathrm{p}}|}{\mu_{\mathrm{g}}} \tag{5.13}$$

The filtered granular temperature equation is defined as:

$$\begin{aligned}\frac{3}{2}\left[\frac{\partial}{\partial t}(\overline{\alpha}_{\mathrm{p}}\rho_{\mathrm{p}}\tilde{\Theta}_{\mathrm{p}}) + \nabla\cdot(\overline{\alpha}_{\mathrm{p}}\rho_{\mathrm{p}}\tilde{\mathbf{U}}_{\mathrm{p}}\tilde{\Theta}_{\mathrm{p}})\right] &= \nabla\cdot(\tilde{\kappa}_{\mathrm{p}}\nabla\Theta_{\mathrm{p}}) + \Phi_{\mathrm{dif}}^{\mathrm{sgs}} \\ &\quad (-\tilde{p}_p\mathbf{I} + \tilde{\boldsymbol{\tau}}_{\mathrm{p}}) : \nabla\tilde{\mathbf{U}}_{\mathrm{p}} + \Phi_{\mathrm{gen}}^{\mathrm{sgs}} \\ &\quad -3\tilde{K}_{\mathrm{gp}}\tilde{\Theta}_{\mathrm{p}} - \Phi_{vis}^{\mathrm{sgs}} \\ &\quad -\tilde{\gamma}_{\mathrm{p}} - \Phi_{\mathrm{dis}}^{\mathrm{sgs}} \\ &\quad -\frac{3}{2}\nabla\cdot\left(\widetilde{\mathbf{U}_{\mathrm{p}}\Theta_{\mathrm{p}}} - \tilde{\Theta}_{\mathrm{p}}\tilde{\mathbf{U}}_{\mathrm{p}}\right)\end{aligned} \tag{5.14}$$

The terms on the RHS first line are the resolved diffusion $\nabla \cdot (\tilde{\kappa}_{\rm p} \nabla \Theta_{\rm p})$ and the subgrid contribution $\Phi^{\rm sgs}_{\rm dif}$. The second line is the resolved generation of granular energy $(-\tilde{p}_p \mathbf{I} + \tilde{\boldsymbol{\tau}}_{\rm p}) : \nabla \tilde{\mathbf{U}}_{\rm p}$ and the subgrid contribution $\Phi^{\rm sgs}_{\rm gen}$. Third line has resolved dissipation due the drag contribution $3\tilde{K}_{\rm gp}\tilde{\Theta}_{\rm p}$ and subgrid contribution $\Phi^{\rm sgs}_{vis}$. Fourth line has the resolved dissipation due to particle collisions $\tilde{\gamma}_{\rm p}$ and subgrid contribution $\Phi^{\rm sgs}_{\rm dis}$. The last term is the contribution from the convection term.

5.3.2 Budget Analysis

The grid independent simulation result from the previous section is used for the budget analysis of the filtered particle momentum equation. The objective of this exercise is to identify the important terms for the prediction of correct bed height. The refined simulation is referred as Direct Numerical Simulation and the grid size as Δ_{DNS}. The refined simulation results will be used to provide closures for the sub grid contribution in filtered momentume equations. Instantaneous particle volume fraction of the DNS is shown in Figure 5.13. After the initial transients, the instantaneous fields are used to obtain filtered variables such as particle volume fraction, mixture pressure, particle granular temperature, gas and particle phase velocities for a given filter size equal to 3 Δ_{DNS}, 5 Δ_{DNS}, 7 Δ_{DNS}, 9 Δ_{DNS} etc. The filtered values are considered as statistically equivalent and used to perform volume averaging. The average of the momentum balance equation along the mean flow direction is defined as

$$\begin{aligned} 0 \;=\; & -\overline{<\overline{\alpha}_{\rm p} \nabla \overline{P}>} - \overline{<\Phi^{\rm sgs}_{b}>} \\ & -\overline{<\nabla \overline{p}_{\rm p}>} - \overline{<\Phi^{\rm sgs}_{\rm p,p}>} \\ & -\overline{<\nabla \cdot (\overline{\alpha}_{\rm p} \tilde{\boldsymbol{\tau}}_{\rm p})>} - \overline{<\Phi^{\rm sgs}_{\rm p,s}>} \\ & \overline{<\tilde{K}_{\rm gp}(\tilde{\mathbf{U}}_{\rm g} - \tilde{\mathbf{U}}_{\rm p})>} + \overline{<\Phi^{\rm sgs}_{\rm p,d}>} \\ & -\overline{<\nabla \cdot (\overline{\alpha}_{\rm p} \rho_{\rm p} \boldsymbol{\sigma}^{\rm sgs}_{\rm p})>} + \overline{<\overline{\alpha}_{\rm p} \rho_{\rm p} \mathbf{g}>} \end{aligned} \tag{5.15}$$

The above equation gives the global equilibrium between the buoyancy, particle stresses, drag, gravity contributions Figure 5.14 shows the effect of filter size on the drag and buoyancy resolved and subgrid contributions. The buoyancy resolved and subgrid contribution did not change appreciably with the filter size. As the filter size increased the resolved and unre-

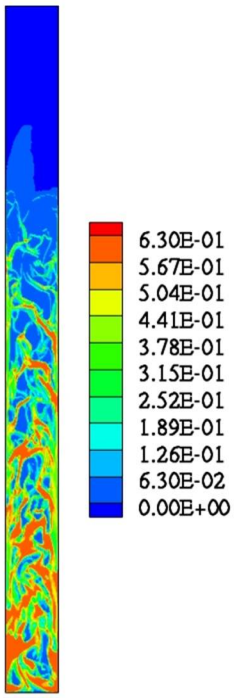

Figure 5.13 Instantaneous contours of particle volume fraction in a pilot scale reactor with grid size equal Δ_{DNS}.

solved drag contribution changed significantly. The coarse grid simulations do not account for unresolved drag and results in higher bed expansion on coarse grids.

The resolved and subgrid particle pressure and stress normalized by the gravity contribution are small compared to the drag and buoyancy contributions. The probability density funciton of particle volume fraction as shown in Figure 5.15 is sensitive to filter size. For small filter sizes, high peaks close to zero and maximum particle volume fraction are observed.

5.3.3 Drift Velocity Model

As discussed, coarse grid simulations need closure for the unresolved drag force contribution to predict correct bed expansion. A closure in the form of an effective drag coefficient ([88], [89]) is defined as

$$\overline{\frac{\alpha_{\mathrm{p}}\rho_{\mathrm{p}}}{\tau_{\mathrm{p}}}V_{r,i}} = \beta_e \tilde{W}_{r,i} \tag{5.16}$$

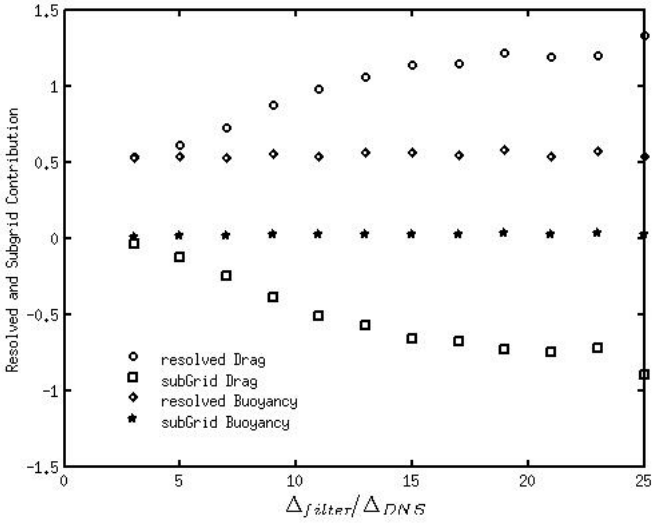

Figure 5.14 Resolved and subgrid contributions of drag and buoyancy term for different filter sizes. The results are normalized by the gravity contributions.

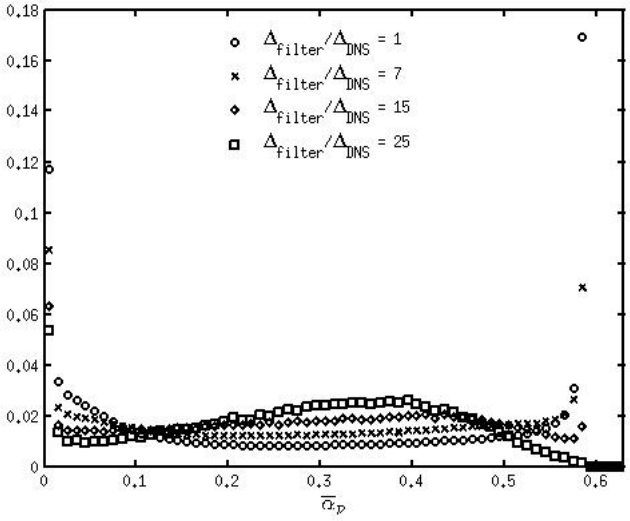

Figure 5.15 Probability density function of particle volume fraction for different filter sizes.

where $V_{r,i}$ is the relative velocity, $\tilde{W}_{r,i}$ is the resolved relative velocity. The filtered drag force is approximated

$$\overline{\frac{\alpha_{\mathrm{p}}\rho_{\mathrm{p}}}{\tau_{\mathrm{p}}}V_{r,i}} = \frac{\rho_{\mathrm{p}}}{\tilde{\tau}_{\mathrm{p}}}\overline{\alpha_{\mathrm{p}}V_{r,i}} \tag{5.17}$$

Parmentier et al [88] and Ali [89] reported that the rhs and lhs of the above equation are correlated by 99% for even large filter size. Figure 5.16 shows the computed pearson correlation coefficients of the lhs and rhs of the above equation in the refined simulations. For small filter sizes, the correlation is close to 1 and for large filter sizes the correlation is around 0.75 - 0.80.

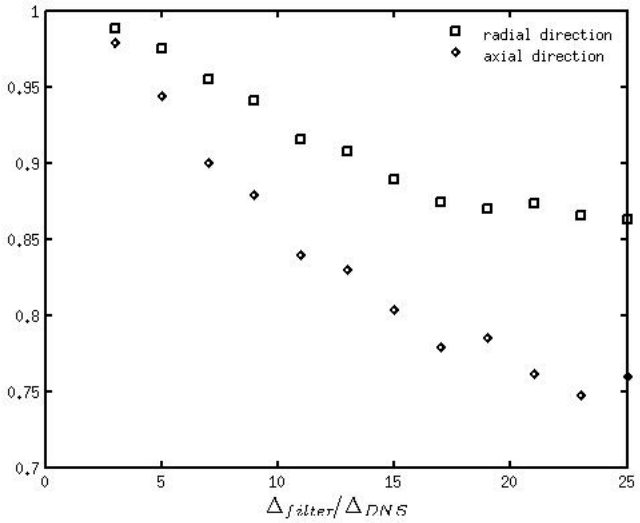

Figure 5.16 Pearson correlation coefficients.

The filtered relative velocity weighted by particle volume fraction is defined as:

$$\overline{\alpha_{\mathrm{p}}V_{r,i}} = \overline{\alpha}_{\mathrm{p}}\left(\tilde{U}_{\mathrm{p},i} - \tilde{U}_{\mathrm{g@p},i}\right) \tag{5.18}$$

where $U_{\mathrm{g@p},i} = \frac{\overline{\alpha_{\mathrm{p}}U_{\mathrm{g},i}}}{\overline{\alpha}_{\mathrm{p}}}$ The filtered drag force can be written as

$$\overline{\left(\frac{\alpha_{\mathrm{p}}\tau_{\mathrm{p}}}{\tau_{\mathrm{p}}}V_{r,i}\right)} = \overline{\alpha}_{\mathrm{p}}\left(\tilde{W}_{r,i} - \tilde{V}_{d,i}\right) \tag{5.19}$$

$\tilde{V}_{d,i}$ is known as the drift velocity and is defined as

$$\tilde{V}_{d,i} = \tilde{U}_{\mathrm{g@p},i} - \tilde{U}_{\mathrm{g},i} \tag{5.20}$$

The drift velocity is assumed to be modeled as:

$$\tilde{V}_{d,i} = -g\left(\overline{\Delta}^*, \overline{\alpha}_{\mathrm{p}}\right) K_{ij} \tilde{W}_{r,j} \tag{5.21}$$

g is a function of filtered particle volume fraction and dimensionless filter size. Refined simulation results will be used to obtain the form of g.

$$g\left(\overline{\Delta}^*, \overline{\alpha}_{\mathrm{p}}\right) = -\frac{<\tilde{V}_{d,y}|\alpha_{\mathrm{p}}>}{<\tilde{W}_{r,y}|\alpha_{\mathrm{p}}>} \tag{5.22}$$

The coefficient K_{ij} can be adjusted dynamically. From the database, the measured values of g (Figure 5.17) are shown for different filter sizes as a function of filtered particle volume fraction. The correction to drag is maximum for large filter sizes and at particle volume fractions in the range 0.15 - 0.40. The h function is obtained by dividing the g function with the area under the curve g vs α_{p}. The h function (Figure 5.18) is nearly independent of filter size for large filter sizes. g is written as

$$g\left(\overline{\Delta}^*, \overline{\alpha}_{\mathrm{p}}\right) \simeq f\left(\overline{\Delta}^*\right) h\left(\overline{\alpha}_{\mathrm{p}}\right) \tag{5.23}$$

The h function can be obtained by fitting the data

$$h(\overline{\alpha}_{\mathrm{p}}) = -tanh\left(2.0\frac{\overline{\alpha}_{\mathrm{p}}}{0.2}\right)\sqrt{\left(\frac{\overline{\alpha}_{\mathrm{p}}}{\alpha_{\mathrm{p,max}}}\right)}\left(1-\frac{\overline{\alpha}_p}{\alpha_{\mathrm{p,max}}}\right)^2 \tag{5.24}$$

$$\left(1.0 - 1.735\frac{\overline{\alpha}_p}{\alpha_{\mathrm{p,max}}} + 5.033\left(\frac{\overline{\alpha}_p}{\alpha_{\mathrm{p,max}}}\right)^2\right) \tag{5.25}$$

The dependence on the filter size, f function can be defined as

$$f(\overline{\Delta}^*) = -\frac{<\alpha_{\mathrm{p}}\tilde{V}_{d,y}>}{<\alpha_{\mathrm{p}}h(\overline{\alpha}_{\mathrm{p}})\tilde{W}_{r,y}>} \tag{5.26}$$

Figure 5.19 shows the f function from measured values and fitted model

$$f(\overline{\Delta}^*) = K_{ij}\frac{\left(\overline{\Delta}^*\right)^{1.33}}{a^2 + \left(\overline{\Delta}^*\right)^{1.33}} \tag{5.27}$$

where $\overline{\Delta}^*$ is

$$\overline{\Delta}^* = \frac{\overline{\Delta}}{\left(\tau_{\mathrm{p}}^{\mathrm{St}}\right)^2 \mathbf{g}} \tag{5.28}$$

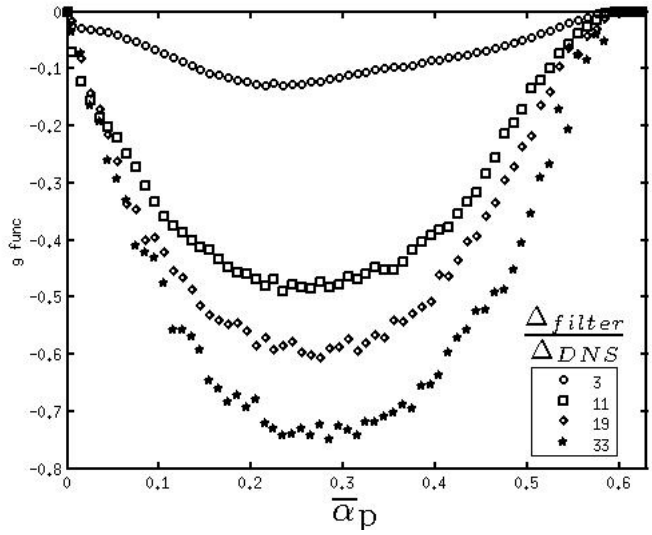

Figure 5.17 g versus filtered particle volume fraction

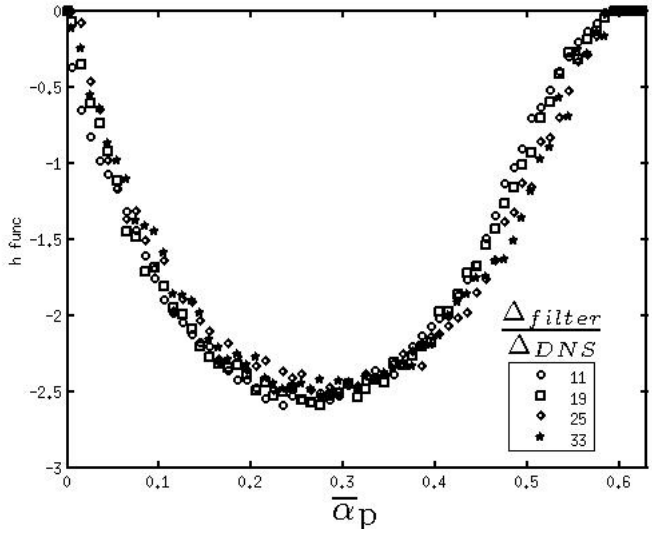

Figure 5.18 h versus filtered particle volume fraction

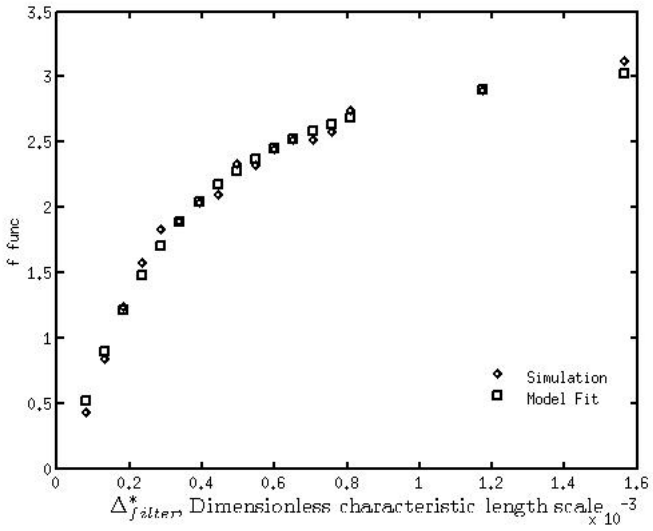

Figure 5.19 f versus dimensionless length scale of the filter

5.4 Simulation Results

The model is tested on the pilot-scale fluidized-bed and bed width of 1m, 2m, 3m and 4m. In Industrial scale reactors, the bed width is typically around 2 - 4m. The simulation parameters are shown in Table 5.5. Same parameters are used for both pilot and industrial scale system. Figure 5.20 shows the instantaneous contours of particle volume fraction on the pilot-scale fluidized-bed. Coarse grid simulation with sub-grid drag correction predicted the bed height close to the refined bed simulation. Figure 5.21 shows the instantaneous contours of dynamic correction to the drag model.

Figure 5.22 shows the instantaneous contours of particle volume fraction in 1m bed width reactor for different grid sizes. Simulation with sub grid models (Figure 5.22(g), Figure 5.22(h)) for drag correction, predicted the correct bed height. Figure 5.23 shows the bed height predictions from coarse grid with and without subgrid correction for bed width equal to 2, 3 and 4 m. Initial model predictions on the large scale reactors for different bed widths is promising. It is important to note that the model is tested for conditions similar to the refined bed simulations. The validity of the model need to be tested for different geometries, flow conditions, fluid and particle phase properties. The length scale used in this work is $\left(\tau_{\mathrm{p}}^{\mathrm{St}}\right)^2 \mathbf{g}$ is a questionable parameter. Further studies need to be performed for a general length scale model.

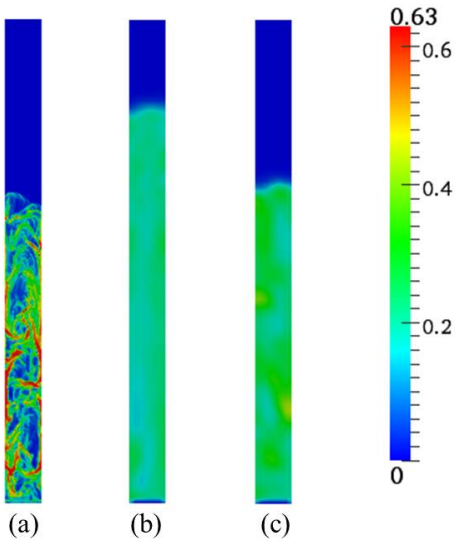

Figure 5.20 Instantaneous contours of particle volume fraction in pilot scale fluidized-bed (a) refined grid (b) coarse grid (c) coarse grid with sub-grid drag correction

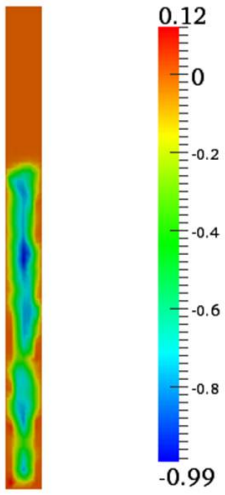

Figure 5.21 Instantaneous contours of dynamic correction (K) of pilot scale fluidized-bed

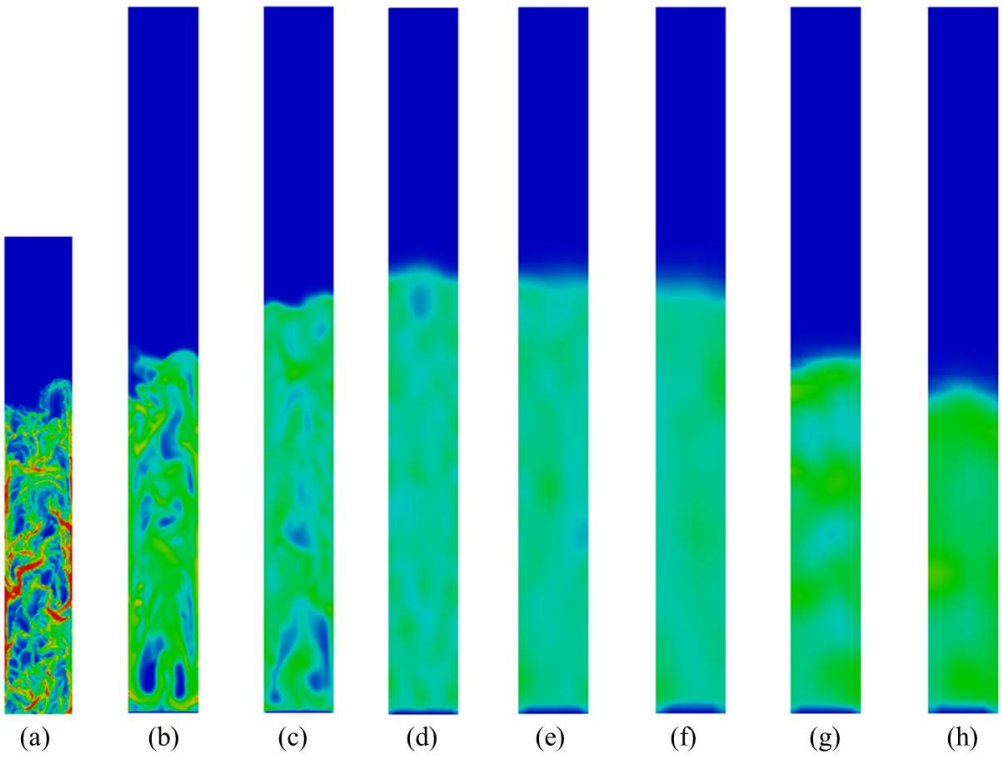

Figure 5.22 Instantaneous contours of particle volume fraction in 1m width scale fluidized-bed, grid size: (a) 1cm (b) 2.5 cm (c) 5.0 cm (d) 10 cm (e) 15 cm (f) 20 cm (g) 15 cm with sub-grid drag correction (h) 20 cm with sub-grid drag correction

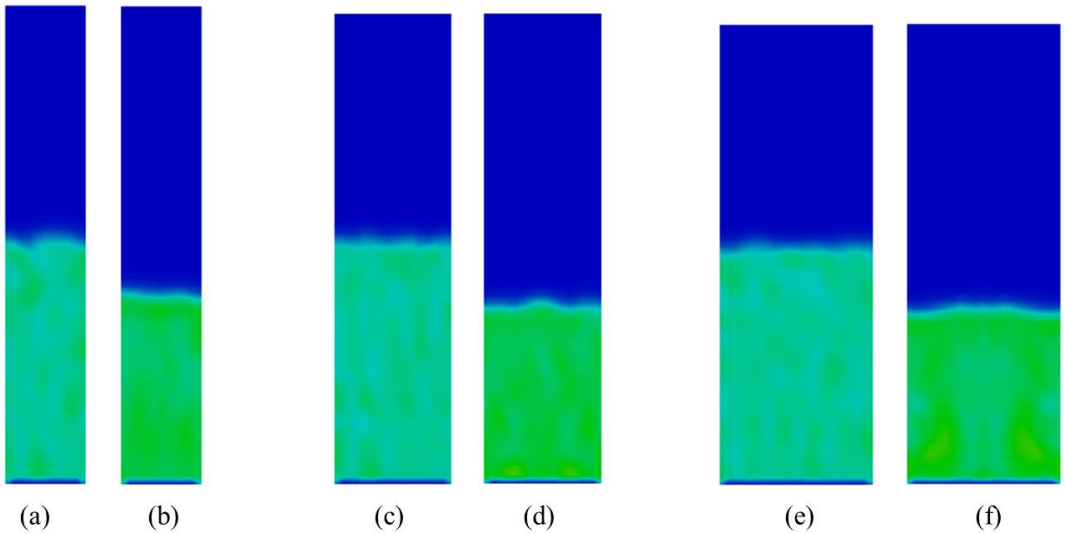

Figure 5.23 Instantaneous contours of particle volume fraction, grid size (a) 20 cm (2m width bed) (b) 20 cm with drag correction (2m width bed) (c) 20 cm (3m width bed) (d) 20 cm with sub-grid drag correction (3m width bed) (e) 20 cm (4m width) (f) 20cm with sub-grid drag correction (4m width bed)

6 AGGREGATION AND BREAKAGE IN POLYDISPERSE GAS-SOLID FLUIDIZED BEDS

6.1 Introduction

Agglomeration of particles is a serious problem in polyolefin reactors. Due to electrostatic and thermal aggregation wall sheets are formed and over a period of time. The sheets can plug the distributor plate holes and cause defluidization [1]. Exothermic reaction inside the fluidized-bed reactor can cause the polymer particle temperature to rise above its melting point. The high temperature causes the polymer to melt and is a source for agglomeration to occur. These agglomerates can stick to other particles or to the walls of the reactors and has the potential to cause defluidization, reactor fouling and finally reactor shut down [96]. There is considerable research interest on thermal/electrostatic agglomeration in olefin gas-phase fluidized-bed reactors at industrial scales. The research is focussed mainly on detecting or preventing the formation of agglomerates ([97], [98], [99]).

In polyolefin gas phase fluidized-bed reactors the catalyst size varies from 10 to 150 microns and the final polymer size ranges from 100 to 3000 microns. The fine polymer particles entrain along with the gas and the fully grown polymer particles are removed through an outlet close to the distributor. Physical and chemical processes like reaction, growth, aggregation and breakage cause the particle size distribution to vary. To account for such size variations a population balance equation (PBE) need to be solved coupled with the multi-fluid model.

There are many methods to solve the population balance equation. The direct method to solve PBE is the classes method [100] in which the internal coordinate (particle length or volume) is discretized into series of bins and large numbers of bins are required to get good results. This increases the computational time and is not feasable for large scale reactor simulations. An alternative solution is the method of moments [101], where the particle size distribution is tracked through its moments. The advantage of this method is that few number

of scalars are required to obtain reasonable results. The disadvantage is the closure problem, where the transport equations are to be represented in terms of the moments. This problem is overcome by using quadrature method of moments (QMOM). The quadrature approximation ([102], [103]) can be determined from the lower order moments by using the product difference algorithm [104]. The main limitation of QMOM is that a phase average velocity of the solid phases is used to solve the transport equations for the moments. To address these problems, direct quadrature method of moments (DQMOM) is developed [105] and it solves the transport equations for the weights and absicssas without resorting to the PD algorithm in QMOM.

Recent studies show that DQMOM is applied in the area of modeling of sprays, bubble column reactors, fluidized-beds and has found to be accurate and computationally efficient. Marchisio and Fox [105] formulated, validated and tested the DQMOM. DQMOM results are compared with QMOM for the monovariate case and applied for different cases such as homogenous growth, dispersion, nucleation, aggregation and breakage. They also implemented DQMOM for bivariate applications like homogenous aggregation and inhomogenous growth. Fox [106] applied the DQMOM on a bivariate population balance equation for coagulation and sintering particles. Silva et al [107] analyzed the different quadrature based methods for solving the PBE. From their work, they found that parallel parent and daughter classes (PPDC) has poor convergence and QMOM, DQMOM had similar accuracy, but the DQMOM was the most efficient. Silva et al [108] implemented DQMOM in ANSYS CFX and OpenFOAM®. They simulated cases with dominant aggregation, dominant breakage and invariant solution and validated against an analytical solution. Selma et al [109] compared the classes method and DQMOM in the simulation of bubbly flows in open source Open-Foam. They found that 25 classes are required to obtain good results and DQMOM was more computationally efficient. In this work the DQMOM with new aggregation and breakage kernels is used to study evolution of particle size distribution in gas-particle fluidized-bed reactors. The DQMOM is efficient and simple when applied to mutli-variate distributions and physically represents the strong coupling between the internal coordinates and the phase velocities. Th chapter discusses the theory on DQMOM, source terms for aggregation and breakage. The numerical implementation and coupling between DQMOM and multi-fluid model will also be presented.

6.2 DQMOM - Multi Fluid Model

The description of the multi-fluid model is given in Chapter 2 and will not be repeated here. The multi-fluid model is a continuum based model and solves for one gas phase and N solid phases. In this section the direct quadrature method of moments and the coupling with the multi-fluid model will be presented.

6.2.1 Direct Quadrature Method of Moments

A polydisperse solid phase can be modeled by a transport equation for the mutlivariate distribution function $n(L, \mathbf{u}_\mathrm{s}; \mathbf{x}, t)$

$$\frac{\partial}{\partial t} n\left(L, \mathbf{u}_\mathrm{s}; \mathbf{x}, t\right) + \nabla \cdot \left[\mathbf{u}_\mathrm{s} n(L, \mathbf{u}_\mathrm{s}; \mathbf{x}, t)\right] + \nabla_{\mathbf{u}_\mathrm{s}} \cdot \left[\mathbf{F} n\left(L, \mathbf{u}_\mathrm{s}; \mathbf{x}, t\right)\right] = S\left(L, \mathbf{u}_\mathrm{s}; \mathbf{x}, t\right) \tag{6.1}$$

where L is the characteristic particle size, $\mathbf{u}_\mathrm{s}$ is the particle velocity vector, S is the source term due to reaction, aggregation and breakage. Using DQMOM the distribution function can be approximated by a summation of N Dirac delta functions:

$$n(L, \mathbf{u}_\mathrm{s}; \mathbf{x}, t) = \sum_{\alpha=1}^{N} \omega_\alpha\left(\mathbf{x}, t\right) \delta\left[L - L_\alpha\left(\mathbf{x}, t\right)\right] \delta\left[\mathbf{u}_\mathrm{s} - \mathbf{u}_{\mathrm{s}\alpha}\left(\mathbf{x}, t\right)\right] \tag{6.2}$$

where ω_α is the weight of the delta function centered at the characteristic particle size L_α and the characteristic velocity $\mathbf{u}_{\mathrm{s}\alpha}$. If Eq. (6.2) is inserted into Eq. (6.1), and a moment transformation applied to derive the transport equations for the N weights ω_α and absicssas L_α. Integrating out the velocity in Eq. (6.1) we obtain the solid phase PBE:

$$\frac{\partial}{\partial t} n\left(L; \mathbf{x}, t\right) + \nabla \cdot \left[\langle \mathbf{u}_\mathrm{s} | L \rangle\, n(L; \mathbf{x}, t)\right] = S\left(L; \mathbf{x}, t\right) \tag{6.3}$$

where $\langle \mathbf{u}_\mathrm{s} | L \rangle$ is the mean velocity conditioned on L. The derivation of the transport equations for the weigths ω_α and weighted absicissas $L_\alpha \omega_\alpha$ are reported in [105]

$$\frac{\partial}{\partial t}\left(\omega_\alpha\right) + \nabla \cdot \left(\mathbf{u}_{\mathrm{s}\alpha} \omega_\alpha\right) = a_\alpha \tag{6.4}$$

$$\frac{\partial}{\partial t}\left(L_\alpha \omega_\alpha\right) + \nabla \cdot \left(\mathbf{u}_{\mathrm{s}\alpha} L_\alpha \omega_\alpha\right) = b_\alpha \tag{6.5}$$

where a_α and b_α are defined through a linear system found from the first $2N$ moments of the PSD.The linear system can be written in matrix form as:

$$\mathbf{A}\alpha = \mathbf{d} \tag{6.6}$$

where the $2N$ coefficient matrix $\mathbf{A} = [\mathbf{A}_1 \mathbf{A}_2]$ is defined by

$$\mathbf{A}_1 = \begin{bmatrix} 1 & \dots & 1 \\ 0 & \dots & 0 \\ -L_1^2 & \dots & -L_N^2 \\ \vdots & \ddots & \vdots \\ 2\left(1-N\right) L_1^{2N-1} & \dots & 2\left(1-N\right) L_N^{2N-1} \end{bmatrix} \tag{6.7}$$

$$\mathbf{A}_2 = \begin{bmatrix} 0 & \dots & 0 \\ 1 & \dots & 1 \\ 2L_1 & \dots & 2L_N \\ \vdots & \ddots & \vdots \\ 2\left(N-1\right) L_1^{2N-2} & \dots & 2\left(N-1\right) L_N^{2N-2} \end{bmatrix} \tag{6.8}$$

The $2N$ vector of unknowns α is defined by

$$\alpha = [a_1 ... a_N b_1 ... b_N]^{\mathrm{T}} = \begin{bmatrix} \mathbf{a} \\ \mathbf{b} \end{bmatrix} \tag{6.9}$$

and the known right hand side

$$\mathbf{d} = \left[\bar{S}_0^N ... \bar{S}_{2N-1}^N\right]^{\mathrm{T}} \tag{6.10}$$

The source term for the k^{th} moment $\bar{S}_k^N$

$$\bar{S}_{\mathbf{x},t}^N = \int_0^\infty L^k S(L;\mathbf{x},t) dL \tag{6.11}$$

The source terms for the transport equation for the abcissas and weighted abcissas can be found by inverting $\mathbf{A}$

$$\alpha = \mathbf{A}^{-1}\mathbf{d} \tag{6.12}$$

In order to be consistent with variables used in multi-fluid model, the weights and abcissas are related to the volume fraction of the solid phase by

$$\varepsilon_{\mathrm{s}\alpha} = k_{\mathrm{v}} L_\alpha^3 \omega_\alpha \tag{6.13}$$

where k_{v}. The transport equation for the $\varepsilon_{\mathrm{s}\alpha}$ and $L_{\mathrm{s}\alpha}$

$$\frac{\partial}{\partial t}\left(\varepsilon_{\mathrm{s}\alpha}\rho_{\mathrm{s}\alpha}\right) + \nabla\cdot\left(\varepsilon_{\mathrm{s}\alpha}\rho_{\mathrm{s}\alpha}\mathbf{u}_{\mathrm{s}\alpha}\right) = 3k_{\mathrm{v}}\rho_{\mathrm{s}\alpha}L_\alpha^2 b_\alpha - 2k_{\mathrm{v}}\rho_{\mathrm{s}\alpha}L_\alpha^3 a_\alpha \tag{6.14}$$

$$\frac{\partial}{\partial t}(\varepsilon_{s\alpha} L_\alpha \rho_{s\alpha}) + \nabla \cdot (\varepsilon_{s\alpha} L_\alpha \rho_{s\alpha} \mathbf{u}_{s\alpha}) = 3 k_v \rho_{s\alpha} L_\alpha^3 b_\alpha - 2 k_v \rho_{s\alpha} L_\alpha^4 a_\alpha \tag{6.15}$$

Eq. (6.14) and Eq. (6.15) is the continuity equation and scalar transport equation for the solid phase in the presence of aggregation and breakage.

6.3 Implementation of Aggregation and Breakage

In this work, particle size evolution is only due to aggregation and breakage. The growth of the particle is neglected. The moment transform of the aggregation and breakage source term is

$$\bar{S}_k^N(\mathbf{x}, t) = \bar{B}_k^a(\mathbf{x}, t) - \bar{D}_k^a(\mathbf{x}, t) + \bar{B}_k^b(\mathbf{x}, t) - \bar{D}_k^b(\mathbf{x}, t) \tag{6.16}$$

where the moments of the birth and death rates are defined by

$$\bar{B}_k^a(\mathbf{x}, t) = \frac{1}{2} \int_0^\infty \int_0^\infty \beta(L, \lambda) (L^3 + \lambda^3)^{k/3} n(\lambda; \mathbf{x}, t) n(\lambda; \mathbf{x}, t) d\lambda dL \tag{6.17}$$

$$\bar{D}_k^a(\mathbf{x}, t) = \int_0^\infty \int_0^\infty L^k \beta(L, \lambda) n(\lambda; \mathbf{x}, t) n(\lambda; \mathbf{x}, t) d\lambda dL \tag{6.18}$$

$$\bar{B}_k^b(\mathbf{x}, t) = \int_0^\infty \int_0^\infty L^k a(\lambda) b(L|\lambda) n(\lambda; \mathbf{x}, t) d\lambda dL \tag{6.19}$$

$$\bar{D}_k^b(\mathbf{x}, t) = \int_0^\infty L^k a(L) n(L; \mathbf{x}, t) dL \tag{6.20}$$

where $\bar{B}_k^a(\mathbf{x}, t)$, $\bar{D}_k^a(\mathbf{x}, t)$ birth and death due to aggregation, $\bar{B}_k^b(\mathbf{x}, t)$, $\bar{D}_k^b(\mathbf{x}, t)$ birth and death due to breakage. In these expressions, $\beta(L, \gamma)$ is the aggregation kernel, which is proportional to the frequency of collision of two particles with length L and γ, $a(L)$ is the breakage kernel, which is the frequency of disruption of a particle of lenght L, and $b(L|\gamma)$ is the fragment distribution function, which contains information on the fragments produced by a breakage event. Using the DQMOM approximation the source term in Eq. (6.16) is closed:

$$\bar{S}_k^N(\mathbf{x}, t) = \frac{1}{2} \sum_{\alpha=1}^N \sum_{\gamma=1}^N \omega_\alpha \omega_\gamma (L_\alpha^3 + L_\gamma^3)^{k/3} \beta_{\alpha\gamma} - \sum_{\alpha=1}^N \sum_{\gamma=1}^N \omega_\alpha \omega_\gamma L_\alpha^k \beta_{\alpha\gamma} + \sum_{\alpha=1}^N \omega_\alpha a_\alpha^* \bar{b}_\alpha^k \tag{6.21}$$

where $\beta_{\alpha\gamma} = \beta(L_\alpha, L_\gamma)$, $a_\alpha^* = a(L_\alpha)$ and

$$\bar{b}_\alpha^k = \int_0^\infty L^k b(L|L_\alpha) dL \tag{6.22}$$

The information on daughter distribution function is given below

$$\bar{b}_{\alpha}^{k} = L_{\alpha}^{k} \frac{m^{k/3} + n^{k/3}}{(m+n)^{k/3}} \tag{6.23}$$

where m and n represent the mass ratios between the two fragments. In this work the two fragments have same volume and thus symmetric fragmentation is considered

6.3.1 Aggregation and Breakage Kernels

Fan and Fox [110] used aggregation and breakage kernels based on particle-particle collision frequency. The model used in [110] are described here. The collision frequency is given by

$$N_{\alpha\gamma} = \pi \omega_{\alpha} \omega_{\gamma} \sigma_{\alpha\gamma}^{3} g_{\alpha\gamma} \left(\frac{4}{\sigma_{\alpha\gamma}} \left(\frac{\Theta_{\mathrm{s}}}{\pi} \frac{m_{\alpha} + m_{\gamma}}{2 m_{\alpha} m_{\gamma}} \right)^{1/2} - \frac{2}{3} \nabla \cdot \mathbf{u}_{\mathrm{s}} \right) \tag{6.24}$$

where m_{α} and m_{γ} are the masses of the α^{th} and γ^{th} particle phase. Θ_{s} is the mixture granular temperature. Divergence term is ignored in their work. The model accounts for collisions when the mixture granular temperature is non zero and does not account for collisions when there is a mean velocity difference between the different particle species. The kinetic theory of granular flow (KTGF) can be applied to derive the expressions for new aggregation and breakage kernels based on collision frequency. According to KTGF the number of collisions per unit volume and time between particles with indices α and γ is given by:

$$N_{\alpha\gamma} = \int_{S+} \int_{R^3} \int_{R^3} f^2 \left(\mathbf{g}_{12} \cdot \mathbf{n} \right) \sigma_{\alpha\gamma}^{2} d\mathbf{n} d\mathbf{u}_{\alpha} d\mathbf{u}_{\gamma} \tag{6.25}$$

where $\sigma_{\alpha\gamma}$ is the distance between the particles at the time of collision, The integrals can be evaluated by assuming a form for the pair distribution function $f^{(2)}$. Using the Enskog approximation the pair distribution function is approixmated by a product of single distribution function and a correction function $g_{\alpha\gamma}$, the radial distribution function [38]. The final form of the $N_{\alpha\gamma}$ is

$$N_{\alpha\gamma} = C \pi g_{\alpha\gamma} \sigma_{\alpha\gamma}^{2} \omega_{\alpha} \omega_{\gamma} \left(3\Theta_{\alpha} + 3\Theta_{\gamma} + |\mathbf{u}_{\mathrm{s}\alpha} - \mathbf{u}_{\mathrm{s}\gamma}|^2 \right)^{1/2} \tag{6.26}$$

The aggregation kernel can be expressed as:

$$\beta_{\alpha\gamma} = C \psi_{a} \pi g_{\alpha\gamma} \sigma_{\alpha\gamma}^{2} \left(3\Theta_{\alpha} + 3\Theta_{\gamma} + |\mathbf{u}_{\mathrm{s}\alpha} - \mathbf{u}_{\mathrm{s}\gamma}|^2 \right)^{1/2} \tag{6.27}$$

where ψ_a is the success-factor for aggregation and is a function of particle temperature, particle velocity and particle position. The breakage kernel is expressed as

$$a^*_\alpha = \psi_b \sum_{\alpha=1}^{N} \frac{N_{\alpha\gamma}}{\omega_\alpha} \tag{6.28}$$

6.4 Solution Technique

The algorithm for implementing and coupling of DQMOM and multi-fluid model is described in the following steps.

1. With known solid phase volume fraction and size the weights ω_α can be obtained from Eq. (6.13).

2. The source terms due to aggregation and breakage are related to the weights and abcissas shown in Eq. (6.16) are computed.

3. The source terms for the transport equation of abscissas and weighted abcissas are obtained from Eq. (6.6).

4. The source terms for the solid phase continuity and scalar transport equations is calculated. The solution of the transport equations is done by a time-splitting scheme.

5. The volume fractions and particles sizes obtained above is used to compute the weights in step 1 for the next time step.

The source terms in the solid phase continuity and scalar equations is stiff and need to be decoupled from the multi-fluid CFD model. A time splitting technique is used and this requires two steps. In the first fractional step, the continuity and scalar transport equation for the solid phase size are solved without the source term. In the next fractional time step the change due to source terms is computed as shown below.

$$\frac{d}{dt}(\varepsilon_{s\alpha}\rho_{s\alpha}) = 3k_v\rho_{s\alpha}L^2_\alpha b_\alpha - 2k_v\rho_{s\alpha}L^3_\alpha a_\alpha \tag{6.29}$$

$$\frac{d}{dt}(\varepsilon_{s\alpha}\rho_{s\alpha}L_{s\alpha}) = 4k_v\rho_{s\alpha}L^3_\alpha b_\alpha - 3k_v\rho_{s\alpha}L^4_\alpha a_\alpha \tag{6.30}$$

A new solid-solid drag closure is used in this work

$$C_{\alpha\gamma} = \frac{2}{5} c_0 (1+e) \frac{(d_\alpha + d_\gamma)^2}{\rho_\alpha d_\alpha^3 + \rho_\gamma d_\gamma^3} \varepsilon_\alpha \rho_\alpha \varepsilon_\gamma \rho_\gamma g_{0,\alpha\gamma} E_{\alpha\gamma}^{1/2} (\mathbf{u}_{s\alpha} - \mathbf{u}_{s\gamma}) \tag{6.31}$$

where $E_{\alpha\gamma} = \left(3\Theta_\alpha + 3\Theta_\gamma + |\mathbf{u}_{s\alpha} - \mathbf{u}_{s\gamma}|^2\right)$ is known as the energy scaling factor.

6.5 Simulation Results

The new aggregation kernels are implemented in the MFIX DQMOM solver. MFIX is an open source granular multiphase code developed by Department of Energy, USA. The continuum based two-fluid model uses a finite volume method with auto time stepping method to speed up the calculation. CFD multi-fluid simulations are done on two-dimensional fluidized-bed reactor. The simulation conditions are same as described in Fan and Fox [110] and shown in Table 6.1. Initital particle size and particle volume fraction (Table 6.2) are found using the moments of the initial particle size distribution and product difference algorithm. Two cases are run with aggregation dominant and a breakage dominant. The aggregation and breakage success factors are used to control the dominance of aggregation or breakage events. In this work, constant aggregation and breakage success factors are used, but in realistic conditions, they are a function of particle properties such as velocity, diameter. For each case, the particle size distribution is represented by two and three nodes.

Table 6.1 Simulation conditions

Width, cm	10.1
Height, cm	50.0
Particle Properties	
Particle density, kg/m^3	2530
Coefficient of restitution	0.8
Packed bed void fraction	0.38

Figure 6.1 and 6.2 shows the evolution of moments of the particle size distribution for the two cases. Each of the moments have physical meaning, the zeroth order moment is the total number density. Second order moments represents the total particle area and the third

Table 6.2 Initial values of particle diameter and solid-phase volume fractions for Nodes $N = 2$ and 3 for the same initial PSD

	N	$\alpha = 1$	$\alpha = 2$	$\alpha = 3$
Particle diameter, μm	2	183	356	
	3	174	263	409
Particle volume fraction	2	0.274	0.356	
	3	0.196	0.229	0.205

order moments indicates the total particle volume. In aggregation dominant case, the zeroth, first and second order moment decrease as a function of time. As particles aggregate, the number density decreases and bigger particles are formed. The particles continue to aggregate till a defluidization condition has reached. In this condition, the particle species granular temperatures and the mean particle species velocity difference is zero. For breakage dominated case, the zeroth, first and second order normalized moments increase with time. As particles break, the number density increases and results in the formation of smaller particles. As process continues, small particles are formed and this increases elutriation. The third order moments remains constat, as the total particle volume does not change with aggregation or breakage dominant cases

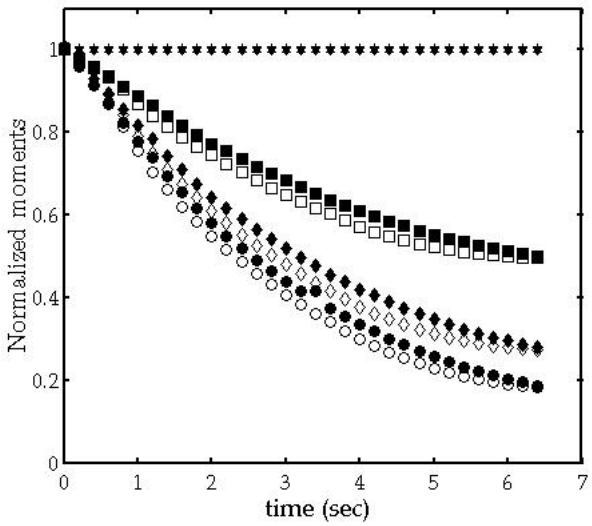

Figure 6.1 Moments of the particle size distribution in aggregation dominant case. open symbols: 2 Nodes, closed symbols: 3 Nodes: circle - Zero order moment, diamond - First order moment, square - Second order moment, star - Third order moment

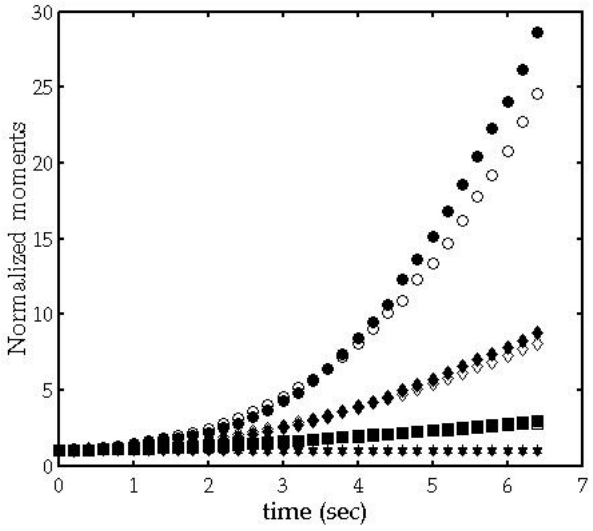

Figure 6.2 Moments of the particle size distribution in breakage dominant case. open symbols: 2 Nodes, closed symbols: 3 Nodes: circle - Zero order moment, diamond - First order moment, square - Second order moment, star - Third order moment

Figure 6.3 and 6.4 shows the volume average mean diameter for the aggregation and breakage case. The mean particle diameter is computed as the ration of third to second order moment. The mean particle size for the aggregation case increases and for the breakage case decreases with time. For a given flow time, the mean particle size with the new aggregation kernel is bigger than the kernels described in Fan and Fox [110]. The reason is due to increase of collision frequency due to species velocity difference term in the new kernels.

Figure 6.5 and 6.6 shows the evolution of particle size distribution with time. For aggregation dominated process the mean particle size increases and bigger particles move towards the distributor and the smaller particles segregate to the upper section of the bed. As particles aggregate, the particle volume fraction tends to the packing limit and this process leads to defluidization. For breakage dominated process, the mean particle size decreases, smaller particles are produced and elutriated.

The results presented in this work are consistent with the conclusions of Fan and Fox [110]. New aggregation and breakage kernels are developed and implemented in MFIX code. The success factors are assumed to be constant, but for real applications and model validation, the success factors need to be developed

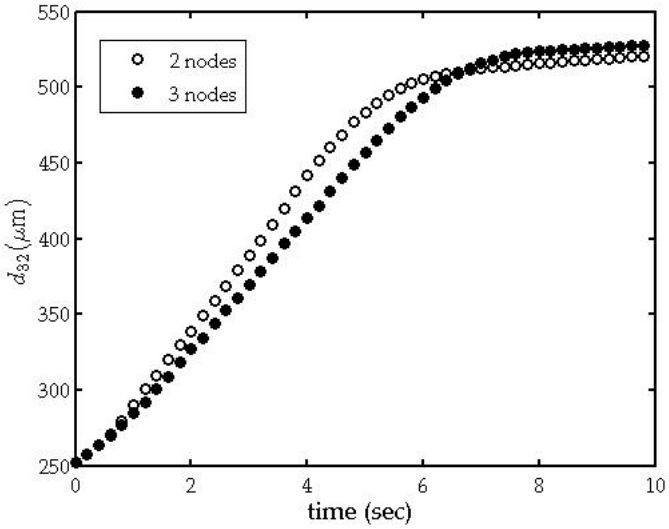

Figure 6.3 Volume average mean diameter in aggregation dominant case

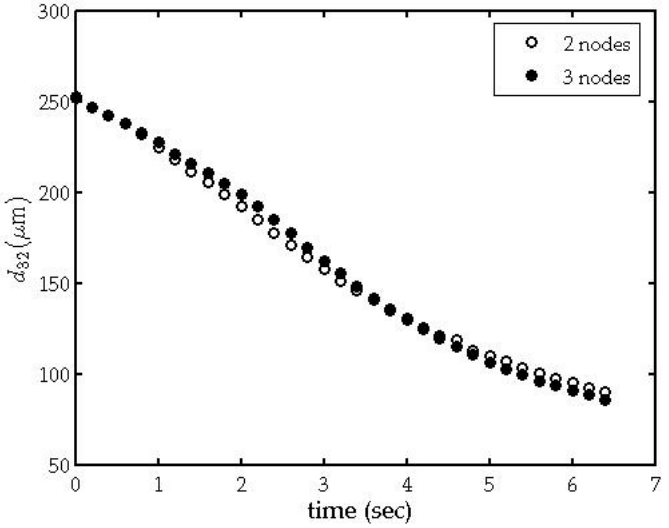

Figure 6.4 Volume average mean diameter in breakage dominant case

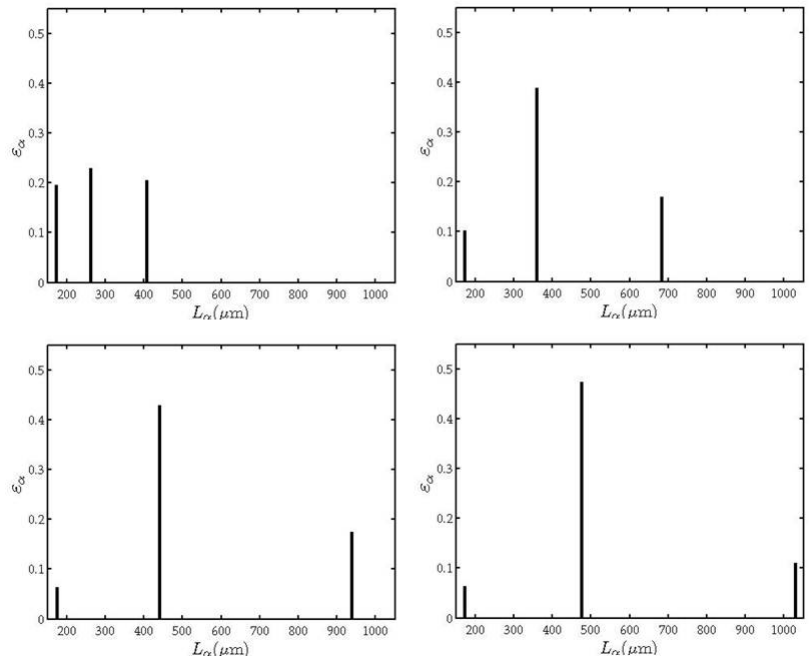

Figure 6.5 Evolution of PSD at different flow times in aggregation dominant case

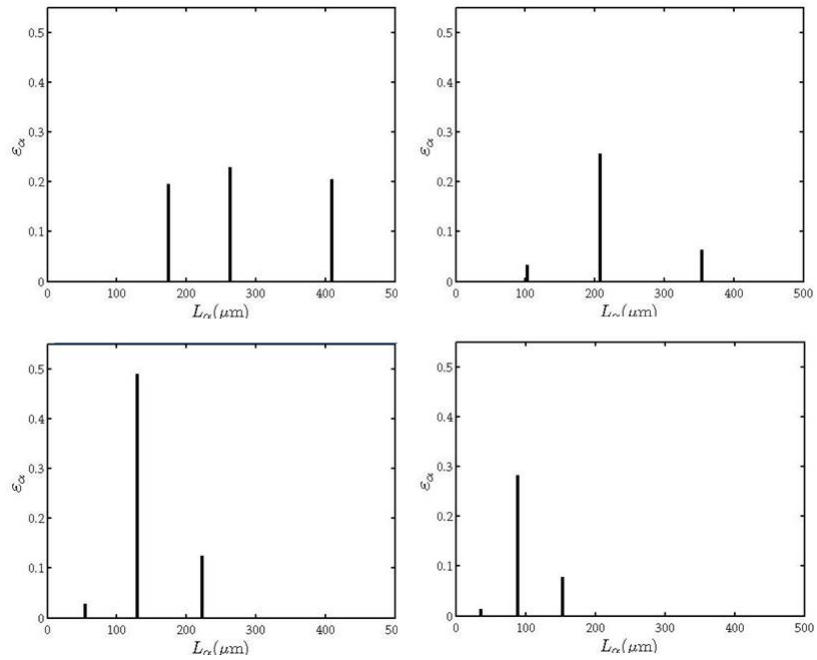

Figure 6.6 Evolution of PSD at different flow times in breakage dominant case

7 CONCLUSIONS AND FUTURE WORK

Electrostatics are known to influence the hydrodynamics of gas-particle fluidized-bed reactors. The motion of charged particles in a reactive environment such as polymerization fluidized-bed reactors could lead to sheet formation and thereby process upsets. An understanding of the process, such as the effect of electrostatics in polymerization reactors would help in control process upsets. The chapter outlines the work done in the thesis and directions for future work.

An electrostatic model from first principles based on Gauss's law is developed. The model predictions are compared with simulation results on two simple test cases. In the first case, the poisson solver in ANSYS FLUENT is compared with MATLAB predictions. In the second case the electrostatic model is coupled with multi-fluid computational fluid dynamic model. The model predicted the basic phenomena such as like charged particles repel and unlike charged particles attract. This case is performed in the absence of other forces like gravity and the different phases are initialized to zero velocity. Next, the model predictions were compared with experimental measurements and observations. The model predictions were in reasonable agreement with experimental results such as bed height, fluidization flow regimes, segregation pattern and quantitative measurements of WALL particles.

In the next step, the model (Euler-Euler CFD multiphase model coupled with electrostatic model) is applied on an existing pilot scale polymerization fluidized-bed reactor. A catalyst size distribution (specific catalyst for poly ethylene polymerization) is represented in three particle classes using quadrature method of moments. Using a reaction engineering model, the final polymer size is predicted. The simulations were run with the predicted final polymer size. A size dependent particle charge from the experiments was used in the simulations. Three different cases were run to understand the effect of charges on the dynamics of the fluidized-bed system. Particle segregation is shown to be dependent on the magnitude and polarity of

charge. The sheet formation (wall and dome sheeting) in the reactors is shown to be dependent upon the polarity of catalyst. This behavior is well predicted in the simulations. Electrostatics were also shown to have effect on entrainment of catalyst and polymer particles. Process upsets such as defluidization were known to occur at high particle charge conditions. The catalyst phase distribution inside the fluidized-bed is strongly dependent on the mean bed charge and the polarity of the catalsyt.

There are few drawbacks in the current electrostatic model. Electrostatic simulations are performed with constant particle charge conditions. In other words, after several collisions the particles have reached an equilibrium charge and the simulations are run at these steady state conditions. For a more advanced model, a transport equation for the conservation of charge need to be solved to account for changes in particle charge. To solve the transport equation closure models for charge generation and dissipation are required.

In the previous step, the simulations were run on a pilot scale reactor. It is important to know the fluidization and electrostatic behavior on an industrial scale reactor where poly ethylene is commercially produced. The CFD models used on the pilot scale are also applicable on large scale reactors. The simulations on large scale reactors are computationally expensive and is the objective to develop filtered models. In this work a filtered model based on the formulation as described in Parmentier et al [88] and Ali [89] is developed. A refined two-fluid simulation of Geldart B type particles on a pilot scale reactor is done. From the refined simulation database, closures for the filtered drag model are obtained. The correction for the drag is written in terms of the filtered particle volume fraction and grid size used in the simulations. Preliminary simulations with the developed closure models yielded promising results. Further tests on different geometries, flow regimes and particle properties need to be performed to test the validity of the derived closures. Subgrid closures need to be derived for the electrostatic model to simulate the hydrodynamics of charged particles on large scale reactors with coarse grids.

In Chapter 6, the Direct Quadrature Method of Moments with new aggregation kernels is used to run polydisperse gas-particle fluidized-bed simulations. The kernels are assumed to be a function of the particle collision frequency. The new kernels account for relative velocity

difference between the particle species and increases the collision frequency as compared to kernels described in Fan and Fox [110]. For industrial applications, closure forms for the success factors need to be derived

Bibliography

[1] G. Hendrickson. Electrostatics and gas phase fluidized bed polymerization reactor wall sheeting. *Chemical Engineering Science*, 61(4):1041 – 1064, 2006.

[2] Andrew Sowinski, Leigh Miller, and Poupak Mehrani. Investigation of electrostatic charge distribution in gas-solid fluidized beds. *Chemical Engineering Science*, 65(9):2771 – 2781, 2010.

[3] Y. Kaneko, T. Shiojima, and M. Horio. Dem simulation of fluidized beds for gas-phase olefin polymerization. *Chemical Engineering Science*, 54(24):5809 – 5821, 1999.

[4] T. Xie, K. B. McAuley, J. C. C. Hsu, and J. W. Bacon. Gas phase ethylene polymerization: Production processes, polymer properties, and reactor modeling. *Industrial and Engineering Chemistry Research*, 33:449 – 479, 1994.

[5] G. A. Bokkers, M. van Sint Annaland, and J. A. M. Kuipers. Mixing and segregation in a bidisperse gas-solid fluidised bed: a numerical and experimental study. *Powder Technology*, 140(3):176 – 186, 2004. 1st International Workshop on Granulation.

[6] R. Fan. Computational fluid dynamics simulation of fluidized bed polymerization reactors. *Unpublished doctoral dissertation, Iowa State University*, 2006.

[7] R. Fan and R. O. Fox. Segregation in polydisperse fluidized beds: Validation of a multi-fluid model. *Chemical Engineering Science*, 63(1):272 – 285, 2008.

[8] J. Y. Kim and K. Y. Choi. Modeling of particle segregation phenomena in a gas phase fluidized bed olefin polymerization reactor. *Chemical Engineering Science*, 56(13):4069 – 4083, 2001.

[9] F. A. Mahdi, A. S. Dudley, and S. Sundaresan. The effect of static electrification on gas-solid flows in vertical risers. *Industrial and Engineering Chemistry Research*, 41(25):6224 – 6234, 2002.

[10] M. Baerns. Effect of interparticle adhesive forces on fluidization of fine particles. *Industrial and Engineering Chemistry Fundamentals*, 5(4):508 – 516, 1966.

[11] T. Baron, C. L. Briens, M. A. Bergougnou, and J. D. Hazlett. Electrostatic effects on entrainment from a fluidized bed. *Powder Technology*, 53(1):55 – 67, 1987.

[12] C. L. Briens, M. A. Bergougnou, I. I. Inculet, T. Baron, and J. D. Hazlett. Size distribution of particles entrained from fluidized beds: Electrostatic effects. *Powder Technology*, 70(1):57 – 62, 1992.

[13] M. Bafrnec and J. Bena. Quantitative data on the lowering of electrostatic charge in a fluidized bed. *Chemical Engineering Science*, 27(5):1177 – 1181, 1972.

[14] D. Boland and D. Geldart. Electrostatic charging in gas fluidised beds. *Powder Technology*, 5(5):289 – 297, 1972.

[15] J. Ciborowski and A. Wlodarski. On electrostatic effects in fluidized beds. *Chemical Engineering Science*, 17(1):23 – 32, 1962.

[16] J. Guardiola, V. Rojo, and G. Ramos. Influence of particle size, fluidization velocity and relative humidity on fluidized bed electrostatics. *Journal of Electrostatics*, 37(1-2):1 – 20, 1996.

[17] P. Mehrani, H. T. Bi, and J. R. Grace. Electrostatic charge generation in gas-solid fluidized beds. *Journal of Electrostatics*, 63(2):165 – 173, 2005.

[18] P. Mehrani, H. T. Bi, and J. R. Grace. Electrostatic behavior of different fines added to a faraday cup fluidized bed. *Journal of Electrostatics*, 65(1):1 – 10, 2007.

[19] R. Elsdon and F. R. G. Mitchell. Contact electrification of polymers. *Journal of Physics D: Applied Physics*, 9:1345 – 1460, 1976.

[20] A. Gajewski. Investigation of the electrification of polypropylene particles during the fluidization process. *Journal of Electrostatics*, 17(3):289 – 298, 1985.

[21] J. R. Mountain, M. K. Mazumder, R. A. Sims, D. L. Wankum, T. Chasser, and P. H. Pettit Jr. Triboelectric charging of polymer powders in fluidization and transport processes. *IEEE Transactions on Industrial Applications*, 37(3):778 – 784, 2001.

[22] J. Revel, C. Gatumel, J. A. Dodds, and J. Taillet. Generation of static electricity during fluidisation of polyethylene and its elimination by air ionisation. *Powder Technology*, 135-136:192 – 200, 2003. Electrostatic Phenomena in Particulate Processes.

[23] A. Wolny and W. Kazmierczak. Triboelectrification in fluidized bed of polystyrene. *Chemical Engineering Science*, 44(11):2607 – 2610, 1989.

[24] H. Zhao, G. S. P. Castle, I. I. Inculet, and A. G. Bailey. Bipolar charging in polydisperse polymer powders in industrial processes. *Proceedings of the IEEE-IAS Annual Meeting*, 33:835 – 841, 2000.

[25] Y. Behjat, M. A. Dehnavi, S. Shahhosseini, and S. H. Hashemabadi. Heat transfer of polymer particles in gas phase polymerization reactors. *International Journal of Chemical Reactor Engineering*, 6(A81):508 – 516, 2008.

[26] T. F. McKenna and J. B. P. Soares. Single particle modelling for olefin polymerization on supported catalysts: A review and proposals for future developments. *Chemical Engineering Science*, 56(13):3931 – 3949, 2001.

[27] T. F. McKenna, R. Spitz, and D. Cokljat. Heat transfer from catalysts with computational fluid dynamics. *AICHE Journal*, 45:2392 – 2410, 1999.

[28] H. Song. Polymerization in expanding catalyst particles. *Doctoral dissertation-University of Houston*, 2004.

[29] H. Song and D. Luss. Bounds on operating conditions leading to melting during olefin polymerization. *Industrial and Engineering Chemistry Research*, 43:270–282, 2004.

[30] A. M. Dehnavi, S. Shahhosseini, S. H. Hashemabadi, S. M. Ghafelebashi, J. A. Debling, and W. H. Ray. Cfd based evaluation of polymer particles heat transfer coefficient in gas phase polymerization reactors. *International Communications in Heat and Mass Transfer*, 35:1375 – 1379, 2008.

[31] E. J. G. Eriksson and T. F. Mckenna. Heat transfer phenomena in gas olefin polymerization using computational fluid dynamics. *Industrial and Engineering Chemistry Research*, 43(23):7251 – 7260, 2004.

[32] A. Gobin, H. Neau, O. Simonin, J. R. Llinas, V. Reiling, and J. L. Seilo. Fluid dynamic numerical simulation of a gas phase polymerization reactor. *International Journal for Numerical Methods in Fluid Dynamics*, 43:1199 – 1220, 2003.

[33] L. R. Glicksman. Scaling relationships for fluidized beds. *Chemical Engineering Science*, 43(6):1419 – 1421, 1988.

[34] Y. Tsuji, T. Kawaguchi, and T. Tanaka. Discrete particle simulation of two-dimensional fluidized bed. *Powder Technology*, 77(1):79 – 87, 1993.

[35] B. P. B. Hoomans, J. A. M. Kuipers, W. J. Briels, and W. P. M. van Swaaij. Discrete particle simulation of bubble and slug formation in a two-dimensional gas-fluidised bed: A hard-sphere approach. *Chemical Engineering Science*, 51(1):99 – 118, 1996.

[36] T. B. Anderson and R. Jackson. A fluid mechanical description of fluidized beds. *Industrial Engineering and Chemical Fundamental*, 6:527, 1967.

[37] H. Enwald, E. Peirano, and A. E. Almstedt. Eulerian two-phase flow theory applied to fluidization. *International Journal of Multiphase Flow*, 22(Supplement 1):21 – 66, 1996.

[38] D. Gidaspow. *Multiphase Flow and Fluidization: Continuum and Kinetic Theory Descriptions*. Academic Press, 1994.

[39] M. Syamlal. Mfix documentation: Numerical technique. *DOE/MC31346-5824, U. S. Department of Energy, Morgantown, WV.*, 1988.

[40] C. Y. Wen and Y. H. Yu. Mechanics of fluidization. *Chem. Eng. Prog. Symp. Series*, 62:100–111, 1966.

[41] M. Syamlal. The particle-particle drag term in a multiparticle model of fluidization. *DOE/MC/21353-2373, NTIS/DE87006500.*, 1987.

[42] S. Ogawa, A. Umemura, and N. Oshima. On the equation of fully fluidized granular materials. *Journal of Applied Mathematics and Physics*, 31:483 – 493, 1980.

[43] S. Chapman and T. G. Cowling. The mathematical theory of non-uniform gases. *Cambridge University Press, Cambridge, England, 3rd edition*, 1990.

[44] M. Syamlal, W. Rogers, and T. J. O'Brien. Mfix documentation: Volume 1, theory guide. Technical report, National Technical Information Service, Springfield, VA, 1993.

[45] C. K. K. Lun, S. B. Savage, D. J. Jeffrey, and N. Chepurniy. Kinetic theories for granular flow: Inelastic particles in couetter flow and slightly inelastic particles in a general flow field. *Journal of Fluid Mechanics*, 140:223–256, 1984.

[46] Y. Shih, D. Gidaspow, and D. Wasan. Hydrodynamics of electro fluidization: Separation of pyrites from coal. *AIChE Journal*, 33:1322–1333, 1987.

[47] J. D. Jackson. Classical electrodynamics. *3rd ed., New York: Wiley*, 1999.

[48] S. M. Pereira T. P. Iglesias M. A. Rivas. Relative permittivity of the mixtures (dimethyl or diethyl carbonate) + n - nonane from t = 288.15 k to t = 308.15 k. *The Journal of Chemical Thermodynamics*, 34:1897–1907, 2002.

[49] V. L. Lanza and D. B. Herrmann. The density dependence of the dielectric constant of polyethylene. *J. Polymer Science*, 28:622 – 625, 1958.

[50] K. Masamitsu and I. Masayuki. Dielectric properties of impurity doped polyethylene. *Journal of physical society of Japan*, 27(6):1604 – 1611, 1969.

[51] V. Svorcik, O. Ekrt, V. Rybka, and J. Liptak. Permittivity of polyethylene and polyethyleneterephtalate. *Journal of Materials science Letters*, 19:1843 – 1845, 2000.

[52] H. G. David, S. D. Hamann, and J.F. Pearse. The dielectric constant of ethylene at high pressures. *J. Chem. Phys*, 19:1491 – 1494, 1951.

[53] B. A. Younglove. Thermophysical properties of fluids. 1. argon, ethylene, parahydrogen, nitrogen, nitrogen trifluoride and oxygen. *Journal of Physical and Chemical Reference Data*, 11(supplement no 1), 1982.

[54] Andrew Sowinski, Fawzi Salama, and Poupak Mehrani. New technique for electrostatic charge measurement in gas-solid fluidized beds. *Journal of Electrostatics*, 67(4):568 – 573, 2009.

[55] Poupak Mehrani, Hsiaotao T. Bi, and John R. Grace. Electrostatic behavior of different fines added to a Faraday cup fluidized bed. *Journal of Electrostatics*, 65(1):1 – 10, 2007.

[56] Poupak Mehrani, Hsiaotao T. Bi, and John R. Grace. Bench-scale tests to determine mechanisms of charge generation due to particle-particle and particle-wall contact in binary systems of fine and coarse particles. *Powder Technology*, 173(2):73 – 81, 2007.

[57] Poupak Mehrani, Hsiaotao T. Bi, and John R. Grace. Electrostatic charge generation in gas-solid fluidized beds. *Journal of Electrostatics*, 63(2):165 – 173, 2005.

[58] K. Tanue and H. Masuda. *Electrostatic Separation: Powder Technology Handbook*. Third Edition CRC Press, 2006.

[59] Ram G. Rokkam, Rodney O. Fox, and Michael E. Muhle. Computational fluid dynamics and electrostatic modeling of polymerization fluidized-bed reactors. *Powder Technology*, 203:109–124, 2010.

[60] M. A. Van der Hoef, M. Van Sint Annaland, N. G. Deen, and J. A. M. Kuipers. Numerical simulation of dense gas-solid fluidized beds: A multiscale modeling strategy. *Annual Review of Fluid Mechanics*, 40:47 – 70, 2008.

[61] M. J. V. Goldschmidt, J. A. M. Kuipers, and W. P. M. van Swaaij. Hydrodynamic modelling of dense gas-fluidised beds using the kinetic theory of granular flow: effect of

coefficient of restitution on bed dynamics. *Chemical Engineering Science*, 56(2):571 – 578, 2001.

[62] R. Fan, R. O. Fox, and M. E. Muhle. Role of intrinsic kinetics and catalyst particle size distribution in cfd simulations of polymerization reactors. *Fluidization 12 conference*, Article 122:994 – 1000, 2007.

[63] A. H. Ali and R. O. Hagerty. Process and system for preventing pressure tap fouling in tandem polymerization reactors. *U. S. Patent*, 5688865, 1997.

[64] M.G. Goode, D. M. Hasenberg, T.J. McNeil, and T. E. Spriggs. Method for reducing sheeting during polymerization of alpha olefins. *U. S. Patent*, 4803251, 1989.

[65] A. H. Ali, S. M. Chranowski, J. G. Foster, and T. A. Geoghegan. Static control with teos. *U. S. Patent*, 5731392, 1998.

[66] P. Brant, M. E. Muhle, and M. Kuchta. Polymerization reactor operability using static charge modifier agents. *U. S. Patent*, 0058487 A1, 2008.

[67] T. D. Brown and M. T. OShaughnessy. Prevention of fouling in polymerization reactors. *U. S. Patent*, 3995097, 1976.

[68] J. R. Chirillo, K. C. Kimbrough II, and P. E. McHattie. Method for reducing sheeting during polymerization of alpha olefins. *U. S. Patent*, 4855370, 1989.

[69] K. K. Poliafico, M. Coyle, M. Marello, and T. M. Frantz. Method for reducing static charge and reactor fouling in a polymerization process. *U. S. Patent*, 0203259 A1, 2005.

[70] K. W. Wilcox. Prevention of fouling in polymerization reactors and antistatic agents. *U. S. Patent*, 4068054, 1978.

[71] R. S Eisinger, M. G. Goode, D. M. Hasenberg, and K. H. Lee. Process for reducing sheeting during polymerization of alpha-olefins. *U. S. Patent*, 5034479, 1991.

[72] B. D. Fulks, S. P. Sawin, C. D. Aikman, and J. M. Jenkins. Process for reducing sheeting during polymerization of alpha-olefins. *U. S. Patent*, 4792592, 1988.

[73] K. L. Neal-Hawkins, S.M. Nagy, W. J. Sartain, K. Gupte, and K. W. Johnson. Supported catalysts which reduce sheeting in olefin polymerization, process for the preparation and the use thereof. *U. S. Patent*, 6884749 B2, 2005.

[74] I. McKay, D. Jeremic, P. Mesquita, G. B. Jacobsen, and S. Mastroianni. Supported antistatic polymerization catalyst. *U. S. Patent*, 0282085 A1, 2007.

[75] M. P. Bartilucci, E. R. Davis Jr, B. J. Egan, R. O. Hagerty, and P. K. Husby. Method and apparatus for reducing static charges during polymerization of olefin polymers. *U. S. Patent*, 6548610 B2, 2003.

[76] M. E. Muhle and R. O. Hagerty. Method for operating a gas-phase reactor at or near maximum production rates while controlling polymer stickiness. *U. S. Patent*, 0060721 A1, 2007.

[77] E. J. Markel and A. K. Agapiou. Method of maintaining heat transfer capacity in a polymerization reaction system. *U. S. Patent*, 0033121 A1, 2008.

[78] J. R. Llinas and J. L. Selo. Method for reducing sheeting and agglomerates during olefin polymerization. *U. S. Patent*, 0144432 A1, 2003.

[79] H. Haardt, H. Hemmerbasch, M. Muller, H. Niederberger, D. Obermann, J. Schoofs, and K. Werle. Process for early detection of reactor fouling in gas phase polymerization. *U. S. Patent*, 6743870 B1, 2004.

[80] M. E. Muhle, P.C. Shannon, and F. D. Ehrman. Reactor wall coating and processes. *U. S. Patent*, 0063874 A1, 2004.

[81] S. Mihan, A. Lange, and W. Rohde. Solid reactor with an antistatic coating for carrying out reactions in a gaseous phase. *U. S. Patent*, 6335402 B1, 2002.

[82] L. Cohen, J. B. Haehn, and D. E. Witenhafer. Process for preventing polymer buildup in a polymerization reactor. *U. S. Patent*, 4255470, 1981.

[83] K. M. Gupte, K. Tolley, A. Mutchler, and S. Holland. Static reduction. *U. S. Patent*, 6630548 B1, 2003.

[84] R. B. Painter, B. J. Garner, and G. H. Song. Gas phase fluidized bed polyolefin polymerization process using gas or gas-solids tangential flow. *U. S. Patent*, 5428118, 1995.

[85] W. Fang, W. Jingdai, and Yongrong. Distribution of electrostatic potential in gas-solid fluidized bed and measurement of bed level. *Industrial and Engineering Chemistry Research*, 47:9517 – 9526, 2008.

[86] Andrew Sowinski, Leigh Miller, and Poupak Mehrani. Investigation of electrostatic charge distribution in gassolid fluidized beds. *Chemical Engineering Science*, 65:2771–2781, 2010.

[87] J. F. Parmentier, O. Simonin, and O. Delsart. A numerical study of fluidization behavior of geldart b, a/b and a particles and using an eulerian multifluid modeling approach. *Werther, J., Wirth, K.E., Nowak, W. (Eds.), Ninth International Conference on Circulating Fluidized Beds, Hamburg, Germany*, 2008.

[88] J. F. Parmentier, O. Simonin, and O. Delsart. A functional subgrid drift velocity model for filtered drag prediction in dense fluidized-bed. *AIChE Journal*, 58:1084 – 1098, 2011.

[89] A. Ozel. Development of large eddy simulation approach for simulation of circulating fluidized beds. *PhD thesis, Universite de Toulouse, Toulouse, France*, 2011.

[90] OpenCFD. The open source cfd toolbox user's guide, 1st edition. *OpenCFD Ltd., United Kingdom*, 2010.

[91] OpenCFD. The open source cfd toolbox programmer's guide, 1st edition. *OpenCFD Ltd., United Kingdom*, 2010.

[92] A. Passalacqua and R. O. Fox. Implementation of an iterative solution procedure for multifluid gas-particle flow models on unstructured grids. *Powder Technology*, 213:174 – 187, 2011.

[93] C. M. Rhie and W. L. Chow. A numerical study of the turbulent flow past an isolated airfoil with trailing edge separation. *AIAA Journal*, 21:1525 – 1532, 1983.

[94] P. C. Johnson and R. Jackson. Frictional collisional constitutive relations for granular materials with applications to plane shearing. *Journal of Fluid Mechanics*, 176:67 – 93, 1987.

[95] Y. T. Makkawi, P. C. Ocone, and R. Ocone. The effect of friction and inter-particle cohesive forces on the hydrodynamics of gassolid flow: A comparative analysis of theoretical predictions and experiments. *Powder Technology*, 163:69 – 79, 2006.

[96] J. Ruud van Ommen, M. Coppens, C. M. van den Bleek, and J. C. Schouten. Early warning of agglomeration in fluidized beds by attractor comparison. *AIChE Journal*, 46(11):2183 – 2197, 2000.

[97] L. A. Noble. Method of preventing or reducing polymer agglomeration on grid in fluidized-bed reactors. US Patent 0215956 A1, Assigned to Westlake Longview Corporation, 2009.

[98] J. Lunas and J. Selo. Method of reducing and agglomerates during olefin polymerization. US Patent 0165179 A1, 2005.

[99] M. Tamura, K. Takimiya, and T. Konaka. Method and apparatus for detecting agglomerates. US Patent 6,417,295 B1, Assigned to Sumitomo Chemical Company, 2002.

[100] S. Rigopoulos. Population balance modelling of polydispersed particles in reactive flows. *Progress in Energy and Combustion Science*, In Press, Corrected Proof:–, 2010.

[101] R. B. Diemer and J. H. Olson. A moment methodology for coagulation and breakage problems: Part 2–moment models and distribution reconstruction. *Chemical Engineering Science*, 57(12):2211 – 2228, 2002.

[102] D. L. Marchisio, R. D. Vigil, and R. O. Fox. Quadrature method of moments for aggregation-breakage processes. *Journal of Colloid and Interface Science*, 258(2):322 – 334, 2003.

[103] D. L. Marchisio, R. D. Vigil, and R. O. Fox. Implementation of the quadrature method of moments in cfd codes for aggregation-breakage problems. *Chemical Engineering Science*, 58(15):3337 – 3351, 2003.

[104] R. McGraw. Description of aerosol dynamics by the quadrature method of moments. *Aerosal Science and Technology*, 27:255–265, 1997.

[105] D. L. Marchisio and R. O. Fox. Solution of population balance equations using the direct quadrature method of moments. *Journal of Aerosol Science*, 36(1):43 – 73, 2005.

[106] R. O. Fox. Bivariate direct quadrature method of moments for coagulation and sintering of particle populations. *Journal of Aerosol Science*, 37(11):1562 – 1580, 2006.

[107] L. F. L. R. Silva, R. C. Rodrigues, J. F. Mitre, and P. L. C. Lage. Comparison of the accuracy and performance of quadrature-based methods for population balance problems with simultaneous breakage and aggregation. *Computers and Chemical Engineering*, 34(3):286 – 297, 2010.

[108] L. F. L. R. Silva, R. B. Damian, and P. L. C. Lage. Implementation and analysis of numerical solution of the population balance equation in cfd packages. *Computers and Chemical Engineering*, 32(12):2933 – 2945, 2008.

[109] B. Selma, R. Bannari, and P. Proulx. Simulation of bubbly flows: Comparison between direct quadrature method of moments (dqmom) and method of classes (cm). *Chemical Engineering Science*, 65(6):1925 – 1941, 2010.

[110] R. Fan, D. L. Marchisio, and R. O. Fox. Application of the direct quadrature method of moments to polydisperse gas-solid fluidized beds. *Powder Technology*, 139(1):7 – 20, 2004.